MASTER'S THESIS

STORM SURGE MODELING
IN A CLOSED AND SEMI-ENCLOSED BASIN

The influence of basin topography and wind direction on the set-up along the coast using 1-DH and 3-D flow models.

F. Upmeijer BSc

University of Twente

STORM SURGE MODELING IN A CLOSED AND SEMI-ENCLOSED BASIN

THE INFLUENCE OF BASIN TOPOGRAPHY AND WIND DIRECTION ON THE SET-UP ALONG THE COAST USING 1-DH AND 3-D FLOW MODELS

In partial fulfillment of the requirements for the degree of

Master of Science in Water Engineering and Management
Faculty of Engineering Technology University of Twente

Author: Frank Upmeijer BSc
Contact: f.upmeijer@gmail.com

Date: August 16, 2016
Thesis defend date: August 22, 2016
Location: Enschede, The Netherlands

Graduation committee

Graduation supervisor:	Dr. Ir. J.S. Ribberink	University of Twente
Daily supervisors:	Dr. Ir. P.C. Roos	University of Twente
	Dr. W. Chen	University of Twente

UNIVERSITY OF TWENTE.

Abstract

Destruction due to flooding, caused by severe storms, is a serious concern along coastal areas. The rise or set-up of the water level induced by a storm is called a storm surge. Improved understanding and accurate predictions of storm surges along the coast will help reducing the negative impacts of coastal disasters. An important aspect of improving storm surge predictions requires physical insight in the influence of basin topography on the set-up along the coast of large-scale basins.

This study investigates the influence of the basin topography on the wind-driven response of large-scale coastal basins, measured in terms of the set-up at the coast, and paying particular attention to the role of the location of a topographic element, such as a shoal or a sand pit, relative to the wind direction. For this purpose, two different idealised process-based models have been used to simulate linearised hydrodynamics in closed and semi-enclosed rectangular basins driven by time-periodic wind forcing: (i) an analytical 1-DH flow model and (ii) the semi-analytical 3-D flow model of W.L. Chen et al. (2016). The frequency response, as obtained from these models, displays in particular resonance peaks, which we explain by linking them to the basin dimensions, the wind direction as well as the influence of the function, size and location of topographic elements.

In general, it is found that adding topographic elements in front of the coast causes the resonance peaks to shift in the frequency domain, through their effect on local wave speed. Increasing bottom friction lowers the peaks. Furthermore, sensitivity analyses demonstrated that resonant frequencies strongly depend on the combination of basin topography and wind direction, particularly in shallow areas where bottom friction dominates the basin dynamics.

Subsequently, we illustrate how the frequency response is reflected in the time-dependent set-up generated by a single wind event. It turns out that the lower frequencies of the wind forcing input clearly dominate the behavior of the time-dependent set-up, relative to higher frequencies. This can be explained by the fact that due to the applied characteristics of a wind event, a large portion of the wind spectrum's energy is distributed over the lower frequencies of the spectrum. Moreover, this study demonstrates how to trigger optimal set-up behavior by modifying the basin topography for a given wind event with a certain wind speed, wind duration, ramp stage and most important, wind angle.

Preface

First of all, I would like to thank my family and friends for their great support during this research project. Many thanks to my mother Ank, with whom I have shared many joys and sorrows throughout this period of this intense project. During this period I lived at my mother's place, where I spent most of my time conducting this study. Thank you for your patience and unconditional support. I will soon help you finishing your lovely new garden!

Furthermore I would like to thank my brother Peter for his support, reading parts of this thesis and for making my cover page a lot more attractive. Also, I would like to thank my sister Judith for her advices and her great trust in me. And of course for offering me a very small job as your personal administrator during this project. I would also like to thank my friends for their patience, understanding and support during this period of dealing with new complex methodologies, and therefore had to skip many fun things, which we will certainly catch up for any time soon! In addition, I want to thank my teammates and staff of my soccer squad S.V. Gramsbergen 3, where I found fun distraction, relaxation and exercise during this period.

And of course many thanks to my supervisors, for their patience and thorough explanations for complex matter. Thank you Pieter for our pleasant meetings, where you explained complex matter in a simple way, and therefore leaving this meetings with a good and confident feeling. And also for motivating me when I was stuck at some point. Always positive and enthusiastic, which is appreciated. And Wenlong, thank you for your help, time and patience while you were busy graduating yourself during this period. And of course great respect for developing such complicated codes in Matlab, making it possible for me to simulate these complex but very interesting flow dynamics in coastal basins. Thanks for that and congratulations on your excellent performance in achieving your well deserved PhD title. And finally Jan, thank you for your trust in me, your patience and giving helpful advice about my work from a different perspective, which has led to some new and valuable insights during the research period.

A moment like this calls for reflection as well. First of all, I have learned a lot during this project. Not only interesting mathematical skills and methods, but also the process you undergo. Staring blindly at certain possible explanations and tendencies of found results, where letting go and move is mostly the best option and works very enlightening at the same time. Furthermore, I wanted to figure out difficulties along the road by myself, where I should have asked for help more often. And of course I have come to understand the great value of a sound planning, which is key in these kind of complex studies. This is also the end of my time as a student at the University of Twente. When I look back at this great time I'm also glad it's finally finished now, looking forward towards a new adventure!

I hope you enjoy reading this thesis! Please feel free to contact me by mail (third page) for questions and/or unclarities regarding this study.

Table of Contents

Chapter 1

Introduction

1.1 Storm surges in coastal basins

Severe storms form a big threat to life and property in coastal regions, especially in low-lying densely populated areas which are most vulnerable to flooding. Therefore the destruction due to flooding is a serious concern along coastal regions. Due to sea level rise and the potential increase in heavy storms resulting from climate change, extreme coastal flooding events are likely to increase in the future (Brown et al., 2010), while the population in coastal zones is expected to increase (IPCC, 2007). Improved understanding and accurate predictions of storm surges along the coast will help reducing the negative impacts of coastal disasters.

Over the last decades, a lot of model studies have been conducted regarding all kind of factors influencing a storm surge. In these studies factors have been analyzed ranging from characteristics of a storm, such as storm size and intensity (e.g. Irish et al., 2008; Weisberg & Zheng 2006c), to the unique properties of a coastal basin, such as topography and geometry (e.g. Q. Chen et al., 2008; Guo et al., 2009). Moreover, due to a better understanding of oceanic physical processes together with an exponential growth of computational capacities, the complexity of hydrodynamic models has increased as well as the potential to predict storm surges more accurately. Although the basic physics of a storm surge on an open coast or in a large estuary is relatively well understood, our understanding of the interactions between storm surges, wind waves, tides and complex topographic and geographic landscapes, such as coastal basins, is still inadequate (Q. Chen et al., 2008). In the following paragraphs we will narrow the wide number of factors down to a final selection on which we will aim our research project.

A storm surge, defined as a rise or set-up of surface water elevation induced by a storm, is mainly driven by meteorological forcing consisting of reduced atmospheric pressure and wind forcing. Other factors such as waves and storm-driven rainfall, which originate from these two main forces, have a minor contribution to the surge height and duration (Lowe et al., 2001). Furthermore, many studies have shown that the reduced atmospheric pressure response is inferior to the wind forcing response (e.g. Jones & Davies, 2007; Rego and Li, 2010). Not only the storm size and intensity, but also other storm characteristics, such as wind direction, appear to influence the storm surge. For example, studies of Guo et al. (2009) and Weisberg & Zheng (2006b) have shown that the behavior of the surge set-up changed drastically when wind direction changes.

In extreme cases of flooding events, a phenomenon known as resonance may occur. A few examples of recent storms, causing extreme coastal flooding, that have been linked to such resonant conditions are typhoon Winnie at the Korean coast of the Yellow Sea and storm Xynthia in the Bay of Biscay. For example, Moon et al. (2003) demonstrated that the residual part, on top of the main part generated by enhanced tidal forcing from the spring tide, of the surge driven by Winnie can be explained by the resonance coupling of the natural periods of the Yellow Sea and the predominant period in the surge. Moreover, Bertin et al. (2012) demonstrated, through an analytical resonance

model and numerical experiments, that the period of the observed oscillations corresponds to the resonant mode of the continental shelf, by analyzing the storm surge associated with Xynthia.

Among the abundant literature available on the subject, a common approach consists of performing a hindcast of a relevant storm to analyze the physical processes responsible for the associated surge (e.g. Moon et al., 2003; Bertin et al., 2012). However, it is difficult to identify the physics from these often complex site-specific events. It requires a more systematic approach to attain insights in the physical processes underlying this wind-driven set-up. A good start is the semi-analytical approach of Ponte (2010), linking the resonance properties of a basin to several types of resonant frequencies. More specifically, he identified resonance peaks associated with along-basin standing waves from his idealized 3-D flow model for elongated basins subject to periodic and spatially uniform wind forcing. The oscillations associated with these peaks were already investigated more generally by Rao (1966). His numerical study particularly demonstrated that the resonant frequencies strongly depend on the width and length of the basin.

This research project elaborates on all of the literature above and particularly on the meantime finished PhD project of W.L. Chen (2015). Furthermore, this study will contribute to the understanding of the important resonance properties of closed and semi-enclosed basins and will give further insights in the physical processes, such as bottom friction, underlying the wind-driven coastal set-up. In particular, we will systematically analyze the influence of topographic basin elements (function, size and location) on the set-up along the coast, subject to time-periodic and space-uniform wind forcing in arbitrary direction.

A more practical motivation for this study is to explain and predict the effects of large-scale sand measures near the coast. For example, large-scale sand mining in the North Sea, whereby most studies (e.g. Walstra et al., 1999) focus on the long-term morphological effects, regarding erosion and sedimentation processes, of this kind of coastal operations. An important and interesting consequential issue could be, regarding this research project, how to manage these types of large-scale operations in such a way to avoid large and long (after sloshing) set-up along the coast?

1.2 Research outline

1.2.1 Research objective

To make more accurate predictions of storm surges in coastal basins, it is important to study the underlying physical processes more specifically, based on a selected number of factors. By making use of idealised hydrodynamic models it is possible to study specific physical processes separately. Since we have experienced a lack of insight in the existing literature about the sensitivity of storm surges in coastal basins to basin topography and wind direction, the research objective of this study is formulated as:

> *To carry out a systematic sensitivity analysis of the wind-driven set-up at the coastal boundary of a closed and semi-enclosed basin to changes in basin topography and wind direction induced by a spatially uniform wind forcing, through idealised process-based modelling.*

This study will be conducted using two process-based models: (i) an analytical 1-DH flow model and (ii) the semi-analytical 3-D flow model of W.L. Chen et al. (2016). An important feature of these flow

models is that they calculate the basin's surface elevation in the frequency domain, instead of in the more conventional time domain. Induced by periodic wind forcing, the basin's surface elevation response in the frequency domain is called the spectral response.

1.2.2 Research questions

The following research questions are formulated to achieve the research objective:

1. How is a time-dependent single wind event converted in the frequency domain and how are its characteristics influencing the spectral representation?
2. How do we formulate the idealised process-based hydrodynamical models suitable for simulation of the set-up along the basin's coastal boundary for the closed and semi-enclosed basin?
3. What are the effects of varying the bottom friction coefficient and topographic basin dimensions on the basin's spectral response at the rear end of the closed and semi-enclosed basin, using the 1-DH flow model?
4. What is the influence of implementing topographic elements, such as shoals and pits, and wind direction on the basin's spectral response at the rear end of the closed and semi-enclosed basin, using the 3-D flow model?
5. How to obtain the actual response of the time-dependent set-up in the basin, induced by a single wind event? And how is the spectral response reflected in the time-dependent set-up?

1.2.3 Methodology

The methodology used in this study to achieve the research objective and to answer the research questions will be treated here in the order of the structure of this report.

In this study we will consider a single wind event (in the order of days) as a superposition of periodic wind forcings at various frequencies ω, after Craig (1989) and Chen (2016). Therefore, periodic wind forcing will be used as the sole input force that drives both flow models. This further implies that we neglect atmospheric pressure forcing in this study. Such an event in the time domain can be converted in the frequency domain by using the well known fast Fourier transform algorithm. This methodology will be used to convert several wind events with various wind characteristics in the frequency domain to study its influence on the spectral representation of a wind event. In turn, the inverse Fourier transform function enables us to convert the wind signal in the frequency domain back in the time domain, and can also be applied to determine the accuracy of representing our wind event of interest in the time domain by the chosen number of Fourier modes.

In our study, we have adopted an idealised process-based modeling approach. This enables us to simplify the basin geometry and certain hydrodynamic processes, while applying solution techniques which are precise in mathematics. Furthermore, we have adopted a linear approach for both of our flow models and therefore ignore non-linear processes such as e.g. advection and tide-surge interaction. In turn, the linearised shallow water equations are used in both flow models to express the hydrodynamic processes in the basin.

The coastal basins will be simulated in two different ways: a closed and a semi-enclosed basin. The closed basin representation is the more simple case, because it excludes dealing with complex open boundaries. The semi-enclosed basin representation does include an open boundary,

which better connects to simulating coastal basins in practice. However, the closed basin results will serve as a good practice to understand and interpret the basin's spectral response to periodic wind forcing, regarding the resonance properties of the basin. Moreover, the closed basin representation connects to recent studies in the literature (e.g. Ponte, 2010 & Chen et al., 2015). Furthermore, our study frame consist of a rectangular basin with a fixed and strongly simplified geometry for the closed and semi-enclosed basin, applied in our models. The chosen basin dimensions in this study are considered to be roughly consistent with the rectangular-shaped geometry of the Southern Bight of the North Sea (shown in Figure 1.1) and also connect to the dimensions of the closed basin study of W.L. Chen (2015). The dimensions of the Southern Bight are approximately: 340 km length, 165 km width and an average basin depth of 25 m (van der Molen et al., 2004).

Figure 1.1: Southern Bight of the North Sea (dark blue) in front of the Dutch coast (Beets et al., 1999).

The 1-DH flow model will be used to study various 1-DH cases for a better understanding of the underlying physical processes of the hydrodynamics in a simplified coastal basin. This analytical model simulates the basin hydrodynamics in a one-dimensional depth-averaged (1-DH) manner, driven by a spatially uniform periodic wind forcing in along-basin direction. Because the model cannot simulate cross-basin dynamics, Coriolis effects are ignored as well in this study. A single step topography will be applied to simulate depth differences in the basin.

Next, the semi-analytical 3-D flow model of W.L. Chen et al. (2016) will be used to study 3-D cases for analyzing the spectral response behavior in a less simplified coastal basin, driven by a spatially uniform periodic wind forcing in arbitrary direction. Furthermore, the 3-D flow model will be used to simulate more complex and realistic basin topographies compared to the 1-DH model, whereas the basin geometry still remains strongly simplified in this study. The model is based on the widely adopted Finite Element Method (FEM). Relative to several other two- and three-dimensional finite difference/volume and finite element models that have been widely adopted and used to simulate hurricane-induced storm surges (W.L. Chen et al., 2013), which are mostly very time consuming, this 3-D flow model of Chen needs much less computation time because of its semi-analytical approach in combination with the Fourier transform method (W.L. Chen, PhD thesis, 2015). And is thus suitable for idealised process-based modeling as well.

To determine the accuracy of the FEM model simulations, the results of the 1-DH and the FEM model simulations will be compared with each other for similar simplified cases in both types of basins. A statistical measure ('standard error of the estimate' (Lane, 2015)) is used to determine the goodness of fit of the 1-DH simulations with the FEM simulations. To obtain a better fit, the 1-DH model will be calibrated with respect to the FEM model regarding the linearised bottom friction coefficients of both models.

Finally, the basin's response (time-dependent set-up along the coast) to a single wind event can be derived by multiplying the Fourier spectrum of a single wind event with the basin's spectral response, obtained by the flow models. In turn, this complex product in the frequency domain can be converted back in the time domain by applying the inverse Fourier transform function again. An overview of how these methodology aspects all connect in this research project, is presented in Figure 1.2.

1.3 Report outline

The report is structured by the following chapters.

Chapter 2: Fourier transform approach. Because the Fourier transform techniques plays such an important part in this study, the fundamentals of this approach are explained more in detail in this chapter. Furthermore, a sensitivity analysis has been conducted to study the influence of wind event characteristics on the spectral representation of the wind event. This will give an answer to the first research question.

Chapter 3: Model formulation. The two flow models that are used in this study are formulated and explained further with the shallow water equations and their underlying assumptions. The semi-analytical 3-D flow model of W.L. Chen et al. (2016) will be treated first, followed by the analytical 1-DH flow model. Mainly, the formulation and its derivations (Appendix A) of the 1-DH model contributed to obtaining the solution for the spectral response of the basin's surface elevation, which answers the second research question.

Chapter 4: Results of the analytical 1-DH flow model. Several case studies have been performed with the 1-DH model and the results are presented in this chapter. The conducted sensitivity analyses give an answer to the third research question, which serves as a basis for the case studies to be performed using the FEM model.

Chapter 5: Results of the semi-analytical 3-D flow model. Several case studies have been performed in the FEM model to study the effects of topographic elements in combination with wind direction. The results are presented in this chapter. The conducted sensitivity analyses give an answer to the fourth research question. Furthermore, the results of both models have been compared with each other, based on similar study cases.

Chapter 6: Time-dependent response of the basin's surface elevation to a single wind event. The insights gained from the previous chapters will be applied to illustrate some of the main effects on the actual time-dependent set-up in the basin, via a few study cases. These cases will be driven by a few different single wind events and the resulting spectral responses will be converted into the time domain. This way, the actual response of the basin's elevation can be obtained to see its oscillating effects over time for the cases of interest. This will answer the last research question.

Chapter 7: Discussion. Here, we discuss the main findings of this study and threat model choices and assumptions formulate the conclusions.

Chapter 8: Conclusions & Recommendations. This final chapter answers the research questions of this research project, followed by recommendations for further study.

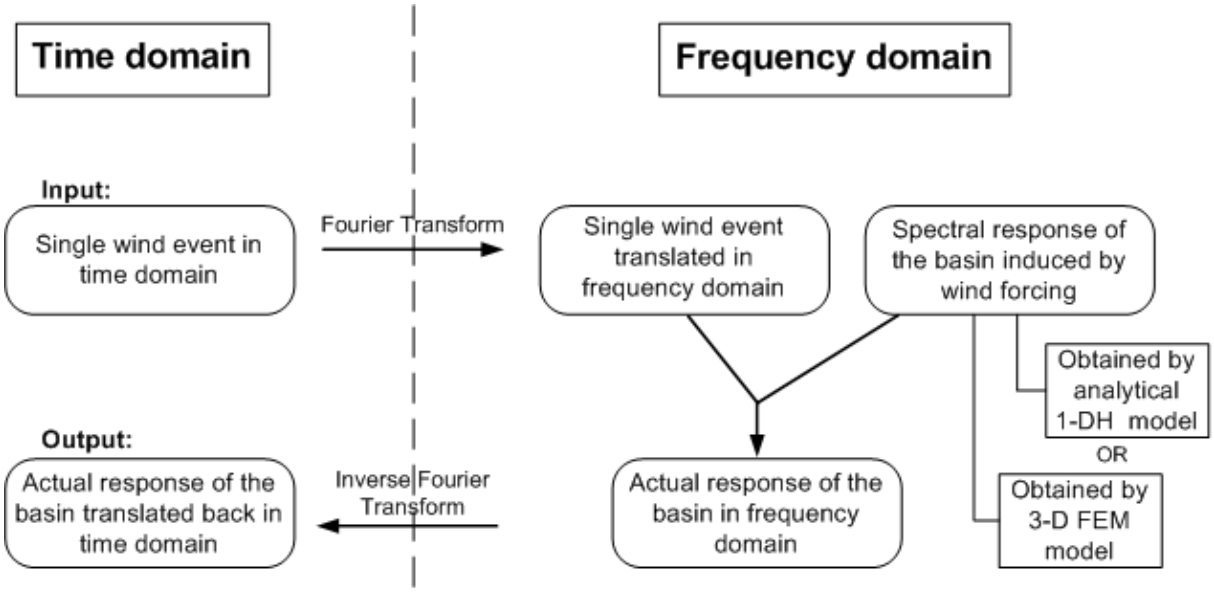

Figure 1.2: Overview of the connected methodology aspects in the research project, distinguished by the temporal (*left*) and spectral (*right*) representation. By following these steps (in clockwise direction, starting in the upper left corner), the actual response of the basin in the time domain will be required. The spectral response of the basin can be obtained by choosing one of the two models.

Chapter 2

Fourier transform approach

In this chapter we will explain how a single wind event in the time domain can be converted to the frequency domain and converted back to the time domain by using Fourier transform techniques. Section 2.1 treats the theory behind these techniques. In Section 2.2 we apply these techniques by converting some examples of time-dependent wind events in to the frequency domain. In addition, we illustrate how a wind event in the time domain is reproduced by a superposition of Fourier modes using the inverse Fourier transform. At the end, an exploratory sensitivity analysis will be conducted to study the influence of some typical wind event characteristics, such as effective duration and ramp stages, on the representation in the frequency domain.

2.1 Temporal and spectral representation of a single wind event

At first, the terms temporal and spectral representation will be explained. If a signal is represented by its value as a function of time in the time domain, we call this the *temporal representation* of the signal. If a signal is represented by its amplitude and phase as a function of frequency in the frequency domain, we will call this the *spectral representation* of the signal. It should be clear that these representations are just two different ways of representing the same signal. Each representation can be derived from the other by using Fourier transform techniques, i.e. one of the two representations is required to obtain both representations for any signal. The Fourier transform approach allows us to switch easily between the two representations.

One important aspect of the Fourier theory is that any smooth periodic signal can be represented as a sum of sinusoids. These sinusoids consist of a mixture of cosines and sines to represent the amplitude and phase information of the periodic signal properly. This is the so-called discrete Fourier series representation (e.g., see Duhamel et al., 1988). In this study we consider a single wind event as a periodic signal. Therefore a single wind event is defined as a signal that will be repeated every T_{recur} days, to be discussed further below in Section 2.2.1. The Fourier series is denoted by:

$$y(t) = \sum_{m=0}^{\infty} A_m \cos\left(\frac{2\pi m t}{T_{\text{recur}}}\right) + B_m \sin\left(\frac{2\pi m t}{T_{\text{recur}}}\right), \tag{2.1}$$

with coefficients A_m and B_m and mode number m. Thereto, B_0 is irrelevant. The signal $y(t)$ can be either input or output. It can represent for example wind stress regarding the forcing or surface elevation regarding the solution. In this chapter $y(t)$ represents the wind stress of a single wind event. If we consider the periodic signal to be smooth, the infinite sum gives a perfectly accurate representation of the signal $y(t)$. An approximation will be given by truncating this sum to a finite sum M-1. In fact $y(t)$ is decomposed into M sinusoids with appropriate amplitude, phase and frequency components. These frequency components consist of integers, the so-called higher

harmonics ($m\omega_o$ for m = 2, 3, 4, …), of the fundamental frequency ($\omega_o = 2\pi/T_{recur}$). Eq. (2.1) now becomes:

$$y(t) = A_0 + \sum_{m=1}^{M-1} A_m \cos(m\omega_0 t) + B_m \sin(m\omega_0 t) \tag{2.2}$$

Since cosines and sines have no average term, periodic signals that have a non-zero average will have a constant component A_0. We can derive the spectral representation of the periodic signal $y(t)$, once we know the coefficients A_0, A_m and B_m. Instead of using integration techniques (e.g., see Weisstein 2015) to calculate the coefficients, a more efficient algorithm will be used to compute the Fourier series. This algorithm is known as the fast Fourier transform (FFT) and will be used in this study to obtain the spectral representation of a single wind event.

Now consider the same periodic signal $y(t)$ again, composed of a sequence of P numbers y_o, y_1, .., y_{P-1}. The Fourier series can be derived by transforming the signal y_p into a series of complex numbers Y_m, using the following algorithm:

$$Y_m = \sum_{p=0}^{P-1} y_p \exp\left(-\frac{2\pi i p m}{P}\right) \tag{2.3}$$

Depending on the number of modes M, each complex number Y_m encodes both amplitude and phase of the corresponding sinusoidal component of the signal y_p. The FFT-function is provided as a built-in function in MATLAB, which enables us to do these computations fast and easy.

Once we have obtained the spectral representation of a single wind event in the frequency domain, we can present it in a graph by plotting the complex amplitude of each mode m per corresponding frequency $m\omega_o$. This shows to which extent the frequencies are being forced by the wind event. In upcoming chapters we will calculate the frequency response of the basin by exerting periodic wind forcing on the hydrodynamic systems. A periodic wind forcing is represented by a sinusoid of a particular frequency. A range of periodic wind forcings of various frequencies will be used as input vector in our hydrodynamic models. In turn, the models calculate the resulting complex amplification of the surface water elevation, which is the frequency response of the implemented wind forcing. In this report, the frequency response is also called the *spectral response*. To obtain the actual response of the basin's elevation (AR_m) to a specific wind event, the spectral representation of the wind event (Y_m) has to be multiplied by the basin's spectral response to unit wind forcing (SR_m):

$$AR_m = Y_m \cdot SR_m \tag{2.4}$$

Finally, to obtain the actual response (ar_p) of the basin in the time domain, the complex multiplication function AR_m has to be converted back to the time domain using the inverse Fourier transform function:

$$ar_p = \frac{1}{P} \sum_{m=0}^{M-1} AR_m \exp\left(\frac{2\pi i p m}{P}\right) \tag{2.5}$$

In the upcoming section, examples of single wind events in the temporal representation have been converted in the spectral representation. In addition, a sensitivity analysis has been conducted to study the influence of typical characteristics of a single wind event on its spectral representation.

2.2 Single wind event cases in the time and frequency domain

2.2.1 Single wind event representation in the time domain

In the previous section we showed that a single wind event can be represented as a signal composed of a superposition of many sinusoids. The fact that a single wind event is repeated over time is a direct consequence of using the discrete Fourier transform method to translate the signal in the frequency domain later on. Figure 2.1 shows an example of a wind event repeated over recurrence time T_{recur}. The forcing of the wind is denoted by the value of the wind stress.

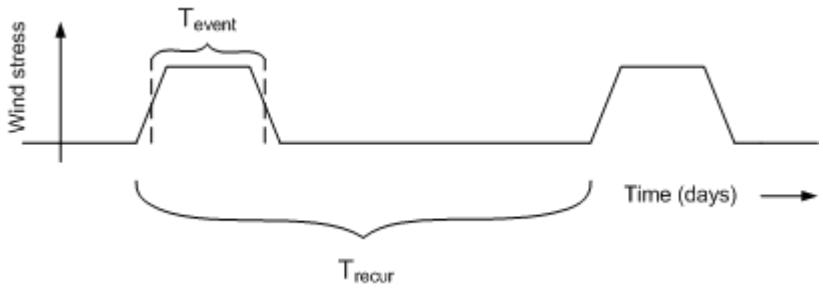

Figure 2.1: Single wind event representation in time domain over period T_{recur}.

A wind event is considered to gradually increase (decrease) in amplitude when gaining force (damping out). These smoothed ramp stages are defined here as a cosine function. The duration of a ramp stage is denoted by T_{ramp}. The smoothness of a wind event plays an important role in the spectral representation of the wind event, which we will show later in the chapter. To illustrate the smoothness of a wind event in the time domain, a wind event of six hours (T_{event}) without ramping (Fig. 2.2a) is compared to a wind event of the same effective duration with smoothed ramp stages (Fig. 2.2b). In the latter case, the effective duration T_{event} is defined as the time span between halfway ramp-up and halfway ramp-down of the wind event, such that the forcing area corresponds to the former case. In these wind events, a wind stress of 1 N m^{-2} is applied as maximum forcing.

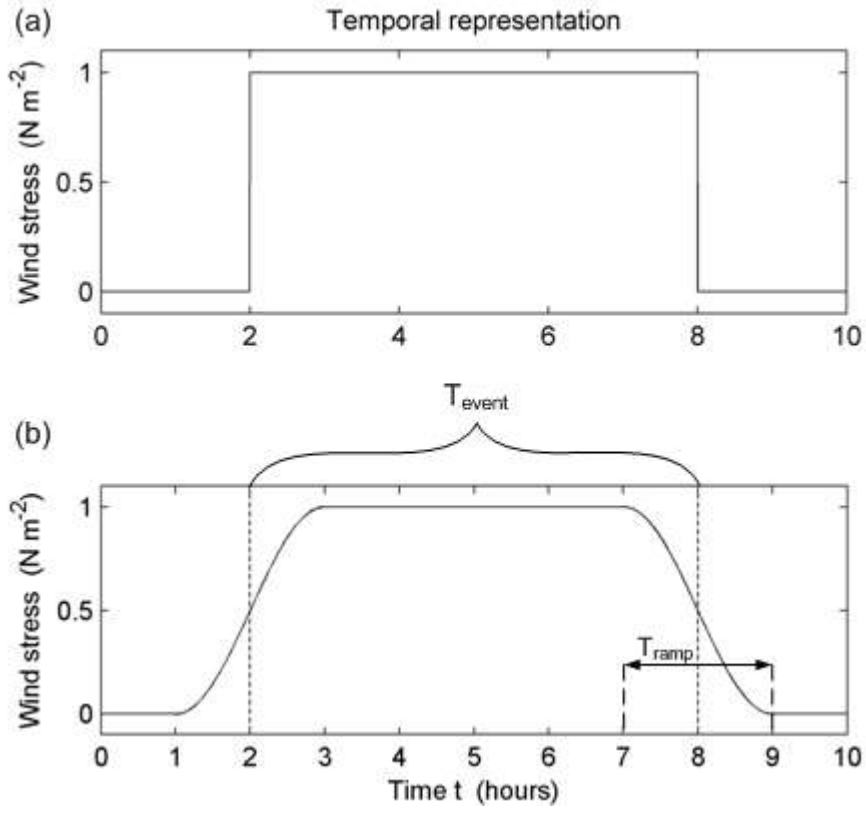

Figure 2.2: Temporal representation of two single wind events with the same T_{event} (6 hrs): (a) without ramp stages (T_{ramp} = 0), (b) with smoothed ramp stages (T_{ramp} = 2 hours).

In the following section we will convert these and other examples of wind events in the frequency domain using the fast Fourier transform technique in MATLAB. An exploratory sensitivity analysis will be conducted regarding the effects of varying the durations T_{ramp} and T_{event} of single wind events.

2.2.2 Single wind event representation in the frequency domain

In Section 2.1 we explained that we can use the FFT-function in MATLAB for converting signals in time domain to signals in frequency domain. By using this technique, we can choose the number of Fourier modes to represent our wind event in the time domain. The more modes *m* we choose, the more accurate the wind event is being represented by its underlying sum of *m* sinusoids (also explained in Section 2.1). A drawback, however, is an increase in computation time when applying more modes. To illustrate the degree of accuracy, the wind event from the previous section (Fig. 2.2) is reproduced by means of a superposition of 75 and 150 modes. A recurrence time T_{recur} of 10 days is used for this wind event to connect with work of Chen (Chen et al., 2015). The original wind event (dotted black) is reproduced by 75 (blue) and 150 (pink) Fourier modes over a time span of 16 hours, shown in Figure 2.3. This clearly shows that the reproduced wind event with T_{ramp} (Fig. 2.3b) is much more accurately representing the original wind event than the reproduced wind event without T_{ramp} (Fig. 2.3a). Furthermore it shows that a higher accuracy can be obtained, for both ramp representations, by choosing more modes.

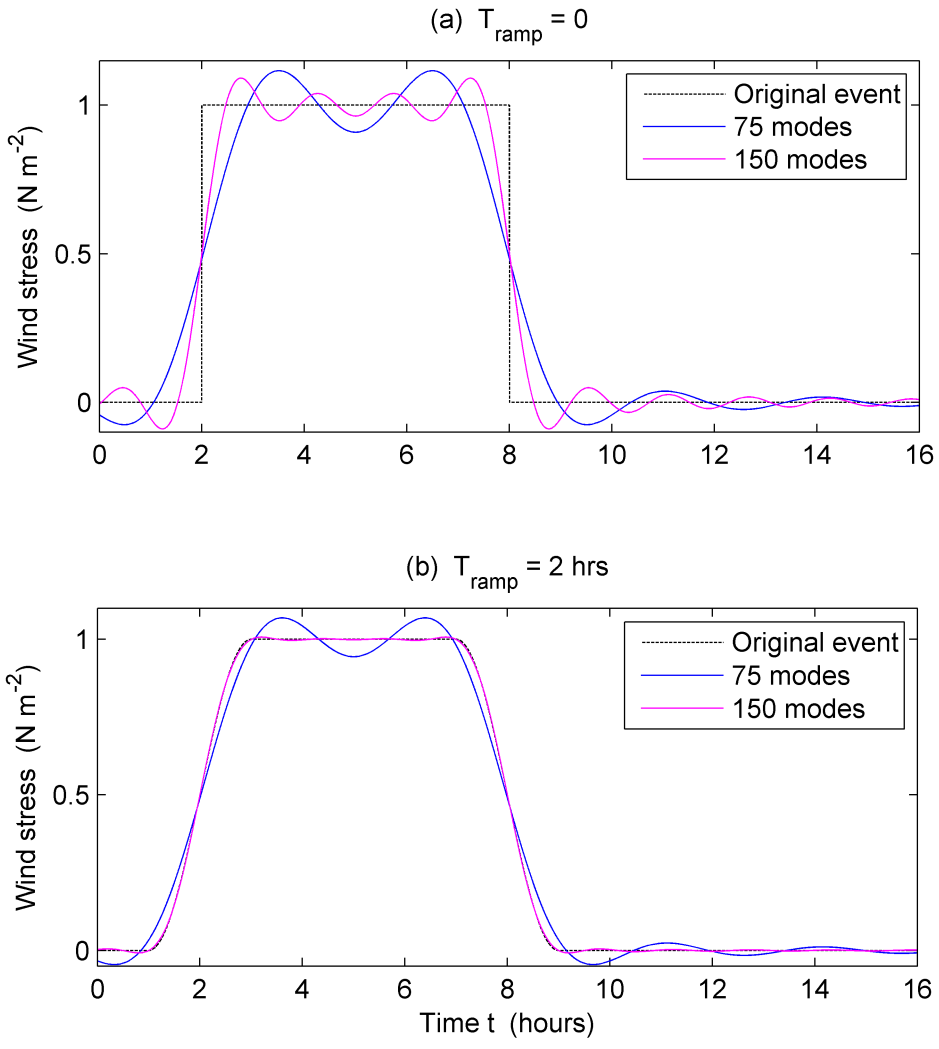

Figure 2.3: Accuracy test: Original wind event (T_{event} = 6 hrs) with (b) and without (a) T_{ramp} (2 hrs), reproduced by a superposition of 75 (blue) and 150 (pink) Fourier modes with T_{recur} = 14 days.

Next, to illustrate the influence of duration and ramp stages on the spectral representation of a wind event, two effective wind event durations with various ramp stages are converted to the frequency domain. The durations and ramp stages will be expressed as a dimensionless fraction of T_{recur}. This means that, regardless of the value T_{recur}, for a fixed number of modes identical fractions for duration and ramp stage of a wind event will give identical Fourier spectra. A few examples of wind events with two different durations and four different ramp stages are converted in the frequency domain and shown in Figure 2.4. Of course the number of Fourier modes still influences the Fourier spectra. Here we have chosen the number of 300 modes, which is very accurately representing the time-dependent wind events. The maximum magnitudes, not shown in the plots, for Figure 2.4a and 2.4b are 0.05 and 0.15 N m^{-2} respectively. First, Figure 2.4 clearly shows that ramp stages of a wind event in time domain influences the representation in the frequency domain. It illustrates that T_{ramp} has a significant influence on the spectral representation of the wind event, especially in the tail of the graph. Further increasing T_{ramp} will lower the wind amplification in the Fourier spectrum even more. Second, by comparing Figure 2.4a with 2.4b, it can be concluded that increasing T_{event} increases the wind amplification in the frequency domain. Furthermore, increasing T_{event} will result in more condensed amplification peaks in the frequency domain.

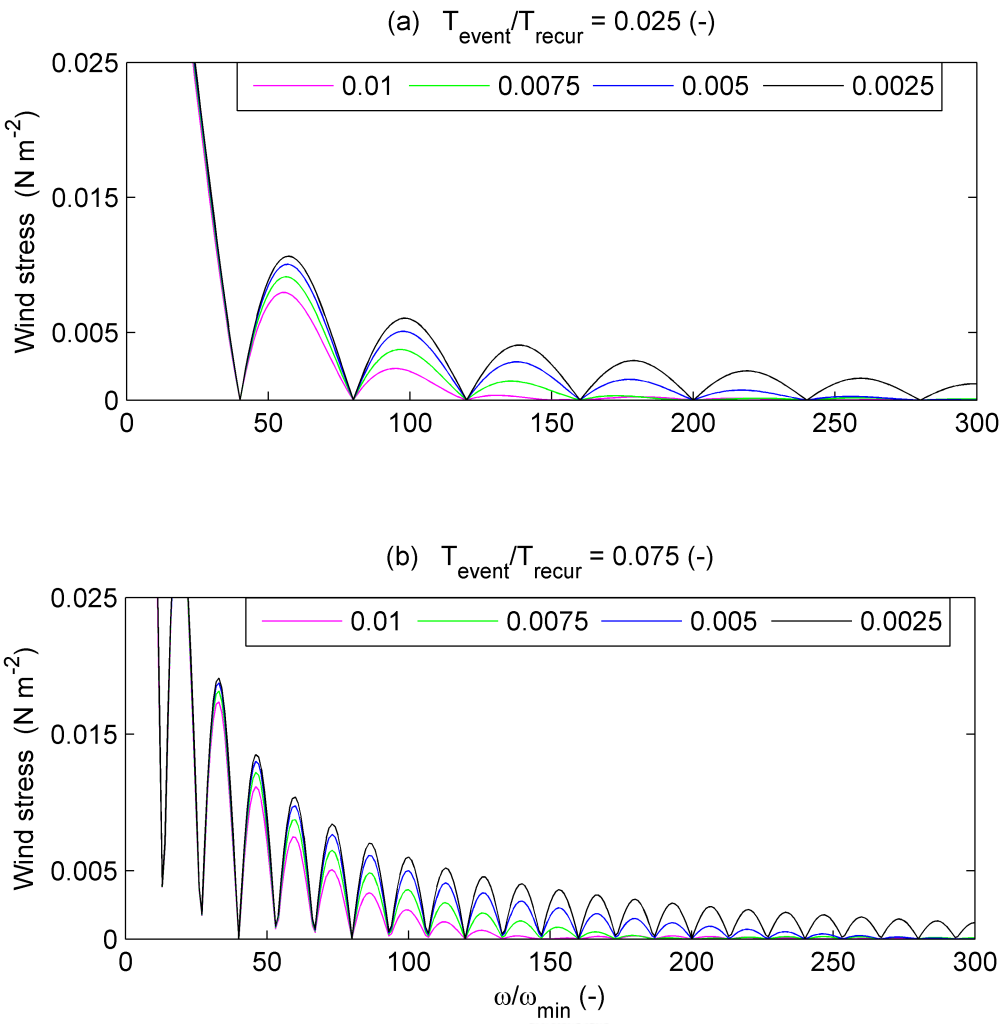

Figure 2.4: Spectral representation of two wind events (a & b) with multiple ramp stages T_{ramp}/T_{recur} (-); wind stress (N m^{-2}) as a function of the dimensionless forcing frequency ω/ω_{min} (modes): (a) Effective wind event duration T_{event}/T_{recur} of 0.025 (-) with various dimensionless values of T_{ramp}/T_{recur} = 0.0025 (black), 0.005 (blue), 0.0075 (green) and 0.01 (pink), (b) T_{event}/T_{recur} = 0.075 (-) with the same ramp stages.

To illustrate the sensitivity of the spectral representation of a wind event to changes in T_{event}, a series of single wind events with various durations have been converted to the frequency domain using 300 modes. The several wind event cases are conducted with two ramp stages that are used in Figure 2.4 as well: T_{ramp}/T_{recur} = 0.0025 (a) & 0.01 (b) (-), presented in color plots in Figure 2.5 (next page). Furthermore, the effective wind event durations presented in Figure 2.4 are represented by the white dashed lines in Figure 2.5. Only the first 150 modes are shown to zoom in on the differences between the two color plots. Figure 2.5 once more illustrates how the characteristics, duration and smoothness of ramp stages, of a wind event influence the spectral representation of a wind event. These insights are valuable for interpreting spectral responses of the basin's elevation in upcoming chapters.

Later in Chapter 6, we give more examples of single wind events, with realistic values for variables T_{ramp}, T_{event}, T_{recur} and number of frequency modes, to see their influences on the time-dependent set-up of the basin.

2.3 Summary

By considering a single wind event and its response as a periodic signal, it allows us to easily switch between the between the temporal and spectral representation of both forcing and response by means of the Fourier transform approach. Its application will be further addressed particularly in Chapter 6.

Furthermore, an exploratory sensitivity analysis has shown that the duration (T_{event}) and smoothness (T_{ramp}) of a wind event play an important role in the spectral representation of the wind event. It turns out that the spectral energy of the wind signal is distributed in more condensed peaks with higher amplitudes when we increase T_{event}, and that increasing T_{ramp} will lower the amplitudes, especially at higher frequencies. These insights are valuable for interpreting spectral responses of the basin's elevation in Chapters 4, 5 and 6.

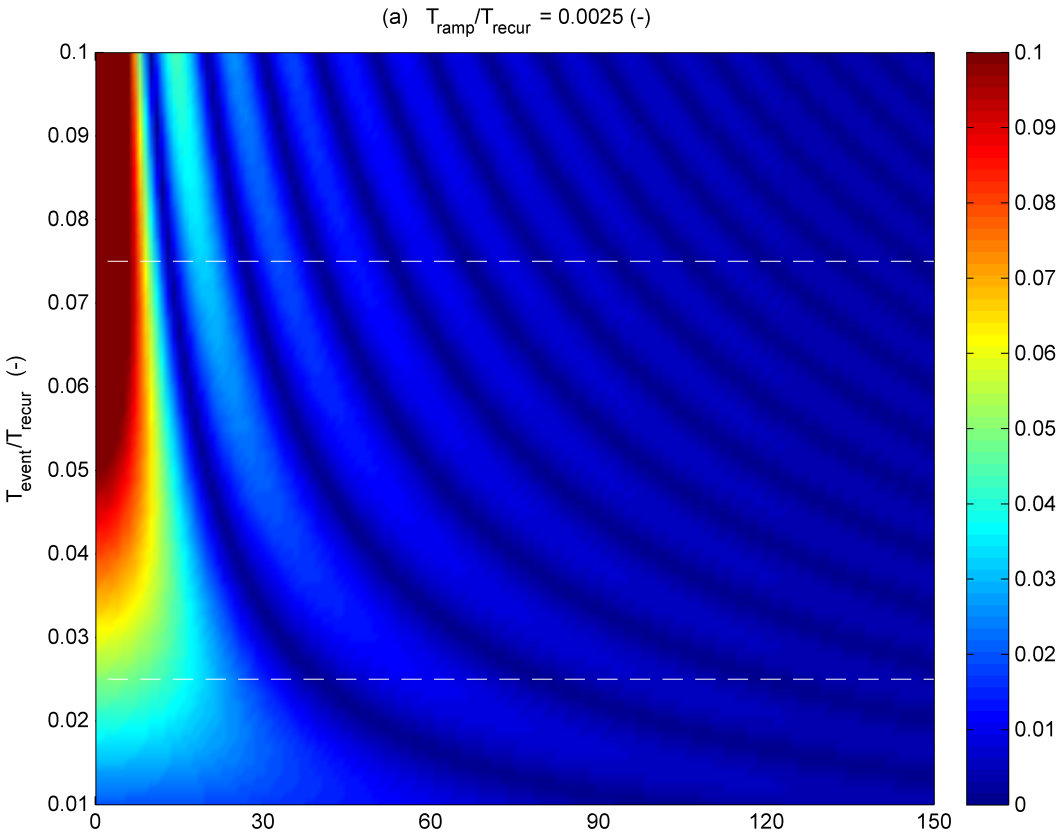

Figure 2.5: Wind stress (N m^{-2}) as a function of frequency ω/ω_{min} (modes) (horizontal axis) and wind duration T_{event}/T_{recur} (-) (vertical axis) of a single wind event: (a) T_{ramp}/T_{recur} = 0.0025 (-), (b) T_{ramp}/T_{recur} = 0.01 (-). The dashed white lines in both plots represent the wind event cases with T_{event}/T_{recur} = 0.025 & 0.075 (-). Both plots are simulated with 300 modes (the first 150 modes are shown here).

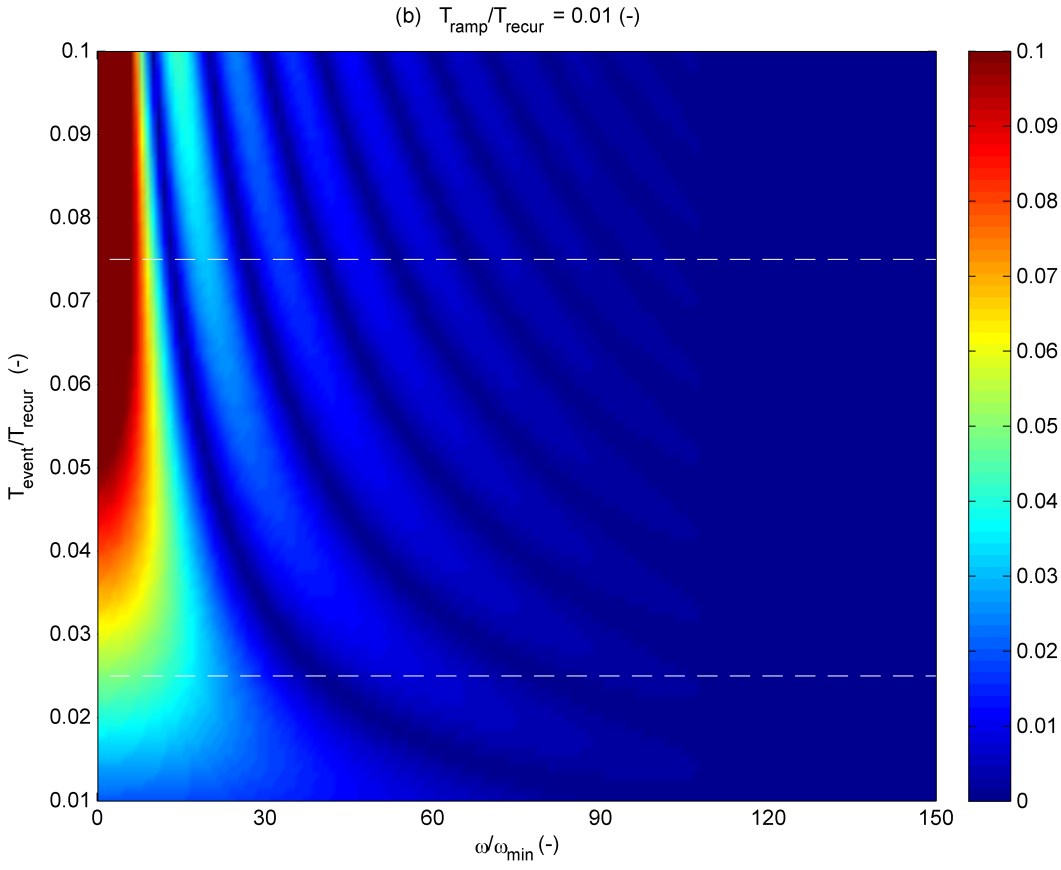

Chapter 3

Model formulation

This chapter treats the formulation of the analytical 1-DH model and the semi-analytical 3-D FEM model of W.L. Chen et al. (2016). First, the model outline of the 3-D flow model will be treated in Section 3.1. Here, the hydrodynamics, boundary conditions and a short outline of the solution method will be given. Next, the model outline of the 1-DH flow model will be treated in Section 3.2, where a transition from the 3-D hydrodynamics towards the 1-DH hydrodynamics takes place. All underlying assumptions will be treated thoroughly.

3.1 Outline of the FEM model

3.1.1 Representation of the closed and semi-enclosed basin

This study is focused on two different types of rectangular basins: a closed and a semi-enclosed basin. The closed basin consists of four closed basin boundaries where water cannot flow through. The semi-enclosed basin has three closed boundaries and one open boundary, where water can flow through, but where elevation will be fixed. The geometry of both types of basins is presented in Figure 3.1.

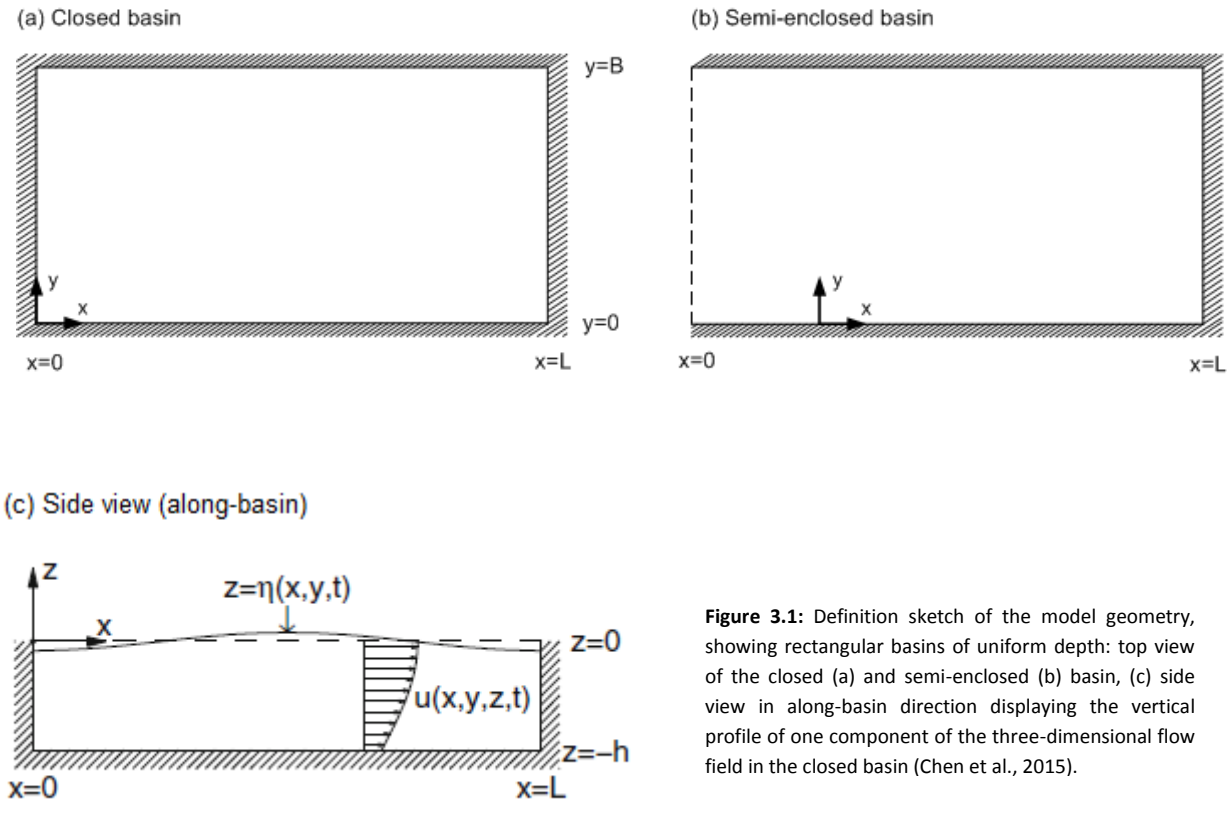

Figure 3.1: Definition sketch of the model geometry, showing rectangular basins of uniform depth: top view of the closed (a) and semi-enclosed (b) basin, (c) side view in along-basin direction displaying the vertical profile of one component of the three-dimensional flow field in the closed basin (Chen et al., 2015).

Here, *x* and *y* are the along-basin and cross-basin coordinates of the rectangular basin with length *L* and width *B*. The open boundary in the semi-enclosed basin is located at *x* = 0. The topography of the basin can be varied in many ways. In Figure 3.1c we have presented a flat bed topography in the closed basin, resulting in a uniform depth *h*. The depth contours of the basin are modeled by the vertical coordinate *z*. The bed level is denoted by *z* = -*h* with respect to the undisturbed water level *z* = 0 and the free surface elevation $z = \eta$. An important aspect of the FEM model is that we can model smoothly varying topographies. These kind of topographic elements will be treated more thoroughly in Chapter 5.

3.1.2 Shallow water equations

Here, we will introduce the hydrodynamics to describe the processes applied in the water system of the FEM model. The shallow water equations, which are derived from the well known Navier-Stokes equations, are used to express the hydrodynamic processes. By assuming linear dynamics, based on the assumption η/h << 1, non-linear processes will be neglected. Conservation of momentum and mass is expressed by the linearised shallow water equations:

$$\frac{\partial u}{\partial t} = -g\frac{\partial \eta}{\partial x} + \frac{\partial}{\partial z}\left[K_{\mathrm{v}}\frac{\partial u}{\partial z}\right], \tag{3.1}$$

$$\frac{\partial v}{\partial t} = -g\frac{\partial \eta}{\partial y} + \frac{\partial}{\partial z}\left[K_{\mathrm{v}}\frac{\partial v}{\partial z}\right], \tag{3.2}$$

$$\frac{\partial u}{\partial x} + \frac{\partial v}{\partial y} + \frac{\partial w}{\partial z} = 0. \tag{3.3}$$

Here, *u*, *v* and *w* (m s^{-1}) are the flow velocity components in *x*, *y* and *z*-direction, *g* is the gravitational acceleration (9.81 m s^{-2}), η is the free surface elevation (m) and K_v is the uniform vertical eddy viscosity (m^2 s^{-1}). Horizontal mixing of momentum is neglected. Although the model can deal with Coriolis effects, they are neglected here to focus on other mechanisms influencing the surface elevation's behavior, such as wind direction, bottom friction and topographic basin elements.

3.1.3 Boundary conditions

The model is driven by wind forcing only, while atmospheric pressure is neglected. Thereto, the system is forced by imposing a time-dependent wind stress at the free surface. At the bottom, a partial-slip condition is imposed to include bottom friction. Assuming that the vertical displacement of the free surface is small (rigid lid approximation), the vertical boundary conditions along with the kinematic boundary conditions are given by

$$w = \frac{\partial \eta}{\partial t}, \qquad K_{\mathrm{v}}\left(\frac{\partial u}{\partial z}, \frac{\partial v}{\partial z}\right) = \frac{\left(\tau_{\mathrm{w}}^{(x)}, \tau_{\mathrm{w}}^{(y)}\right)}{\rho_{\mathrm{w}}} \qquad \text{at } z = 0, \tag{3.4}$$

$$w = 0, \qquad K_{\mathrm{v}}\left(\frac{\partial u}{\partial z}, \frac{\partial v}{\partial z}\right) = s(u, v) \qquad \text{at } z = -h. \tag{3.5}$$

The rigid lid approximation allows the free surface condition to be imposed at *z* = 0 instead of at $z = \eta$. Bottom friction is represented by the partial-slip condition with resistance parameter *s* (m s^{-1}).

Large *s* corresponds to a no-slip condition, where *s* = 0 corresponds to a free-slip condition. The wind forcing at the surface of the basin consists of the wind stress τ_w (kg m^{-1} s^{-2}) divided by the water density ρ_w (1000 kg m^{-3}). Suggested by Wu (1982), the wind stress can be obtained by applying a commonly used empirical relation between wind stress and wind velocity:

$$\tau_w = \rho_a C_d |W| W, \qquad \text{with } C_d = (0.8 + 0.065 \cdot W) \cdot 10^{-3}, \tag{3.7}$$

with air density ρ_a (1.2 kg m^{-3}), dimensionless drag coefficient C_d and the vector W (m s^{-1}) denoting the two-dimensional horizontal wind velocity vector 10 m above the water surface.

Furthermore, the horizontal boundary conditions concern the closed and semi-enclosed boundaries, depending on the geometry of the basin, shown in Figure 3.1. At the closed boundaries in the model domain, we impose a zero transport condition normal to the closed boundaries. This implies that there is no-normal flow at these boundaries. Therefore we require the vertical integration from bottom to surface of *u* and *v* to be zero at these locations:

$$\left.\begin{aligned} \int_{-h}^{0} u(x,z,t)dz = 0 \quad & \text{at } x = 0, L \\ \int_{-h}^{0} v(y,z,t)dz = 0 \quad & \text{at } y = 0, B \end{aligned}\right\} \text{Closed basin} \tag{3.8}$$

In the semi-enclosed basin, we assume that the open boundary is connected with the outer sea, represented by a huge deep water mass. This outer region effectively imposes a boundary condition to our domain of interest. This implies that the surface water elevation is considered to be zero at this open boundary, which results in the imposed Dirichlet condition: η = 0. At the closed boundaries, we impose no-normal flow, as in Eq. (3.8), i.e.

$$\left.\begin{aligned} \eta(x,y,t) = 0 \quad & \text{at } x = 0 \\ \int_{-h}^{0} u(x,z,t)dz = 0 \quad & \text{at } x = L \\ \int_{-h}^{0} v(y,z,t)dz = 0 \quad & \text{at } y = 0, B \end{aligned}\right\} \text{Semi} - \text{enclosed basin} \tag{3.9}$$

3.1.4 Outline of the solution method

The water system is forced by a time-periodic and space-uniform wind stress with angular frequency ω (rad s^{-1}), aligned with the *x*-direction. By using complex notation, the wind stress vector ($\tau_w^{(x)}$, $\tau_w^{(y)}$) in Eq. (3.4) is denoted as follows:

$$\frac{\left(\tau_w^{(x)},\ \tau_w^{(y)}\right)}{\rho_w} = \Re\left\{\left(T^{(x)},\ T^{(y)}\right)\exp(-i\omega t)\right\}, \tag{3.10}$$

where amplitude $T^{(x)}$, $T^{(y)}$ (m^2 s^{-2}) denotes the magnitude of the wind forcing (wind stress divided by water density). The solution to a periodic wind in an arbitrary direction is the superposition of the separate solutions for wind in *x*- and *y*-direction only. By assuming a dynamic equilibrium, the solution of the surface elevation and currents will be expressed in a time-periodic fashion as well, according to

$$\eta(x, y, t) = \Re\{N(x, y)\exp(-i\omega t)\}, \tag{3.11}$$

$$u(x, y, z, t) = \Re\{U(x, y, z)\exp(-i\omega t)\}, \tag{3.12}$$

with complex amplitudes *N* and *U*. Similar expressions hold for *v* and *w*, with complex amplitudes *V* and *W*. The equations will be solved numerically to find the surface elevation at particular locations in the basin. A complete explanation of the solution method can be found in Chen et al., 2016.

3.2 Outline of the analytical 1-DH model

The second model that we use in this study is an analytical 1-DH flow model. In this model we have applied a slightly modified coordinate system for mathematical convenience. Furthermore we have chosen a simplified basin topography. The applied single step topography is a simple but effective method to simulate depth differences in the basin. In this way the resonance properties of the basin can be studied sufficiently for the purpose of this study. Because we can simulate far more complex and realistic basin topographies in the 3-D model, it is not necessary to simulate more complex basin topographies in the 1-DH model.

3.2.1 Representation of the closed and semi-enclosed basin

Unlike the 3-D flow model, treated in the previous section, we assume one-dimensional depth-averaged flow in the 1-DH flow model. Here, the width *B* of the basin is considered to be very small compared to the length *L* of the basin, i.e. $B \ll L$. This means that cross-basin flow is negligible and one-dimensional flow is considered in the *x*-direction. The geometry of both types of basins is presented in Figure 3.2.

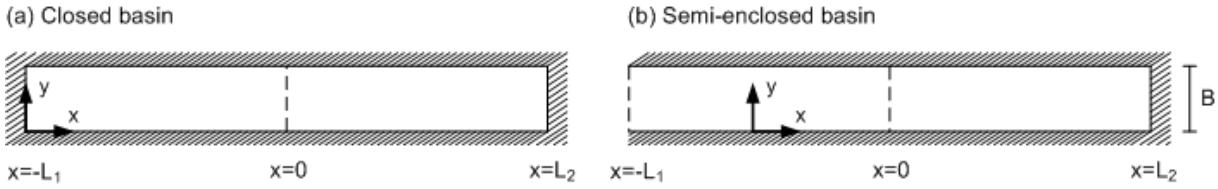

Figure 3.2: Sketches of the model geometries of the two basins: (a) top view of the closed basin, (b) top view of the semi-enclosed basin with open boundary at $x = -L_1$, represented by the dashed line at the left boundary. A step location is situated at $x = 0$, represented by the dashed line at the center of the basin. The width of the basin *B* is assumed to be very small compared to the length *L* of the basin ($B \ll L$).

Here, *x* and *y* are the along-basin and cross-basin coordinates with the along-basin boundaries located at $x = -L_1$ and $x = L_2$. The open boundary in the semi-enclosed basin is located at $x = -L_1$. To create depth differences in the basin, a topographic step is introduced, located at $x = 0$. An important notification here is that the basin consists of two compartments. These two compartments (1 & 2) generally have a different uniform water depth h_1 and h_2, connected by a topographic step. A flat bed topography is represented by setting $h_1 = h_2$. Moreover, $\bar{h}$ denotes the average depth of the basin. The length of compartment 1 and 2 is denoted by L_1 and L_2 respectively. The lengths and depths of the compartments can be varied in the model. A sketch of the basin topography is presented in Figure 3.3.

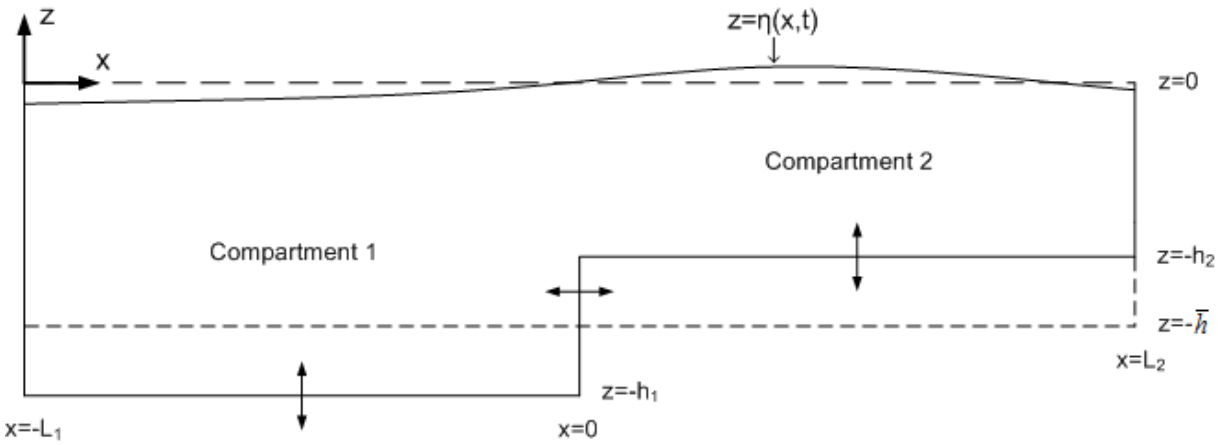

Figure 3.3: Side view sketch of a single step topography in the closed basin, consisting of two compartments which can vary in depth and length (represented by the arrows). Coordinates $x = -L_1$ and $x = L_2$ represent the horizontal boundary locations. The water depths of compartment 1 and 2 are h_1 and h_2 respectively, connected by a step at $x = 0$. The surface elevation relative to the still water level (upper dashed line) is denoted by $\eta(x,t)$. A flat bed case is represented by the lower dashed line, with average water depth $\bar{h}$. A similar sketch applies for the semi-enclosed basin, only with an open boundary at $x = -L_1$.

3.2.2 Shallow water equations

In our analytical model, we assume depth-averaged flow and neglect flow in the *y*-direction ($B \ll L$), which results in our one-dimensional depth-averaged (1-DH) flow model. To obtain the 1-DH shallow water equations, we depth-integrate Eqs. (3.1) and (3.3) from bottom to surface of the basin with conditions (3.4) and (3.5) in the *x*-direction only. In addition, the bottom stress formulation (Eq. 3.5) is parameterized by replacing su at the bottom by $r\bar{u}$. Here, we have introduced a linear bottom friction coefficient r (m s^{-1}). Subsequently, the resulting 1-DH shallow water equations are denoted by:

$$\frac{\partial \bar{u}}{\partial t} + \frac{r\bar{u}}{h} = -g\frac{\partial \eta}{\partial x} + \frac{\tau_w^{(x)}}{\rho_w h}, \tag{3.13}$$

$$\frac{\partial \eta}{\partial t} + h\frac{\partial \bar{u}}{\partial x} = 0, \tag{3.14}$$

$$\text{with} \quad \bar{u}(x,t) = \frac{1}{h}\int_{-h}^{0} u(x,z,t)dz. \tag{3.15}$$

With depth-averaged flow $\bar{u}$ in *x*-direction.

3.2.3 Matching and boundary conditions

Here, it has been taken into account that the depth of the basin is uniform everywhere, except at the step. Therefore matching conditions, consisting of continuity of volume transport and surface water elevation, apply at the step location ($x = 0$):

$$\bar{u}_1 h_1 = \bar{u}_2 h_2, \qquad \eta_1 = \eta_2 \qquad \text{at } x = 0. \tag{3.16}$$

Since the water is bounded, no horizontal flow is imposed at the closed boundaries. The horizontal boundary conditions for the closed basin are given by

$$\bar{u}_1 = 0 \text{ at } x = -L_1, \qquad \bar{u}_2 = 0 \text{ at } x = L_2. \qquad \text{(closed basin)} \tag{3.17}$$

In the semi-enclosed basin, we impose a zero surface elevation condition at the open boundary, as in the FEM model. At the closed boundary, the condition of no horizontal flow, as in Eq. (3.17), is imposed. The horizontal boundary conditions for the semi-enclosed basin are given by

$$\eta_1 = 0 \text{ at } x = -L_1, \qquad \bar{u}_2 = 0 \text{ at } x = L_2. \qquad (\text{semi} - \text{enclosed basin}) \tag{3.18}$$

3.2.4 Outline of the solution method

The wind forcing is again assumed to be time-periodic and space-uniform and considered as an along-basin wind. In complex notation, this will be denoted as

$$\frac{\tau_{\mathrm{w}}^{(x)}}{\rho_{\mathrm{w}}} = \Re\left\{T^{(x)} \exp(-i\omega t)\right\}, \tag{3.19}$$

By assuming a dynamic equilibrium, the solution of the differential problem will be written in a time-periodic fashion, with complex amplitudes *N* and *U*, according to:

$$\eta(x,t) = \Re\{N(x)\exp(-i\omega t)\}, \tag{3.20}$$

$$\bar{u}(x,t) = \Re\{U(x)\exp(-i\omega t)\}. \tag{3.21}$$

Because the system of equations is linear, the problem can be reduced to solving the complex amplitudes *N* and *U*. By substitution, the amplitudes satisfy

$$-i\omega U + \frac{rU}{h} = -g\frac{\partial N}{\partial x} + \frac{T^{(x)}}{h}, \tag{3.22}$$

$$-i\omega N + h\frac{\partial U}{\partial x} = 0. \tag{3.23}$$

By rearranging Eq. (3.22) it follows that

$$-i\omega\gamma^2 U = -g\frac{\partial N}{\partial x} + \frac{T^{(x)}}{h}, \qquad \text{with } \gamma^2 = \left(1 + \frac{ir}{\omega h}\right). \tag{3.24}$$

A complex frictional correction factor γ^2 has been introduced as a function of the linear friction coefficient *r*. In absence of bottom friction, this factor is equal to one. The derived equations of motion (3.23 & 3.24) for this 1-DH setting can now be solved analytically for any location (*x*), by applying the matching and boundary conditions (3.16 – 3.18).

In Chapter 4, the surface elevation at a specific location in the basin will be calculated. Because we are mainly interested in the behavior of the surface elevation at the coast, we have chosen to focus on the closed boundary at the rear end of the basin. This means that we will study the behavior of the surface elevation at the rear end of the basin ($x = L_2$), and that this location will be our *evaluation point* in upcoming analyses. Before that, we first have to derive the solution at this point: $N_2(L_2)$. The solution method is further explained in Appendix A.

3.3 Summary

Two flow models will be used in this study to simulate the hydrodynamics in the basin. The hydrodynamic processes are expressed by the linearised shallow water equations in both models. While the semi-analytical 3-D model simulates both the along- and cross-basin dynamics, the analytical 1-DH model only simulates the along-basin dynamics based on depth-averaged flow velocities. However, the 1-DH model will be mainly used to better understand certain processes (treated in the next chapter) which play an important role in the set-up behavior of shallow coastal basins, subject to along-basin wind forcing. In turn, these insights will contribute to interpret the results of the cases in the 3-D model, and in particular the results concerning the behavior of the basin's spectral response, subject to wind forcing in arbitrary direction.

Two types of coastal basins are considered in this study: a closed and a semi-enclosed basin. These rectangular basins differ from each other by a closed and an open boundary at the front of the basin, expressed in the boundary conditions for both models.

The 1-DH model can only simulate step topographies (including a flat bed), whereas the 3-D model can simulate several types of complex topographies. Which specific basin topographies we actually study will be treated in Chapters 4 and 5.

Chapter 4

Results of the analytical 1-DH model

To answer the third research question, several cases have been studied using an analytical 1-DH model. The underlying surface elevation solutions of this model have been derived in Appendix A.2 and A.3.

First we will illustrate how resonance is reflected in the spectral response of both types of basins by simulating simple cases in the model. At the same time, the influence of bottom friction is shown in the spectral response of these reference cases (Section 4.1).

In turn, we will study the influence of varying the topography on the basin's spectral response of both types of basins by conducting two sensitivity analyses in Section 4.2. The first analysis focuses on the depth differences of two basin compartments in general, to study the influence of the basin's depth ratio on the basin's spectral response (Section 4.2.1). The resulting insights will be explained more thoroughly by highlighting specific cases in Section 4.2.2. The second analysis focuses on the influence of topographic elements, such as shoals and pits, on the basin's spectral response (Section 4.2.3). For each case the volume of the basin remains constant by redistributing sand in the basin, in contrast to the cases in Section 4.2.1. All the cases, required for both analyses, have been simulated with different bottom friction coefficients to illustrate the influence of bottom friction as well.

4.1 Reference flat bed case

Resonance plays an important role in the spectral response behavior in our modeled cases. To illustrate the phenomenon of resonance, we will first look into the solutions of the most simple cases in the model: flat bed topography without bottom friction in the closed and semi-enclosed basin. The solutions for these cases at the rear end of the basin ($x = L$) are derived in Appendix A (Eqs. A.14 & A.24):

$$N(L)_{\text{closed}} = \frac{T^{(x)}}{ghk}\left(\frac{1-\cos kL}{\sin kL}\right); \qquad N(L)_{\text{semi}} = \frac{T^{(x)}}{ghk}\tan kL, \tag{4.1}$$

$$\text{with } k = \frac{\omega}{\sqrt{gh}}.$$

Resonance will occur if these amplitudes ($N(L)_{\text{closed}}$ & $N(L)_{\text{semi}}$) take on large values. In the closed basin, large values will be obtained if the term $\sin kL$ in the denominator of the solution becomes very small, say $\sin kL \approx 0$, whereas the enumerator attains a finite value. Since $\sin kL = 0$ if kL equals to integers of π, resonance occurs if kL becomes close to integers of π. This is true only if the term $\cos kL \neq 1$ in the enumerator. Because $\cos kL = 1$ if kL equals even integers of π, resonance only occurs if kL becomes close to odd integers of π, i.e. $kL = \pi$, 3π, 5π… etc. The same reasoning can be applied to the solution of the semi-enclosed basin, resulting in occurrence of resonance if kL becomes close to odd integers of ½ π, i.e. $kL =$ ½ π, 3/2 π, 5/2 π… etc.

Before we plot the solutions of the flat bed cases, two scaling terms will be introduced first. The amplification of the surface water elevation will be expressed in terms of the dimensionless elevation amplitude *A*, defined as $A = |N_L|/N_{\mathrm{ref}}$. The scaling term N_{ref} is a reference elevation which follows from the balance between surface elevation and wind stress. From chapter 3, the terms at the right hand side of the momentum equation (3.24) have to contain identical scales in order to conserve the balance. The required surface elevation *N* of the shallow water wave to balance the wind stress, follows from the horizontal derivative term of *N*. The magnitude of the horizontal derivative of *N* will be *kN*, due to the fact that the shallow water wave has a cosine *kx* behavior. Scaling term N_{ref} is then derived according to:

$$gkN = \frac{T^{(x)}}{h} \quad \rightarrow \quad N = \frac{T^{(x)}}{ghk}, \ \text{with } k = \frac{\omega}{\sqrt{gh}} \quad \rightarrow \quad N_{\mathrm{ref}} = \frac{T^{(x)}}{\omega\sqrt{gh_{\mathrm{ref}}}}. \tag{4.2}$$

This so-called scaling argument gives roughly the reference elevation N_{ref} required for a shallow water wave with reference depth h_{ref} to balance the wind stress $T^{(x)}$ for a certain frequency ω.

The forcing frequency range will be expressed in the dimensionless frequency term $\omega/\omega_{\mathrm{ref}}$. The scaling term ω_{ref} is a reference frequency which is defined as the frequency for which the frictionless shallow water wavelength λ equals the basin length *L*:

$$\lambda = \frac{2\pi\sqrt{gh}}{\omega}; \qquad \rightarrow \quad \omega_{\mathrm{ref}} = \frac{2\pi\sqrt{gh}}{L}. \tag{4.3}$$

To this end, in the flat bed topography cases, the classical resonance peaks are obtained at $\omega/\omega_{\mathrm{ref}}$ - values of odd integers of ½ in the closed basin and odd integers of ¼ in the semi-enclosed basin, clearly illustrated in Figure 4.1 for both types of basins.

The solutions of the spectral response at the rear end of the basin are presented in Figure 4.1 for the closed and semi-enclosed basin. The spectral response is represented by the amplification (*A*) as a function of a range of forcing frequencies ($\omega/\omega_{\mathrm{ref}}$). To illustrate the influence of bottom friction, the results of a few flat bed cases with different values of the bottom friction coefficient *r* are presented in the figure. The figure shows that the blue and red peaks coincide with the classical resonance peaks for the closed and semi-enclosed basin respectively. Furthermore, it shows that the amplitudes at the resonant frequencies decrease as the friction coefficient increases. In line with that, extremely large resonance peaks show up in the flat bed cases without bottom friction (*r* = 0), not shown in the figure. These results apply to closed and semi-enclosed basins of arbitrary basin length and depth with a flat bed topography, forced by a periodic wind forcing with arbitrary wind stress. In upcoming sections, we will use these results as a reference case to analyze the sensitivity of spectral response behavior to changes in topography and bottom friction.

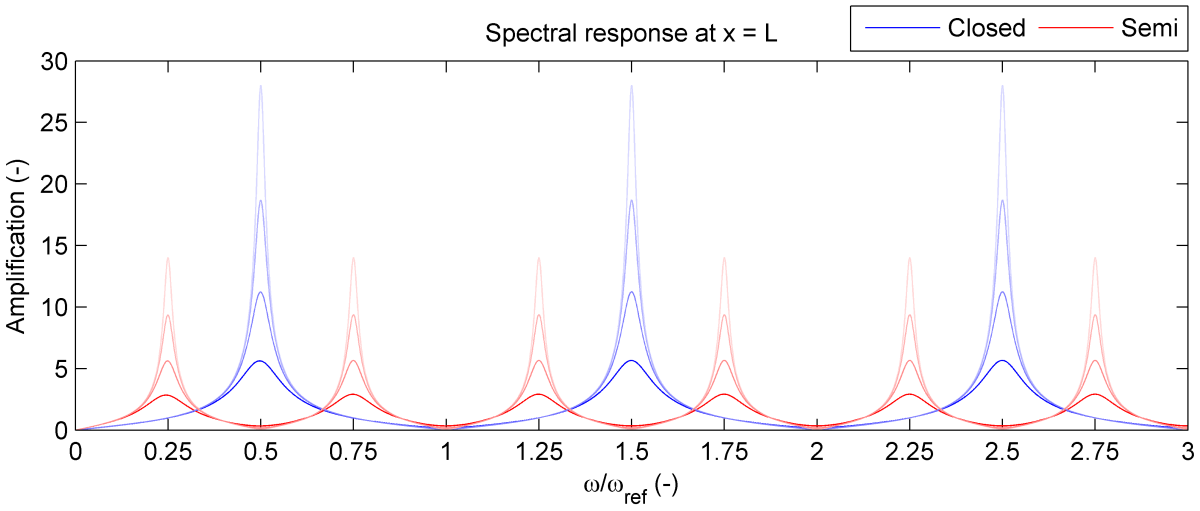

Figure 4.1: Scaled amplification factor *A* as a function of dimensionless forcing frequency ω/ω_{ref} at the rear end of the closed (blue) and semi-enclosed (red) basin with flat bed topographies. Four different descending bottom friction coefficients (r = 0.001, 0.0005, 0.0003 and 0.0002 m s^{-1}) are represented by corresponding descending color tints (dark is strongest friction) for both types of basins.

4.2 Sensitivity analysis regarding single step topography cases

In this section we will investigate the influence of the step topography on the spectral response. To study the influence of topographic elements in the basin, depth and length dimensions of the basin regions (connected by a topographic step) will be varied in the model to simulate several topographic features of the basin. In each case, the bottom friction coefficient will be varied as well to study the influence of bottom friction. In this way the sensitivity of the spectral response of the basin's surface elevation have been analyzed systematically. For each case, the closed basin results will be discussed first, followed by the semi-enclosed basin results. A reference basin length of 200 km is applied in all cases.

4.2.1 Sensitivity of the spectral response to depth ratio h_2/h_1

In this first sensitivity analysis we will study the depth ratio between depth h_2 of compartment 2 and depth h_1 of compartment 1 in our model. To cover a depth ratio h_2/h_1 ranging from 0.1 to 10, h_2 is varied between 2 and 200 m, while h_1 is kept constant to 20 m. The studied h_2/h_1 ratios are presented on a vertical log scale in Figure 4.2. The location of the topographic step will be located at the center of the basin, meaning $L_1 = L_2$ = 100 km.

Model simulations have been done with three different values of the bottom friction coefficient, representing no bottom friction (r = 0), weak bottom friction (r = 0.0002 m s^{-1}) and moderate bottom friction (r = 0.001 m s^{-1}). Figure 4.2 shows the scaled amplification factor *A* as a function of ω/ω_{ref} (horizontal axis) and the depth ratio h_2/h_1 (logarithmic vertical axis) at the rear end of the basin ($x = L$) for three bottom friction cases (a, b, c). The reference frequency ω_{ref} is derived from the reference depth $h_{ref} = h_1$. Recall from Section 4.1 that the dimensionless amplification factor *A* is defined as $A = |N_L|/N_{\mathrm{ref}}$, with $N_{\mathrm{ref}} = T/\left(\omega\sqrt{gh_{\mathrm{ref}}}\right)$.

The first case without bottom friction (Fig 4.2a) demonstrates that the classical resonance peaks appear at depth ratio $h_2/h_1 = 1$, indicated by the white line in the plots. At values below (above) this line, compartment 2 is shallower (deeper) than compartment 1. What we notice is that these resonance peaks shift to the left (right) when the depth ratio becomes < 1 (> 1). The explanation behind this behavior follows from the fact that waves in shallow water propagate more slowly than waves in deep water. This is also reflected in the expression for the propagation speed *c* of a shallow water wave: $c = \sqrt{gh}$. This means that the time (wave period) it takes for a wave to cover a cycle in the basin, increases in shallower water. The wave frequency is the reciprocal of the wave period, therefore the wave frequency decreases when the wave period increases. This means that the natural frequencies of the basin decrease (increase) when the basin becomes shallower (deeper). In order to get resonance, the forcing frequency should coincide with one of the natural frequencies of the basin. This explains that peaks will shift to the left (right), representing lower (higher) resonant frequencies, when h_2 becomes shallower (deeper) than h_1. We also notice that new peaks show up, which were absent for $h_2 = h_1$, due to breaking of symmetry.

If we now compare the frictionless case with the bottom friction cases (Figs. 4.2b & c), it is directly seen that the amplification *A* damps significantly due to bottom friction. Increasing the friction coefficient will damp the amplification even further. Also, we see that in shallower regions (below the white line) bottom friction damps the amplification to a higher degree than in deeper regions (above the white line). This can be explained by the fact that the velocity of the waves will be slowed down to a higher degree in shallower regions, which leads to larger damping of amplification.

The same sensitivity study of spectral response to depth ratio h_2/h_1 has been conducted for the semi-enclosed basin. The resulting color plots for the three bottom friction cases have been presented in Figure 4.3a-c. Based on these plots, a similar spectral response's behavior of the semi-enclosed basin to the spectral response's behavior of the closed basin is noticed.

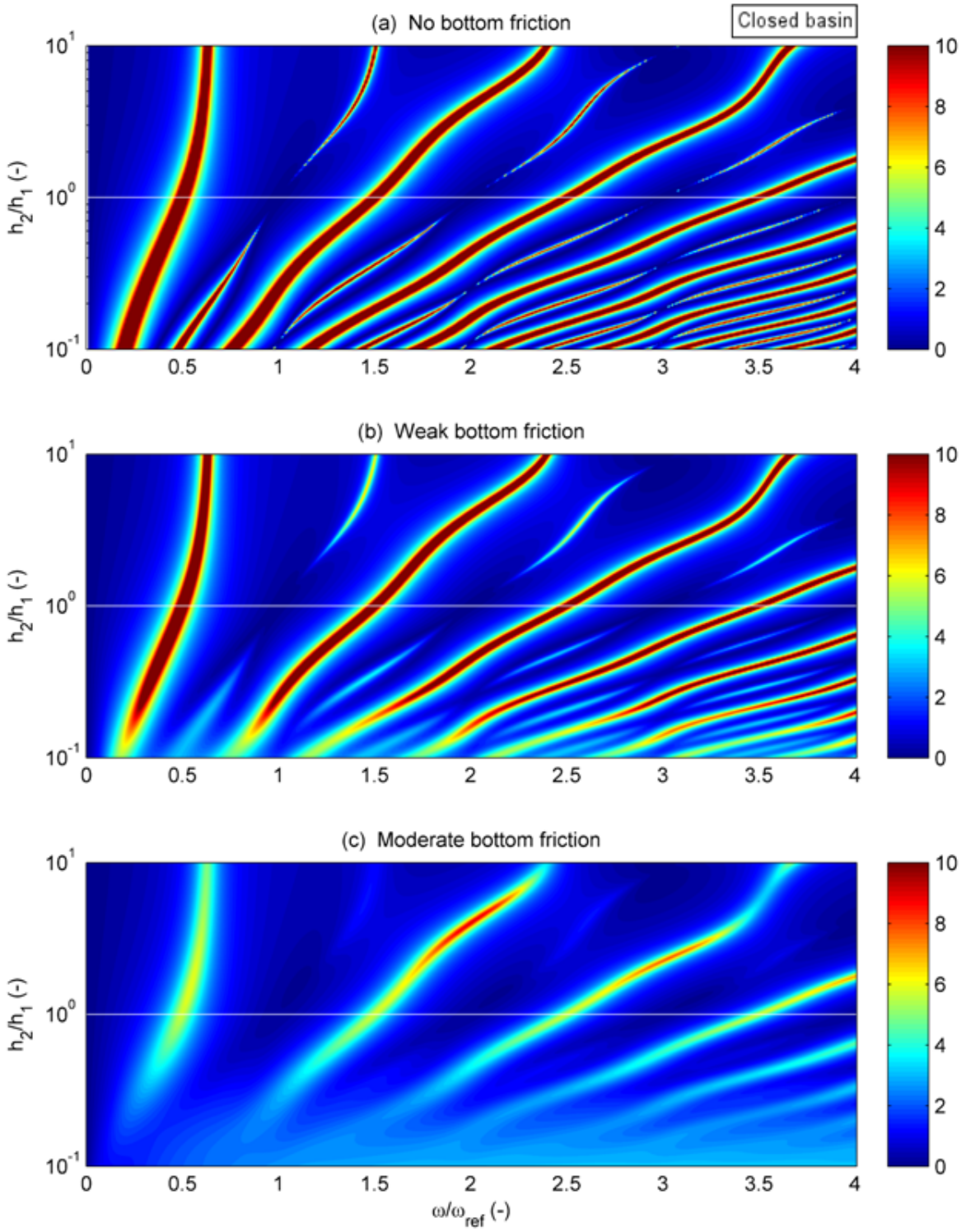

Figure 4.2: Scaled amplification factor A as a function of dimensionless forcing frequency ω/ω_{ref} (horizontal axis) and depth ratio h_2/h_1 (vertical logarithmic axis) with different bottom friction coefficients at the rear end of the closed basin ($x = L$): (a) no bottom friction ($r = 0$), (b) weak bottom friction ($r = 0.0002$ m s^{-1}), (c) moderate bottom friction ($r = 0.001$ m s^{-1}). The white line represents the flat bed topography ($h_2/h_1 = 1$), already shown in Fig. 4.1. In all cases, $h_1 = 20$ m.

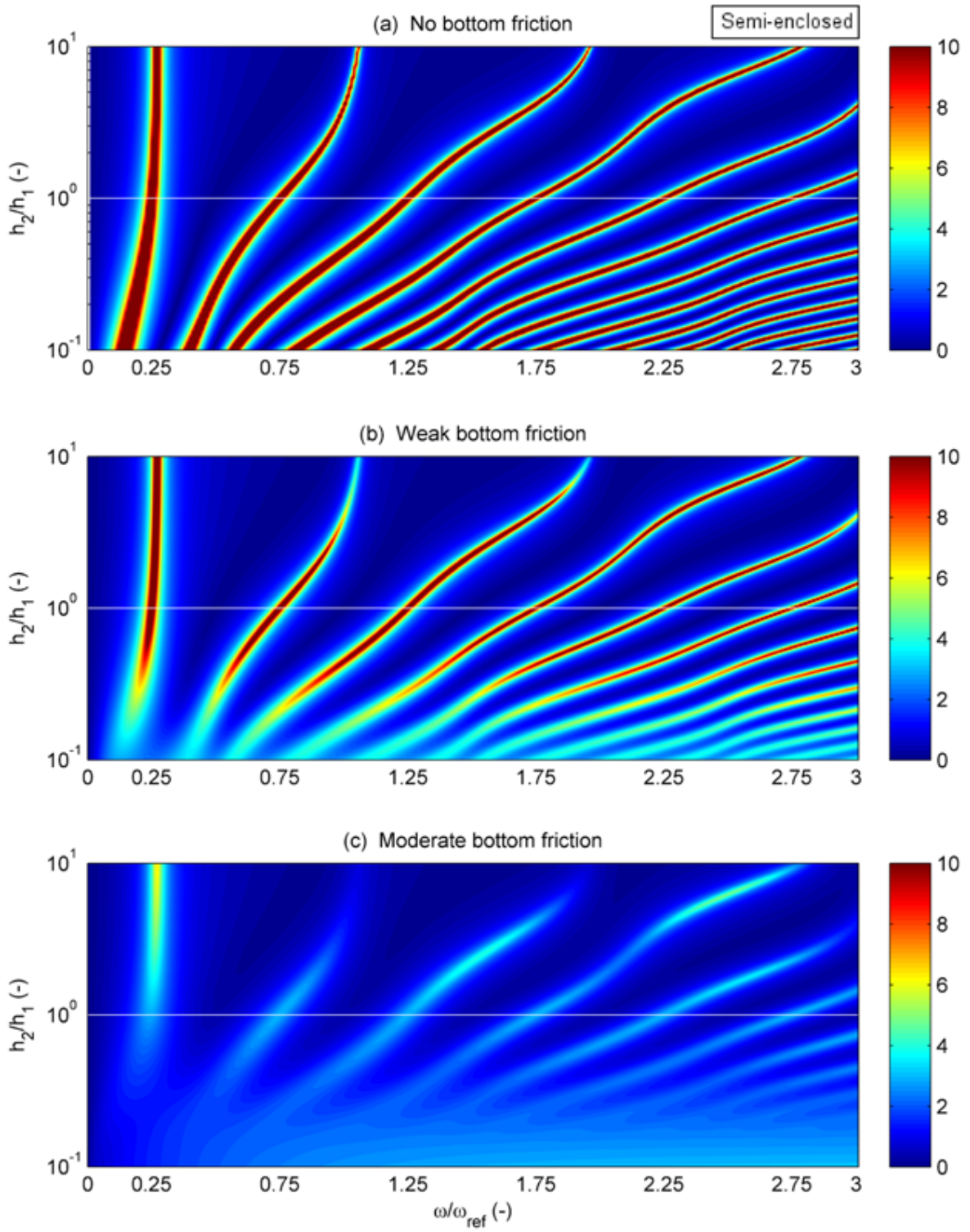

Figure 4.3: Same as Figure 4.2, but now for the semi-enclosed basin.

4.2.2 Step case with average basin depth equal to reference depth

From the previous sensitivity analyses we concluded that the basin's depth plays an important role in basin's spectral response behavior due to the relation between propagation speed and water depth: $c = \sqrt{gh}$. In this section we elaborate further on this relation by implementing a single case in the model to study the influence of the effective wave speed and the effective bottom friction on the spectral response in shallow and deep regions in the basin.

In this case the average basin depth is equal to the reference depth (20 m) of the flat bed case. Because of the 1-DH representation of the basin, the basin volume is represented by its side surface (volume per meter width). The topographic step will be located at the center (L_1 = L_2) of the basin, with h_1 = 10 m and h_2 = 30 m. The spectral response of this case will be compared with the spectral response of the flat bed case, shown in Figure 4.4. A sketch of the basin topographies is shown to the right of the plot: flat bed (black) and step (pink) topography. A weak bottom friction coefficient is applied for both cases in the closed basin.

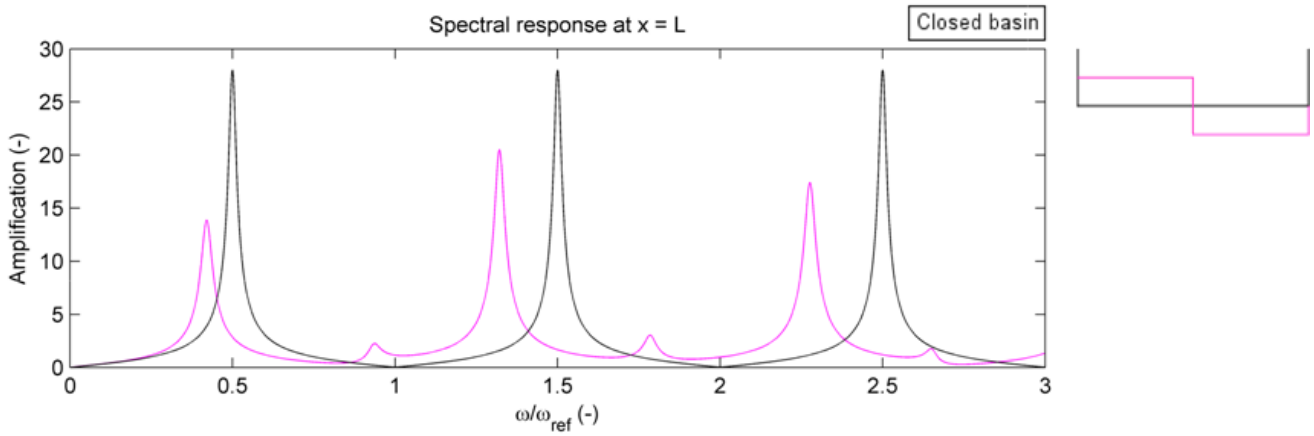

Figure 4.4: Scaled amplification factor *A* at the rear end of the closed basin (*x* = *L*), as a function of dimensionless forcing frequency ω/ω_{ref} for a step topography case (h_1 = 10 m, h_2 = 30 m; pink) compared to the flat bed case (black). With h_{ref} = 20 m and weak bottom friction (r = 0.0002 m s^{-1}) for both cases. A side view of the corresponding basin topographies is presented at the upper right.

Figure 4.4 shows that the peaks in this step topography case will shift to the left compared to the flat bed case, while the total volume in the basin remains the same. This suggests that the shallower region in the basin dominates the deeper region. This can be explained by the difference in effective wave speed in the two cases. The effective wave speed in the flat bed case follows from $c_{\text{flat}} = \sqrt{gh_{\text{ref}}} =$ 14.01 m s^{-1}. The effective wave speed in the step topography case is the average of the sum of the wave speeds of both compartments: $c_{\text{step}} = \left(\sqrt{gh_1} + \sqrt{gh_2}\right)/2 =$ 13.53 m s^{-1}. This shows that the effective wave speed in the step topography case is lower than in the flat bed case. As already explained, due to a lower effective wave speed in the basin the natural frequencies of the basin decrease. Therefore resonant frequencies will be lower, meaning peaks will shift to the left.

Furthermore, we notice from Figure 4.4 that the peaks in the step case are lower than the peaks in the flat bed case. This can be explained by the fact that bottom friction is dominating in the shallower part of the step case and therefore effectively damps the peaks to a higher degree than in the flat bed case. Again we will apply an heuristic approach to illustrate the difference in influence of

bottom friction on the spectral response between both cases: the bottom friction contribution is represented by the friction term $r\bar{u} \cdot h^{-1}$ of the momentum equation (3.13). For simplicity we assume that the depth-averaged flow velocity remains more or less the same with changing depth. Thus, for a constant r, the effective friction coefficient is represented by h^{-1}. It turns out that ½ (h_1^{-1} + h_2^{-1}) > h_{ref}^{-1}, which indicates that the effective friction in the shallower part dominates the effective friction in the deeper part of the step case. This supports our observation of the lowered peaks in the step case. In addition, smaller peaks show up in between the classical resonance peaks due to breaking of symmetry in the step topography case (as already mentioned before in Section 4.2.1).

The same case has been implemented in the semi-enclosed basin model as well, shown in Figure 4.5. Similar results as in the closed basin model have been found, aside from the peaks due to breakdown of symmetry.

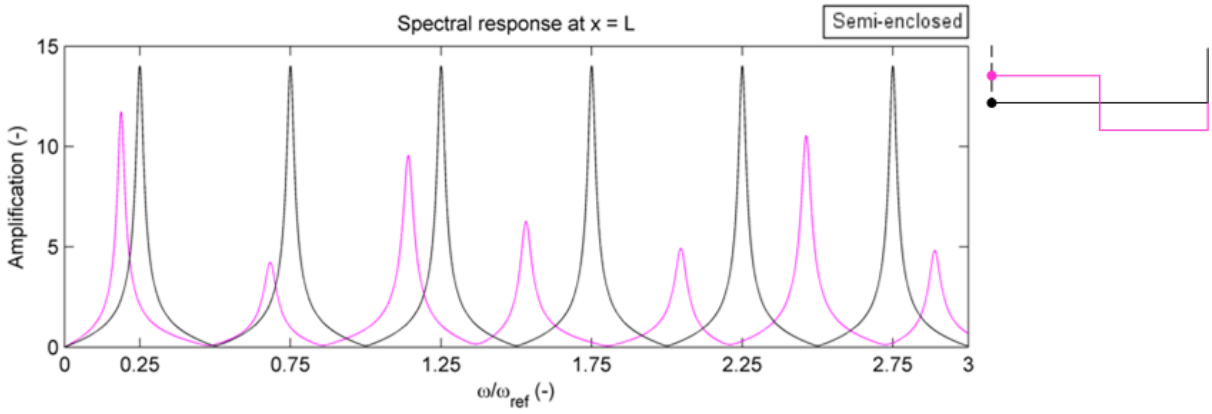

Figure 4.5: Same as Figure 4.4, but now for the semi-enclosed basin.

4.2.3 Sensitivity of the spectral response to the h/L ratio of shoals and pits

In this section we will simulate topographic elements such as shoals and pits, by redistributing sand in the basin. This means that the volume of the basin remains constant for each case. The volume of the basin is represented by the side surface of our reference basin: 20 m x 200 km = 4 x 10^6 m^2 (volume per meter width). A fixed amount of sand will be redistributed from one compartment to the other. This amount of sand corresponds with the surface of the shoal and the pit design and is set to 5 x 10^5 m^2 (volume per meter width). By varying the basin dimensions in the model, various shoal and pit cases can be simulated and studied systematically. Because of the model's single step topography, only rectangular shoals and pits can be simulated. The influence of the basin topography distribution on the spectral response will be studied regarding the height/length ratio of the element (pit or shoal). The height of the element is represented by the difference between the two compartment depths (h_2 – h_1), the length of the element is represented by the length of compartment 2 (L_2): $h_{element} = h_2 - h_1$; $L_{element} = L_2$.

Figures 4.6 and 4.7 present examples of shoal and pit implementations in the model. In Figure 4.6a, the sand is cumulated at a small length L_2, which gives a relatively large shoal height. Figure 4.6b shows a shoal smeared out over a greater length L_2, which gives a relatively small shoal height. Figure 4.6a thus has a larger h_{shoal}/L_{shoal} ratio than Fig 4.6b. Likewise, two different pit distributions are shown in Figure 4.7, where Fig 4.7a has a larger h_{pit}/L_{pit} ratio than Fig 4.7b. For both the shoal and the pit design, h_1 remains constant and is set to 22.5 m and 17.5 m respectively.

Reference depth h_{ref} is set to 20 m. In the shoal cases, h_2 is varied between 2.5 and 20 m. In the latter case, where h_2 is 20 m, the sand is completely smeared out over the basin length and the basin becomes a flat bed with a reference depth of 20 m. In the pit cases, h_2 is varied between 20 and 37.5 m. For each case, the length of the element (L_2) follows from the surface (5 x 10^5 m^2) divided by the height of the element. The height of the element is set to h_2 - h_1, which means that the h/L ratio of the pit (shoal) is positive (negative). In this way the sensitivity of the spectral response to the h/L ratio of a pit and shoal design can be compared in a single color plot with positive and negative h/L values respectively. The larger the $h_{element}/L_{element}$ ratio, both positive and negative, the more cumulated the element is distributed over the basin. As already mentioned, Figures 4.6a and 4.7a have larger $h_{element}/L_{element}$ ratios than Figures 4.6b and 4.7b.

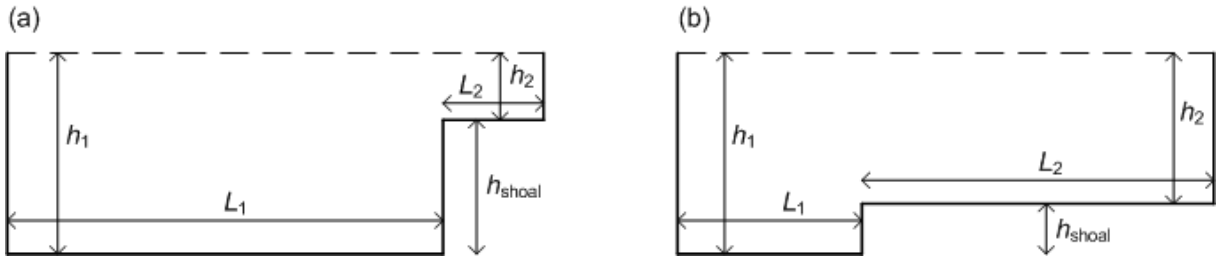

Figure 4.6: Side view sketches of the closed basin topography representing examples of **shoal designs**: (a) relatively large h_{shoal}/L_{shoal} ratio, (b) relatively small h_{shoal}/L_{shoal} ratio. L_2 is equal to L_{shoal}. The still water level is represented by the dashed line and h_1 = 22.5m.

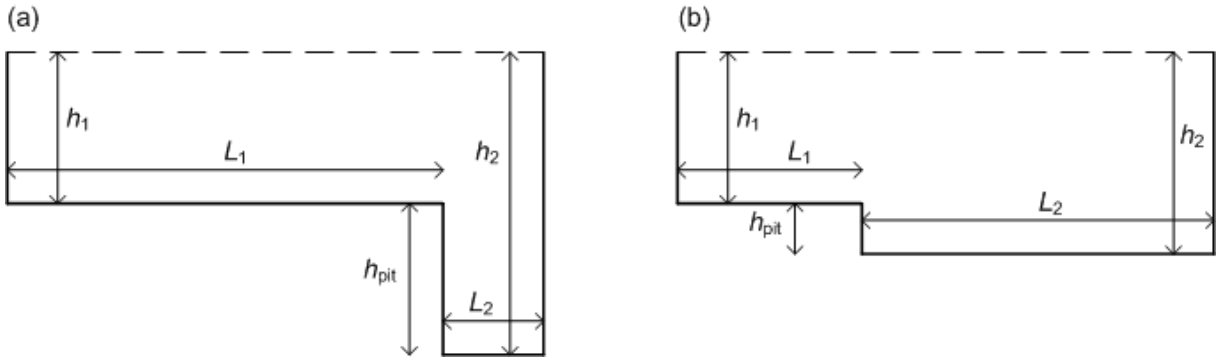

Figure 4.7: Same as Fig 4.6, but now for the **pit designs**. Notice that h_1 (17.5 m) in the pit design < h_1 (22.5 m) in the shoal design.

First we will present the results of the shoal and pit cases with weak bottom friction. Because the cases without bottom friction show similar amplification behavior as the weak bottom friction cases, what we have seen in Section 4.2.1 as well, the frictionless cases will not be presented anymore. The results are presented in Figure 4.8 for the closed (a) and semi-enclosed (b) basin, where positive (negative) $h_{element}/L_{element}$ – values on the vertical axes represent the pit (shoal) cases.

We first notice in the color plots that wiggles appear close to the h/L ratios of zero. These wiggles appear due to the applied non-logarithmic vertical scale, whereby values close to zero are squeezed together. Applying a log scale will prevent this. What we further notice from the plots for both the closed and semi-enclosed basin, is that the amplification of the resonant peaks of the pit design decreases when the h_{pit}/L_{pit} ratio increases, except for the first resonant peak in both plots. This tendency is to a lesser extent also present in the amplification of the resonant peaks of the shoal design, especially in the first resonant peak in both plots. Overall, the amplification is lower in the pit design than in the shoal design, given that the basin volume is constant in all cases.

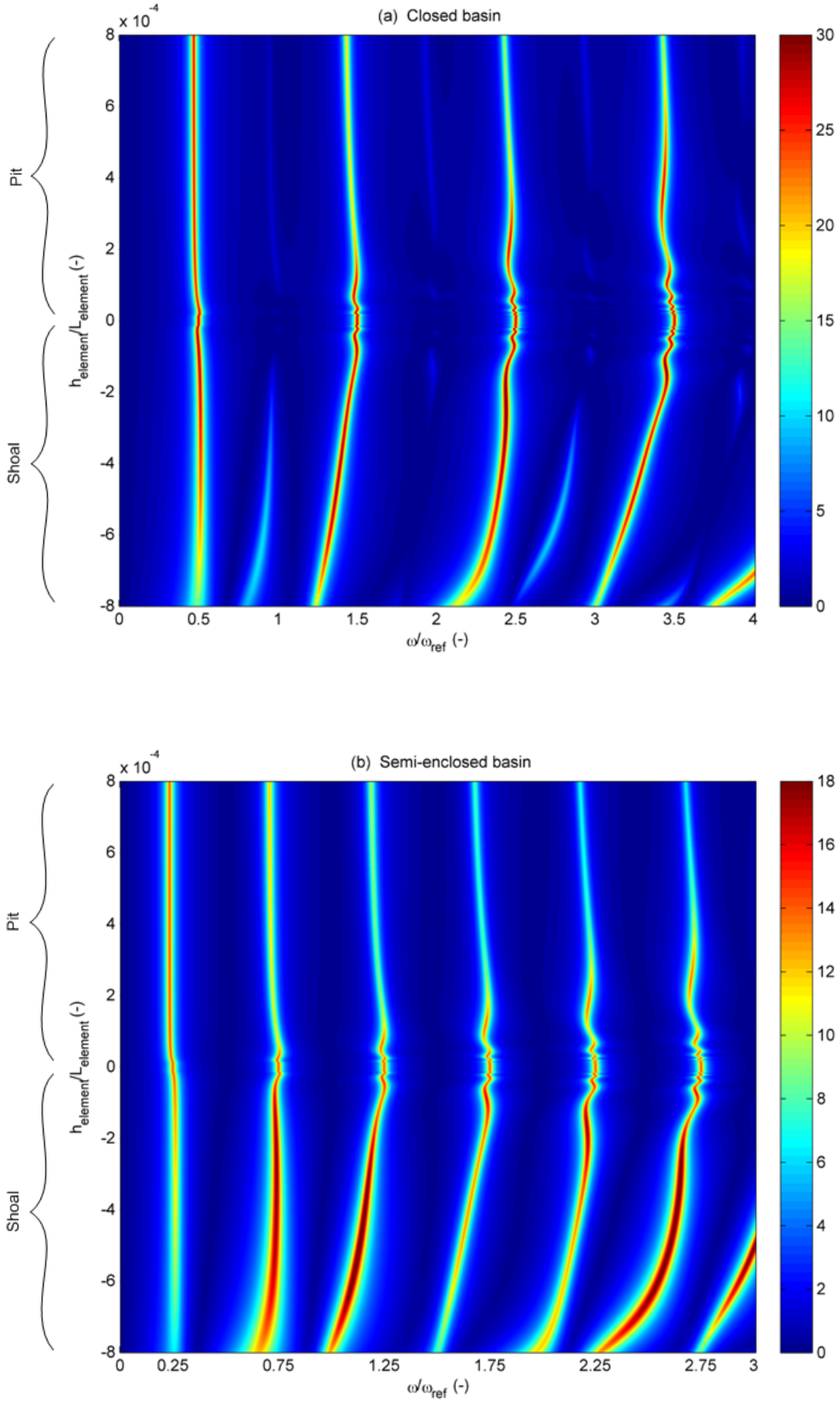

Figure 4.8: Scaled amplification factor A as a function of dimensionless forcing frequency ω/ω_{ref} (horizontal axis) and ratio $h_{element}/L_{element}$ (vertical axis) at the rear end of the basin ($x = L$): (a) closed basin, (b) semi-enclosed basin. Positive (negative) ratios on the vertical axis represent pit (shoal) cases. r = 0.0002 m s^{-1}, h_{ref} = 20 m.

Furthermore, we notice a tendency of peaks shifting slightly to the left when the h_{shoal}/L_{shoal} ratio increases in the shoal design, which is barely notable in the pit design. This can be explained by effective wave speed differences due to increased depth differences in the basin when the ratio increases. The effective wave speed in a step topography case with equal compartment lengths, i.e. L_1 = L_2 = 100 km, equals the average of the sum of the wave speeds in both compartments (as explained in the previous section). Only in these cases the compartment lengths differ. This means that the effective wave speed in the basin can be derived by taking the weighted average of the sum of the wave speeds of both compartments: $c_{\text{step}} = \alpha\sqrt{gh_2} + (1-\alpha)\sqrt{gh_1}$, with α = L_2/L_{tot} and L_{tot} denotes the total length of the basin (200 km). Here, the effective wave speed is the same in the closed and semi-enclosed basin for a certain case. The effective wave speeds of the shoal and pit cases presented in Figure 4.8 are plotted as a function of $h_{element}/L_{element}$ in Figure 4.9. This figure shows that the effective wave speed decreases as $h_{element}/L_{element}$ increases for both the shoal and the pit design. It also shows that the shoal design has more influence on the effective wave speed in the basin, which explains the larger peak shifts of the shoal design with respect to the pit design in Figure 4.8.

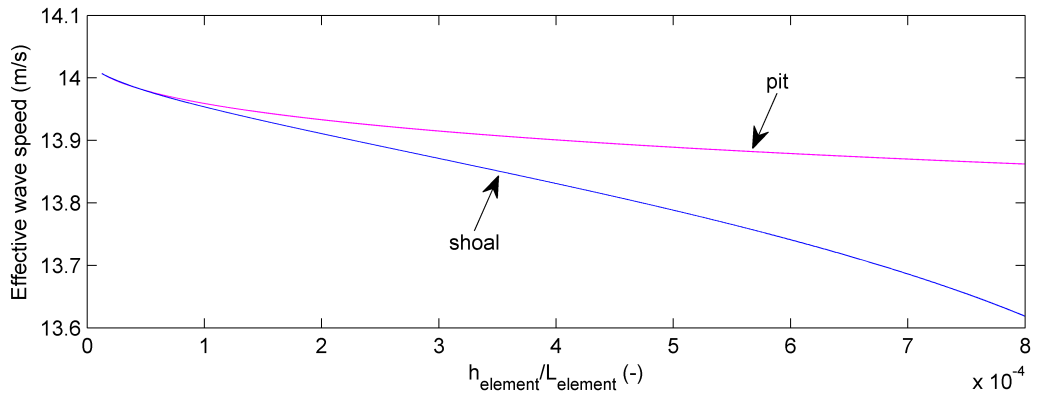

Figure 4.9: Effective wave speed as a function of h_{shoal}/L_{shoal} and h_{pit}/L_{pit} for the shoal (blue line) and pit (pink line) cases presented in Fig. 4.8.

The influence of bottom friction on the spectral response of the shoal and pit cases are presented in Figures B.1 and B.2 in Appendix B. The cases are simulated with moderate bottom friction and compared with the weak bottom friction results at lower amplification values of the color axis. The results show that increasing bottom friction will damp the amplification, what we already concluded in previous sections. Also, it illustrates more clearly that peaks due to breaking of symmetry show up mainly in the shoal design at larger values of the h_{shoal}/L_{shoal} ratio in the closed basin plots. This effect is barely visible in the pit design.

4.3 Summary

At first, the results of our analytical 1-DH model illustrate that the reference cases in the closed and semi-enclosed basin display spectral response peaks which coincide with the classical resonance peaks for these types of basins.

The results further show that topographic variations in general causes these resonance peaks to shift in the frequency domain, through their effect on effective wave speed. This can be explained by the fact that waves in shallow water propagate more slowly than waves in deep water. Due to breaking of symmetry, new peaks show up in the spectral response of the closed basin.

Moreover, the results point out that the spectral response of a step topography case displays lower peaks at lower frequencies compared to the flat bed case with the same basin volume, for both the closed and the semi-enclosed basin. This is explained by the fact that the effective bottom friction as well as the effective wave speed of the shallower region dominates the effective bottom friction and the effective wave speed of the deeper region.

Finally we have studied the influence of topographic elements, such as shoals and pits, on the spectral response, by varying the height/length ratio of the element, while remaining a constant basin volume. In general, it turns out that the resonant peaks of the pit cases are lower than the shoal cases. Furthermore, the spectral responses of the shoal cases show that the peaks slightly shift to lower frequencies as the height/length ratio of the shoal increases, due to effective wave speed differences.

Overall, we have found that increasing bottom friction lowers the resonant peaks of the spectral response of all studied cases. In the next chapter we will extend the possibilities of simulating topographic elements and adding cross-basin dynamics in the basin by using the 3-D FEM model.

Chapter 5

Results of the FEM model

In this chapter we will perform case studies of the closed and semi-enclosed basin with a strongly simplified geometry, but with more realistic and complex topographies compared to the 1-DH cases in the previous chapter, using the 3-D FEM model of W.L. Chen et al. (2016). The model settings will be treated in Section 5.1, regarding the model domain, grid characteristics, friction parameters and number of frequency modes.

Despite a few essential differences between the FEM model and the 1-DH model, certain simple cases can be simulated in a similar way by both models. To get an impression of how well the semi-analytical FEM model simulations match the analytical 1-DH model simulations, a comparison analysis will be conducted in Section 5.2 by reproducing the spectral responses of simple cases in the 1-DH model by simulations of similar cases in the FEM model. At the same time, the bottom friction coefficient r of the 1-DH model will be calibrated to two different values, representing weak and moderate bottom friction, of the bottom friction coefficient s (and a fixed K_v value) of the FEM model using along-basin wind forcing in the flat bed cases of both types of basins. In turn, a few along-basin wind cases regarding shoal and pit implementations over the full width of both types of basins (Section 5.2.3) and a cross-basin wind case regarding a flat bed in the closed basin (Section 5.2.4), will be reproduced in the FEM model and compared with similar 1-DH cases that were simulated with the in Section 5.2.2 calibrated r-coefficients.

In Section 5.3 we will perform FEM model simulations to study the sensitivity of the location of a topographic element on the basin's spectral response along the coast, subject to along- and cross-basin wind forcing, by varying the topographic elements over a few locations in front of the coast. The shoal simulations will be treated in Section 5.3.1, followed by the pit simulations in Section 5.3.2 for both types of basins.

The sensitivity analysis will be further expanded in Section 5.4 by conducting similar simulations as in Section 5.3, subject to 30° and 60° wind angle forcing. Here the results will be treated relative to specific evaluation points along the coast, to see the effects of the location of the topographic elements on the basin's spectral response from a different perspective. The spectral responses of the flat bed cases subject to the same wind angle forcing will serve as reference cases for a better interpretation of the results of the topographic element cases.

5.1 General model settings

Just like in the 1-DH model, the model domain consist of a rectangular basin with a length of 200 km and a width of 100 km. The reference depth of the basin is set to 20 m. The model domain can be represented by a structured or an unstructured grid in the FEM model. An example of both types of grids is presented in Figure 5.1. An uniformly structured grid is preferred when the model domain consists of a simple geometry, because of the fixed connectivity pattern of the elements (forming the grid). On the other hand, an unstructured grid is preferred when grid flexibility is required to increase resolution at local regions of the model domain, e.g. due to complex geometric and/or topographic

features in near-shore regions (Guo et al., 2009). This means that the grid is formed with elements of adaptable size, clearly illustrated in Figure 5.1b.

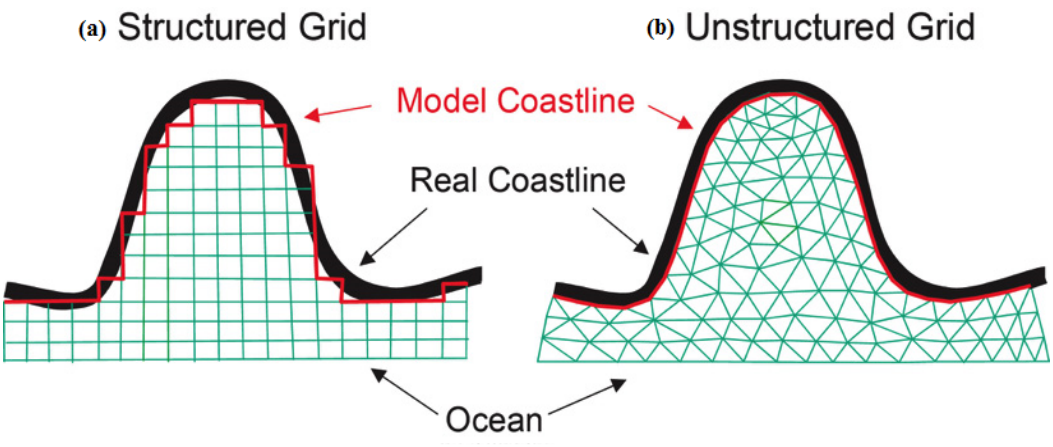

Figure 5.1: An example of fitting a structured grid (a) and an unstructured grid (b) to a simple coastal embayment. The true coastline is shown in black, the model coastline in red. Note how the unstructured triangular grid can be adjusted so that the model coastline follows the true coastline, while the structured grid coastline is jagged – which can result in unrealistic flow disturbance close to the coast (C. Chen et al., 2006).

In this study our simplified model domain allows us to apply a structured grid. The element size is set to 4 km, resulting in a set of 4581 structured triangles in the model domain. Reducing the element size will increase simulation time considerably.

Throughout this chapter we have applied multiple frequency ranges, with at least 300 modes per case simulation to assure a high accuracy of model simulations. For some cases, mostly in Section 5.3 and 5.4, we have extended this range to study certain tendencies outside this range. The reason for this is that the strongest influence on the basin's spectral response is found at the highest frequencies of the studied ranges, discussed later. These studied ranges are based on the applied frequency ranges in Chapter 4. The step size of these ranges were based on a percentage of the reference frequency ω_{ref}[1]: 0.01* ω_{ref} to be precise. This resulted in a high accuracy of exciting the resonant frequencies by our periodic wind forcing. With M = 300-400 modes, our frequency ranges applied in this chapter varies between M*(0.01* ω_{ref}), with inclusion of ω = 0 needed in Chapter 6 to define the steady response to a single wind event (transient state). By choosing 300 modes, each case simulation will take approximately 3 hours of computational time, with the addition that the closed basin simulations takes more computational time than the semi-enclosed basin simulations (order of half an hour).

The vertical eddy viscosity parameter (K_v), which adds turbulence to the system, is assumed uniform over the water depth in the basin and is set to a constant value over the whole domain: K_v = 0.012 m^2 s^{-1} (default value FEM model). In addition, the slip parameter for the simulations after calibration is set to s = 5 x 10^{-4} m s^{-1}. Later, in Section 5.2.3 the simulations based on the default K_v value will be compared to 1-DH model simulations in a steady state condition, after calibrating the r parameter of the 1-DH model for fixed values of the s parameter in the next section. This will give an indication of how realistic this value is compared to the 1-DH model approach of simulating this

[1] See definition in Section 4.1, Eq. (4.3).

process. Furthermore, all FEM model simulations treated in this report are conducted with the default K_v value, while varying the *s* parameter in various cases throughout this chapter.

5.2 Comparison between the FEM model and the 1-DH model

Before we perform sensitivity analyses with cases in the FEM model, we first try to reproduce the spectral response simulations of suitable cases in the 1-DH model with similar cases in the FEM model. Because of the simplifications in the 1-DH model, the FEM model cases are not completely identical to the 1-DH model cases. Nevertheless, it will allow us to link the friction coefficients of both models: (K_v, *s*) vs. *r*. In this section, the FEM and 1-DH model simulations are calculated based on 300 frequency modes (*M* = 300).

5.2.1 Flat bed topography without bottom friction

We begin the comparison with the most simple case in both models, a flat bed topography in the closed and semi-enclosed basin without bottom friction. The 1-DH model settings for this case are: *L* = 200 km, *h* = 20 m (width of the basin is neglected) and bottom friction coefficient *r* = 0. The FEM model settings for this case are: *L* = 200 km, *B* = 100 km, *h* = 20 m and bottom friction coefficient *s* is set close to zero (10^{-10} m s^{-1}). In both models the wind is forced in along-basin direction. The resulting spectral response at the rear end of the basin (*x* = *L*) of the 1-DH model case will be compared to the spectral response at the lower right corner of the basin (*x* = *L*, *y* = 0) of the FEM model case. Here we will use the scaled amplification factor *A* to plot the spectral response of both model simulations. Recall that $A = |N|/N_{\mathrm{ref}}$, treated already in Chapter 4. The results of the 1-DH model case (black peaks) and the FEM model case (pink peaks) for both the closed (a) and semi-enclosed basin (b) are presented in a single plot in Figure 5.2. The closed (semi-enclosed) basin results are reflected in the classical resonance peaks at odd integers of 0.5 (0.25) at the horizontal frequency axis. As we can see from the plots, both model simulations match fairly well. Due to the lack of bottom friction in these cases, extreme amplification of the resonant peaks occurs. The differences in peak heights between the model simulations do not really matter at this scale. These differences will be smaller when we include bottom friction, what we will see in the following sections.

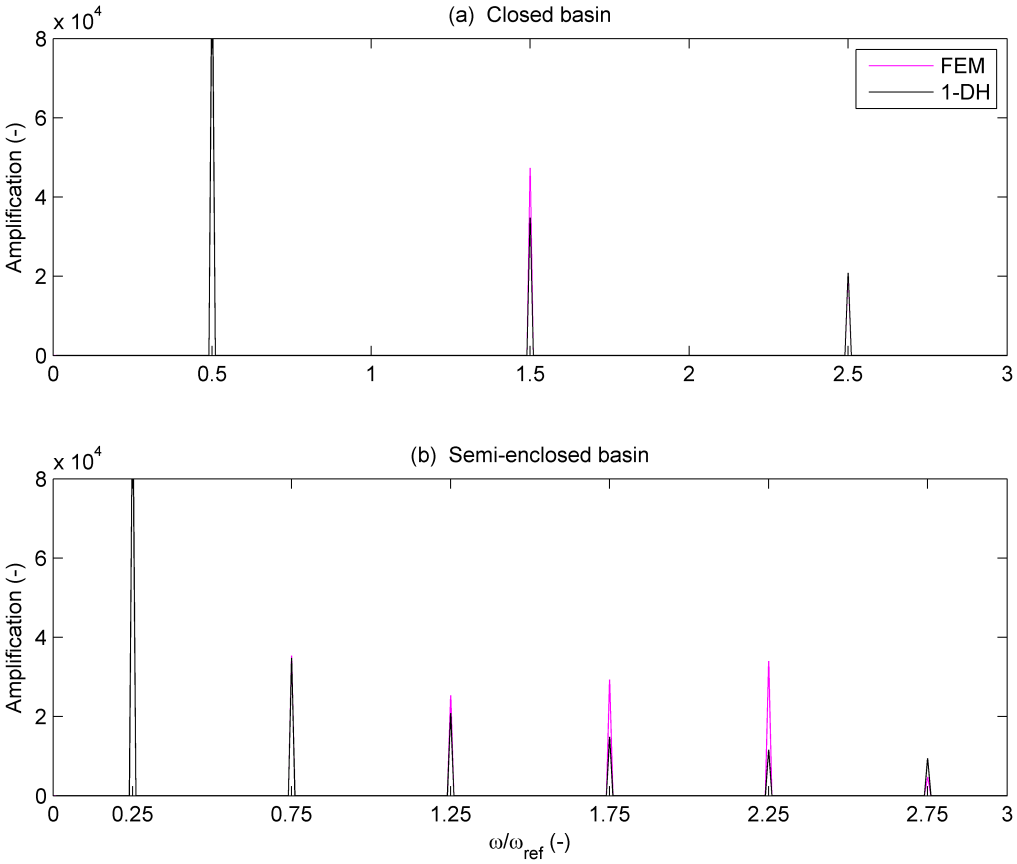

Figure 5.2: Scaled amplification factor *A* as a function of dimensionless frequency ω/ω_{ref} of the flat bed topography at the rear end of the closed and semi-enclosed basin: 1-DH model results (black) versus FEM model results (pink).

5.2.2 Calibration of bottom friction coefficient *r* of the 1-DH model

In this section, the bottom friction coefficient *r* of the 1-DH model will be calibrated to two fixed values of the bottom friction coefficient *s* of the FEM model. To simulate weak and moderate bottom friction, Chen has used in recent studies (Chen et al., 2014 & Chen et al., 2015) the following two coefficient values in the FEM model: $s = 10^{-4}$ m s^{-1} (weak bottom friction) and $s = 10^{-3}$ m s^{-1} (moderate bottom friction). In order to find corresponding *r*-values for the 1-DH model, the flat bed simulations in the 1-DH model have been calibrated to the flat bed simulations in the FEM model for both bottom friction coefficients in both types of basins. To this end, various *r*-values close to the corresponding *s*-values for weak and moderate bottom friction have been implemented in the 1-DH model to find the best fit with the FEM simulations. To determine the goodness of fit of the 1-DH simulations with the FEM simulations, we use the statistical measure 'standard error of the estimate' (Lane, 2015):

$$\sigma_{est} = \sqrt{\frac{\sum_{m=1}^{M} |(N_m - N'_m)^2|}{M}}, \tag{5.1}$$

where σ_{est} is the standard error of the estimate. *N* is the complex amplitude of the surface water elevation at evaluation point $x = L$ and $y = 0$ of the FEM model simulation. *N*' is the complex amplitude of the surface water elevation at evaluation point $x = L$ of the 1-DH model simulation. The complex amplitudes are calculated as a function of frequency, where *m* is the frequency mode index

and *M* is the total number of frequency modes. Here we will determine the goodness of fit over the full frequency domain, which implies that *M* = 300 and ω_{min} = 4.4005 x 10^{-6} rad s^{-1}. One could also focus on a more limited number of frequency modes, e.g. a few frequency modes around a resonant mode, to conduct the calibration at. The smaller the value of the standard error, the better the 1-DH model simulations fit the FEM model simulations.

For weak bottom friction, the best fit is found for *r*-values of 9.5 x 10^{-5} m s^{-1} (closed basin) and 9.3 x 10^{-5} m s^{-1} (semi-enclosed basin) with corresponding standard errors (σ_{est}) of 2.1 x 10^{-3} and 1.8 x 10^{-3} respectively. If we plot the two model simulations in one graph (not shown here), the differences are barely visible for both the closed and the semi-enclosed basin. Therefore it can be stated that the simulations of both models match quite well for the weak bottom friction case in both types of basins.

On the other hand, for moderate bottom friction the best fit is found for *r*-values of 6.5 x 10^{-4} m s^{-1} (closed basin) and 5.9 x 10^{-4} m s^{-1} (semi-enclosed basin) with corresponding standard errors of 1.38 x 10^{-2} and 1.19 x 10^{-2} respectively. The standard errors for moderate bottom friction are larger than the standard errors for weak bottom friction, which means a less good fit for the moderate bottom friction cases over the full frequency domain (*M* = 300). To visualize these differences between the 1-DH simulations and the FEM simulations, the absolute values of the complex amplitudes *N* and *N'* for the moderate bottom friction cases in both types of basins have been plotted in Figure 5.3. Note that these plotted values are not the scaled version as we used to plot the spectral response. In order to illustrate the simulation differences between the two models more clearly, the 1-DH model results will be displayed in pink from now on. Figure 5.3 shows that both model simulations fit reasonably well.

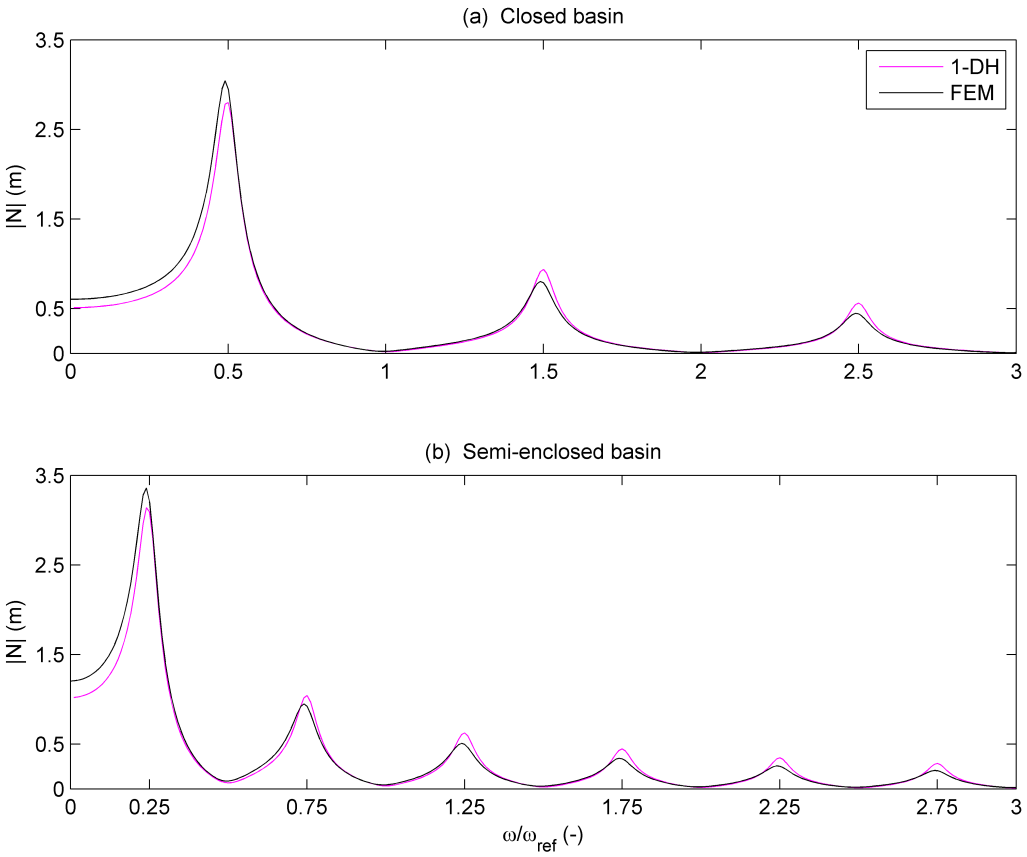

Figure 5.3: Spectral response |*N*| as a function of dimensionless frequency $\boldsymbol{\omega/\omega_{ref}}$ of the flat bed topography at the rear end of the closed (a) and semi-enclosed (b) basin. FEM model results (black) versus 1-DH model results (pink), with moderate bottom friction: *r* = 6.5 x 10^{-4} (a) & 5.9 x 10^{-4} m s^{-1} (b), *s* = 10^{-3} m s^{-1} (a & b).

However, when we plot the scaled amplification factor *A* for the same model simulations (see Figure 5.4), we notice that the peaks of the 1-DH simulations remain (almost) constant for increasing frequencies in contrast to the peaks of the FEM simulations, which decrease for increasing frequencies. We saw this behavior of the 1-DH resonant peaks in the flat bed case already in Chapter 4 for several bottom friction coefficients (Fig. 4.1). This is an important difference between both model simulations, which is possibly a consequence of featuring 1-DH versus 3-D dynamics.

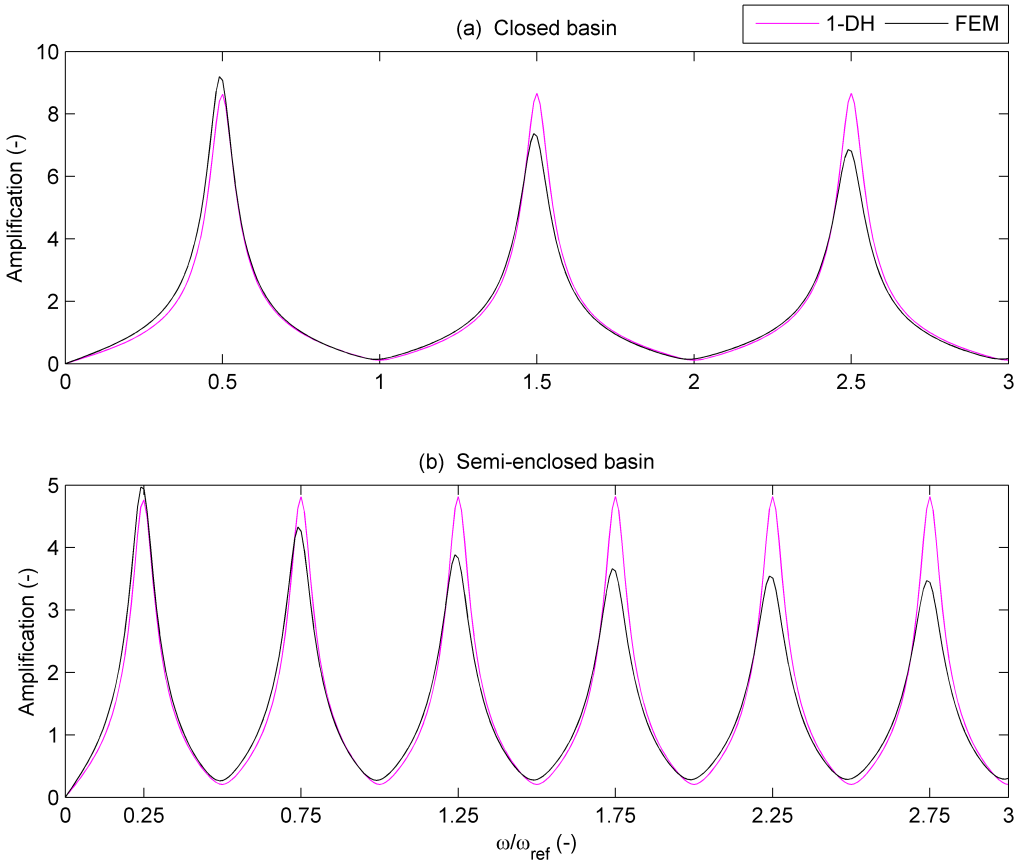

Figure 5.4: Same as Fig. 5.3, but now with the scaled amplification factor *A* at the vertical axis.

Finally, the calibrated *r* values for the four reference cases have been presented in Table 5.1.

	No friction	Weak friction	Moderate friction
s (closed & semi) [m s^{-1}]	10^{-10}	10^{-4}	10^{-3}
r (closed) [m s^{-1}]	0	9.5 x 10^{-5}	6.5 x 10^{-4}
r (semi) [m s^{-1}]	0	9.3 x 10^{-5}	5.9 x 10^{-4}

Table 5.1: Bottom friction coefficients *s* (FEM model) and *r* (1-DH model) for the closed and semi-enclosed basin simulations.

5.2.3 Comparison of the roughness parameters in a steady flow condition

As already mentioned in Section 5.1, all the FEM model simulations in this study have been done with a default K_v value (0.012 m^2 s^{-1}). Now that bottom friction coefficient *r* is calibrated for both types of basins, we can determine how realistic this default K_v value is. In Appendix C, we have

expressed r with the roughness parameters in the FEM model (s, K_v) by expressing the 3-D flow velocity in a 1-DH flow velocity, assuming steady flow (ω = 0). The result of this derivation in the appendix, resulted in

$$r = \frac{1}{\frac{1}{2K_v}h + \frac{1}{s}} . \qquad (C.15)$$

Now we can calculate four different K_v values for weak and moderate bottom friction in the closed and semi-enclosed basin, with corresponding values for r and s presented in Table 5.1 in the previous section. We have presented the calculated K_v values for these four cases with h = 20 m in Table 5.2.

	Weak friction	Moderate friction
Closed basin	0.019	0.0186
Semi-enclosed basin	0.0133	0.0144

Table 5.2: Calculated K_v values for four reference cases, compared to default value: 0.012 [$m^2 s^{-1}$].

The above results show that the default K_v value matches quite well with the 1-DH approach of the FEM model for the semi-enclosed basin and to a lesser extent also for the closed basin. For the purpose of this study, this comparison is sufficient enough to conclude that the applied default value for the FEM simulations is realistically representing the roughness and turbulence in both types of basins.

5.2.4 Shoal and pit implementation over the full width of the basin

Implementing a shoal or a pit in the basin of the 1-DH model can be considered as a shoal or pit that covers the full width of the basin, because the width in the 1-DH model is considered to be very small. A similar case can be simulated in the FEM model by implementing a shoal or a pit over the full width of the basin. Unlike the 1-DH model, the FEM model can implement topographic elements with a smooth transition of the pit (or the shoal). A pit is simulated more naturally by specifying a smoothed slope length in the horizontal x and y directions. A 3-D sketch of such a pit implementation is illustrated in Figure 5.5a, after the example of Roos et al., 2008. A 2-D sketch of the pit profile is shown in Figure 5.5b, c.

The shoal is constructed in the same way. In this study the smoothed slope length S is set to 8 km, which is a valid integer of the chosen element size (4 km) of the FEM model. A cosine function is applied to simulate the smoothed slope of the shoal and the pit. We can also simulate a step topography in the FEM model by setting a very small slope length (i.e. L_{slope} = 10 m) to connect better to the 1-DH model simulations. In this section we compare both FEM model simulations (FEM smooth & FEM step) with the 1-DH model simulation for different bottom friction coefficients.

Moreover, the sloping bed topography in the FEM model is constructed in such a way that it connects with the 1-DH single step topographies that were studied in Chapter 4, clearly illustrated in Figure 5.7.

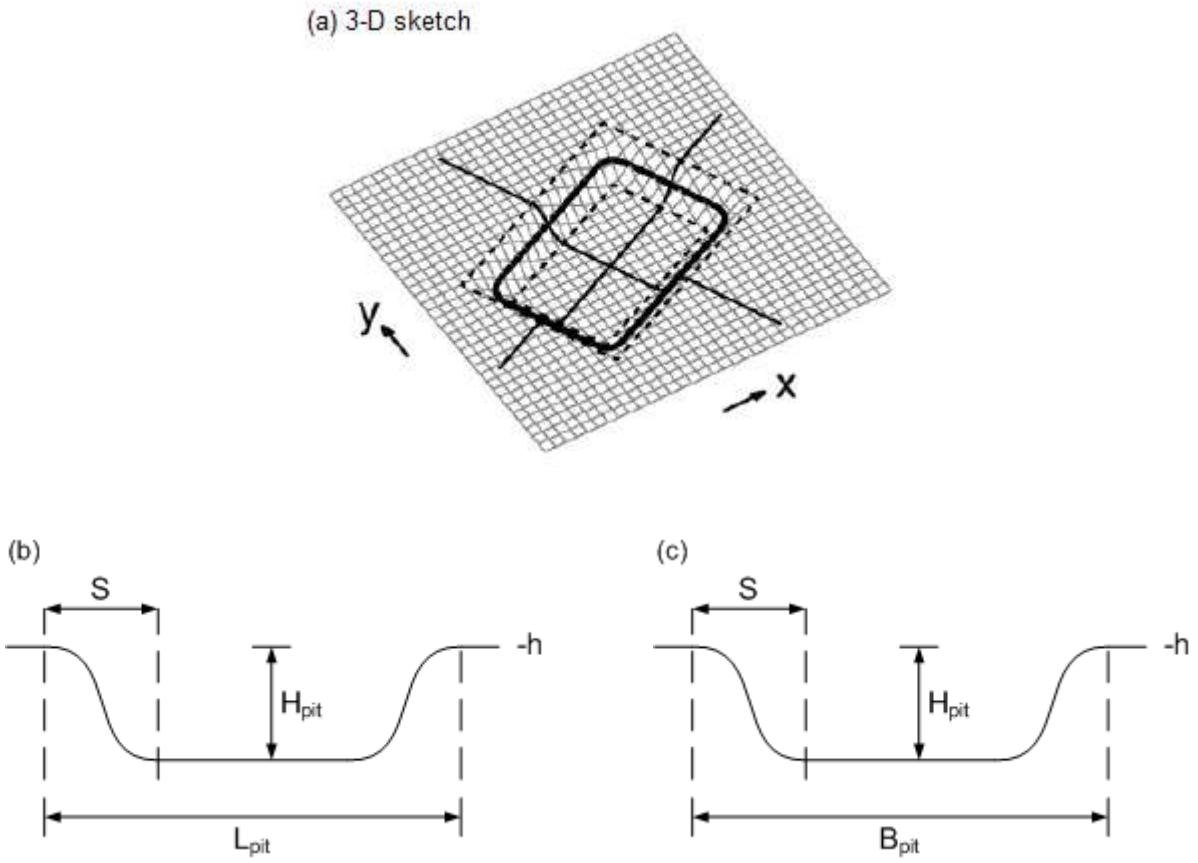

Figure 5.5: Pit geometry: (a) 3-D sketch in raster (Roos et al., 2008), (b) longitudinal pit profile, (c) lateral pit profile. The pit has length L_{pit}, width B_{pit}, depth H_{pit} and a horizontal slope length S. Note: the vertical scale has been strongly exaggerated with respect to the horizontal scale.

At first we implement a shoal at the rear end of the basin in the FEM model. The dimensions of the shoal are set to: 50 km length, 100 km width and 10 m height. The depth of the basin is set to 20 m, which gives a depth of 10 m at the shoal location. A top view of this shoal case is presented in Figure 5.6a. The total slope length lies between the two dotted lines, from s^+ to s^-. The effective shoal length L_{shoal} is thus 50 km. A side view of this representation is presented in Figure 5.7a for the same shoal case. Logically, the same approach applies for the pit case, presented in Figures 5.6b and 5.7b. The simulations with and without smoothed slope length in the FEM model and the 1-DH model simulation of a shoal implementation with similar dimensions at the rear end of the basin will be compared to each other in a single plot. The model simulations have been done with three different bottom friction coefficients for each case. The calibrated values of the coefficients for the closed and semi-enclosed basin have been used for the 1-DH model simulations, presented in Table 5.1 (Section 5.2.2).

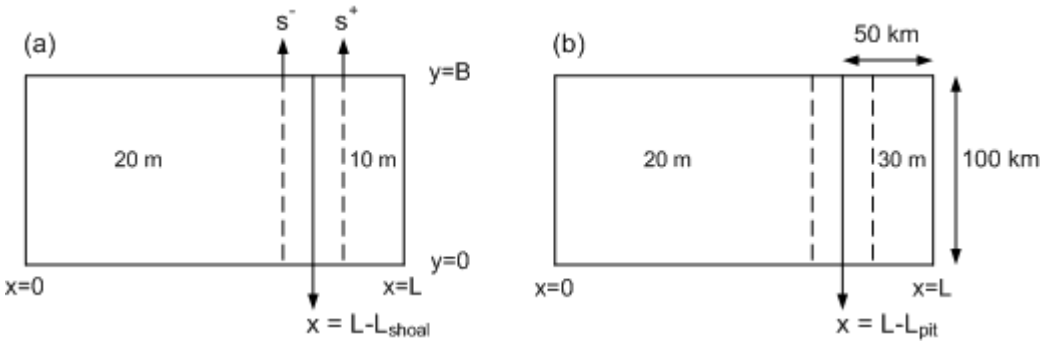

Figure 5.6: Top view of the basin with shoal (a) and a pit (b) implemented over the full width of the basin. The area in between the dotted lines represents the slope length L_{slope}. These *x*-coordinates s^+ and s^- are also shown in the side view of Figure 5.7, where $s^+ = L - L_{shoal} + \frac{1}{4}L_{slope}$ and $s^- = L - L_{shoal} - \frac{1}{2}L_{slope}$ (idem for the *pit* case). Depths in the basin are indicated with 10, 20 and 30 m.

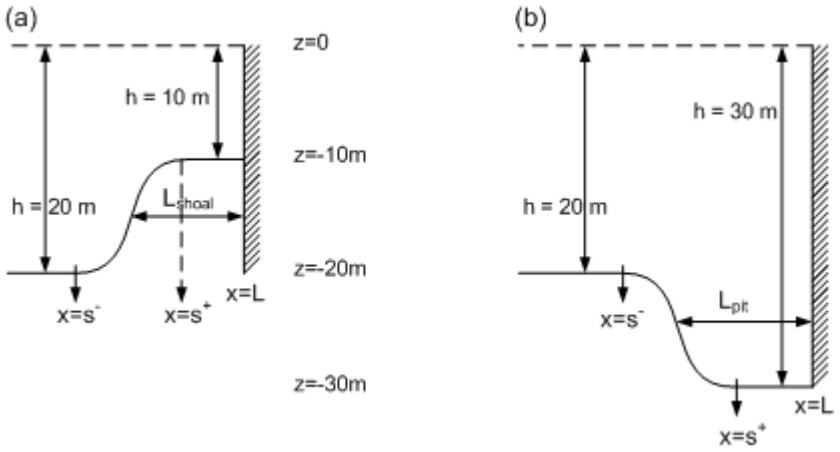

Figure 5.7: Side view of the shoal (a) and pit (b) cases presented in Figure 5.6.

The scaled amplification of the spectral responses of the three model simulations are compared at evaluation points at the rear end of the basin: $x = L$ (1-DH model) and $x = L$, $y = 0$ (FEM model). The results of the closed and semi-enclosed basin simulations with the shoal implementation are presented in Figures 5.8 and 5.9 respectively. Figures 5.8 and 5.9 show that the 1-DH simulations (pink) and the FEM step simulations (dotted black) for both types of basins match quite well for the cases without (a) and weak (b) bottom friction. On the other hand, the moderate bottom friction case (c) of both model simulations for both types of basins matches a lot less. This is consistent with what we already noticed in the previous subsection. Furthermore, the FEM step and FEM slope (cyan) simulations differ much more, especially at higher frequencies. But still they fit reasonably well for the cases weak (b) and moderate (c) bottom friction in both types of basins.

Next, we implement a pit, instead of a shoal, over the full width of the basin in the FEM model. The dimensions of the pit are set to: 50 km length, 100 km width and 10 m height, implemented at the rear end of the basin. The depth of the basin is set to 20 m, which gives a depth of 30 m at the pit location. A top and side view of this pit case is presented in Figures 5.6b and 5.7b, respectively. Again the simulations in FEM will be done with (FEM slope) and without (FEM step) smoothed slope length (i.e. L_{slope} = 10 m) of the pit and compared with a similar 1-DH model simulation of a pit implementation at the rear end of the basin. The simulations have been done with the three different bottom friction coefficients, presented in Table 5.1, for both the closed and the semi-enclosed basin.

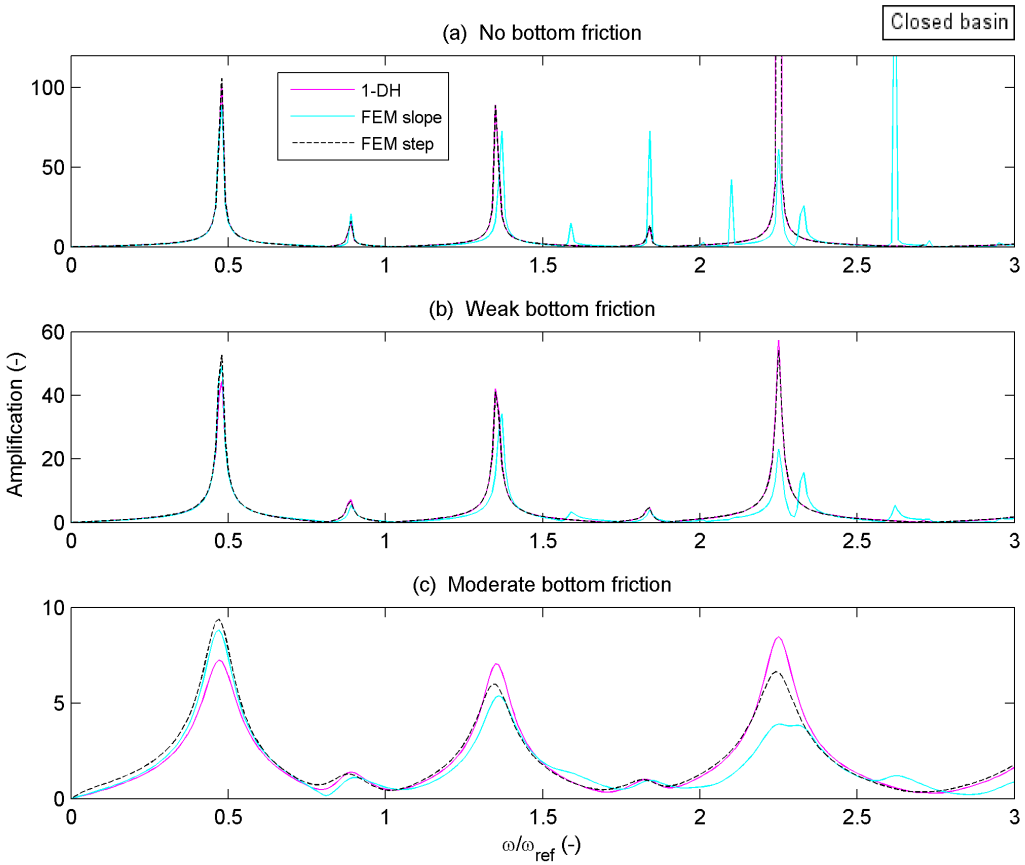

Figure 5.8: Scaled amplification factor *A* as a function of dimensionless frequency ω/ω_{ref} of the **shoal case** implementation at the rear end of the closed basin. 1-DH model results (pink) versus the FEM step (dotted black) and FEM slope (cyan) model results for different bottom friction coefficients (see Table 5.1). Note that all resonant peaks in (a) should reach to infinity, but due to the plotting resolution for ω this is not visible for all peaks.

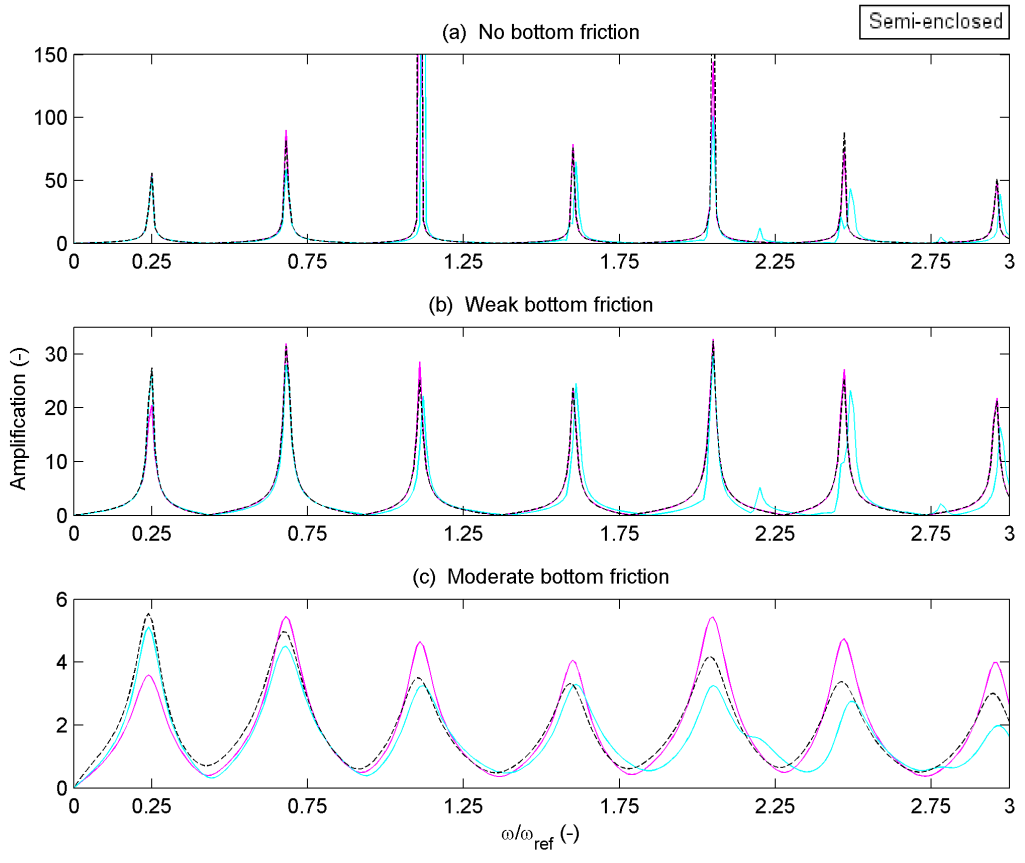

Figure 5.9: Same as Fig. 5.8, but now for the semi-enclosed basin.

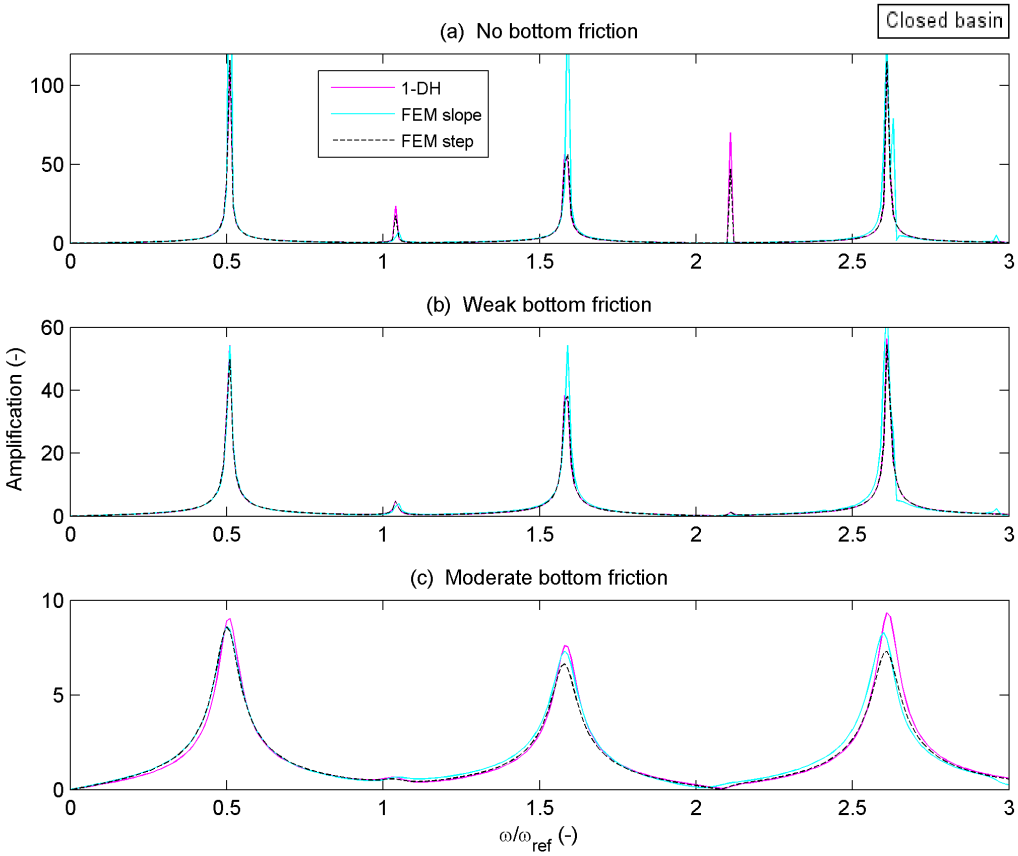

Figure 5.10: Same as Fig. 5.8, but now for the **pit case** implementation at the rear end of the closed basin.

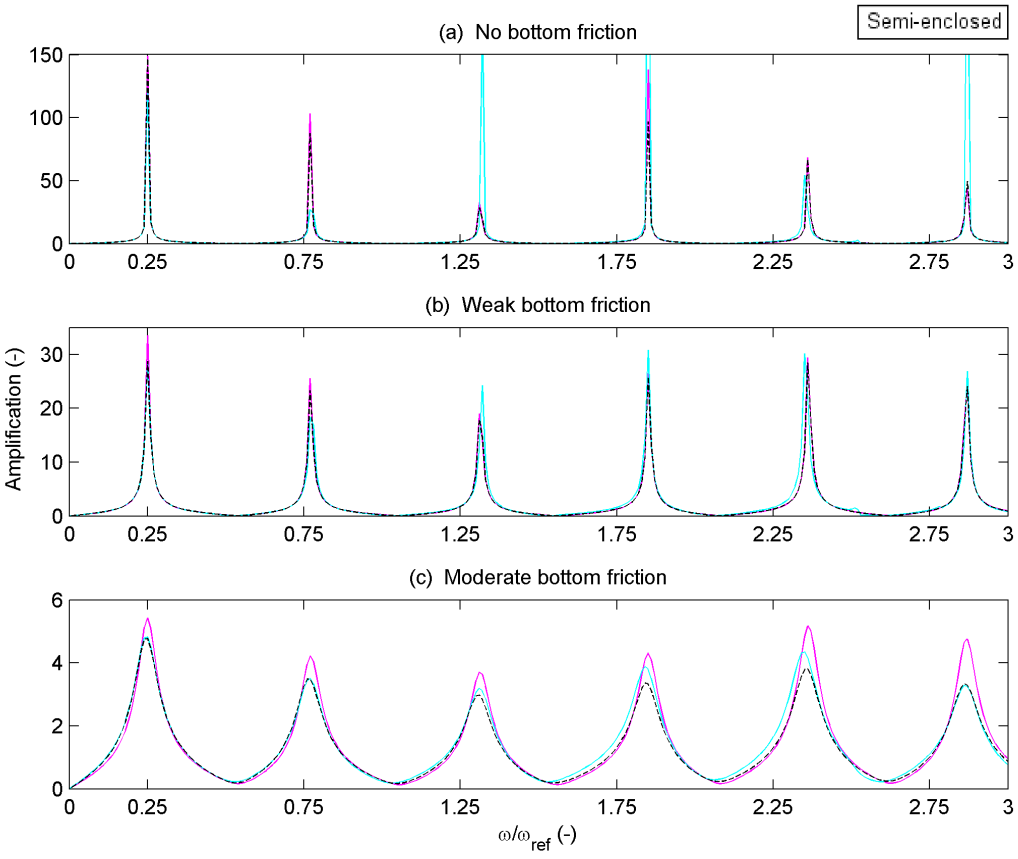

Figure 5.11: Same as Fig. 5.10, but now for the semi-enclosed basin.

The results of the pit implementation over the full width of the basin for both the closed and semi-enclosed basin are presented in Figures 5.10 and 5.11 respectively. These two figures show that the spectral responses of the 1-DH simulations (pink) and the FEM step simulations (dotted black) match quite well for the cases without (a) and weak (b) bottom friction in both types of basins. On the other hand, the spectral responses match a lot less in the moderate bottom friction (c) cases, just like the shoal case simulations. Moreover, the spectral responses of the FEM step and FEM slope (cyan) simulations match fairly well for all three bottom friction coefficients in both types of basins, whereby the differences are mainly in the amplitudes of the resonant peaks. It therefore seems that the FEM slope simulations of the pit case match better with the 1-DH and FEM step simulations than the shoal cases in both types of basins.

5.2.5 Cross-basin wind forcing simulations

The wind forcing in the FEM model can be simulated in arbitrary direction. The wind forcing in the 1-DH model can only be simulated in the along-basin *x*-direction, representing a wind angle of zero degree. However, we can simulate a cross-basin wind forcing, representing a wind angle of 90 degrees, in the 1-DH model by turning the basin 90 degrees. This means that the length of the basin will be replaced by the width of the basin. This is only true for 1-DH model simulations in the flat bed of the closed basin. All previous model simulations have been done with along-basin wind forcing. Here, we will compare the modified cross-basin wind forcing simulation in the 1-DH model with the cross-basin wind forcing simulation in the FEM model. In both model simulations we apply a flat bed topography in the closed basin. The scaled amplification of the spectral responses are compared at evaluation points at the rear end of the basin: $x = L$ (1-DH model) and $x = L$, $y = 0$ (FEM model). The model simulations for three different bottom friction coefficients have been presented in Figure 5.12. Only the moderate bottom friction coefficient *r* have been recalibrated to obtain the best fit with the FEM model simulation. This resulted in a recalibrated *r*-value of 7×10^{-4} with a standard error of 8.5×10^{-3} over the full frequency domain for the 1-DH model. The other two bottom friction coefficients can be found in Table 5.1 (weak and no bottom friction).

Figure 5.12 shows that both model simulations match quite well for all three bottom friction coefficients, especially in the weak bottom friction case (b) where the differences are hardly visible. We further notice that the resonance peaks show up at the scaled resonant frequencies 1 and 3 in the cross-basin wind forcing case. Recall from Chapter 4 that resonance occurs in the closed basin if kL becomes close to odd integers n of π. Considering zero friction, this means that resonance occurs if:

$$\omega = \frac{n\pi\sqrt{gh}}{B} \qquad \text{for } n = 1, 2, \ldots \tag{5.2}$$

The width B (100 km) of the basin equals the effective basin length in the cross-basin wind forcing case. Thus, the resonant frequencies will double when the effective basin length has been halved in this case (and ω_{ref} remains the same), which means that resonance occurs at ω/ω_{ref} = 1, 3, 5, … etc. instead of at ω/ω_{ref} = 0.5, 1.5, 2.5, … etc. This is in accordance with the results shown in Figure 5.12.

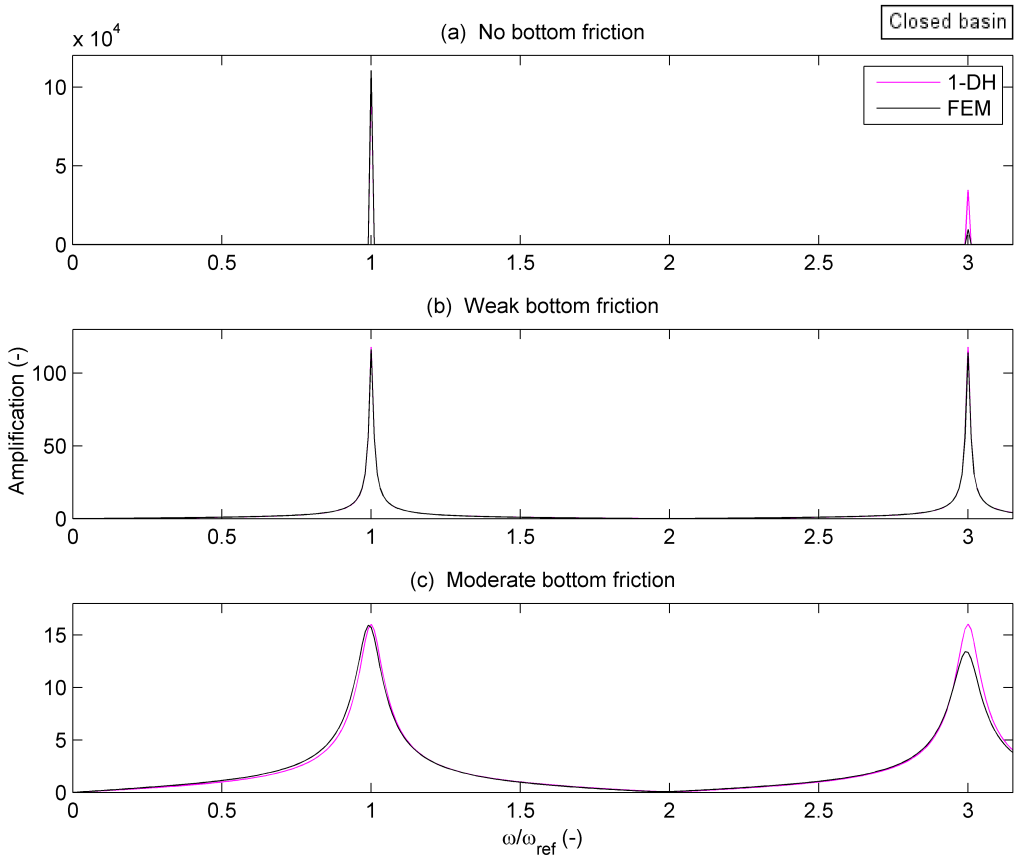

Figure 5.12: Scaled amplification factor *A* as a function of dimensionless frequency ω/ω_{ref} of the **flat bed case** at the rear end of the closed basin for different bottom friction coefficients (a-c). FEM model results (black) versus 1-DH model results (pink), where cross-basin wind forcing is applied.

5.3 Sensitivity analysis regarding the location of topographic elements in the basin

In the FEM model, topographic elements such as shoals and pits can be implemented at various locations in the basin. Here, we have chosen to study two different locations in front of the coastal boundary of the basin. This is because of the expectation of the strongest influence on the basin's spectral response at these locations, compared to locations in the centre and in the front (offshore) of the basin. This is also confirmed by test runs, not presented here. Furthermore, at these locations, shoals and pits of identical dimensions will be implemented in the domains of the closed and semi-enclosed basin in the FEM model. All model simulations in this section will be done with along- and cross-basin wind forcing. The spectral responses of the shoal and pit cases will be analyzed at several evaluation points along the coastal boundary for both wind directions. The shoal cases will be treated first in Section 5.3.1, followed by the pit cases in Section 5.3.2.

5.3.1 Sensitivity of the spectral response to the shoal location in the basin

The fixed dimensions of the shoal have been set effectively to: 50 km length, 50 km width, 10 m height and 8 km slope length. The shoal will be implemented at two different locations in front of the coastal boundary of the basin, presented in Figure 5.13: the upper shoal case (a) and the central

shoal case (b). The shoal locations will be studied separately, meaning that the shoal is implemented at one of the two locations per model simulation.

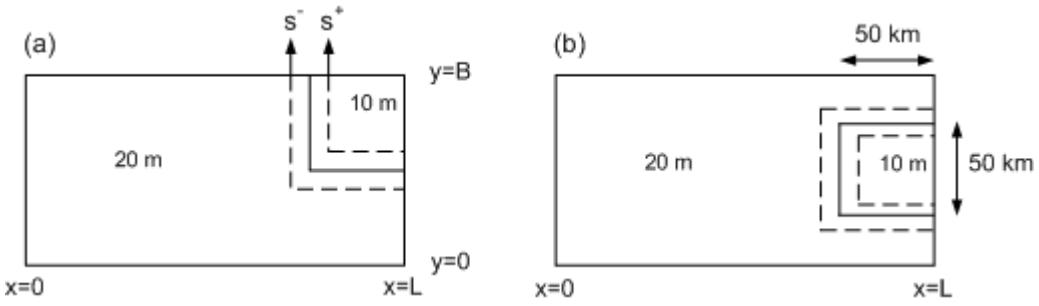

Figure 5.13: Top view of the shoal locations (a & b) in front of the coastal boundary ($x = L$). The same slope length approach as in Figs. 5.6 & 5.7 applies here as well, meaning that the dotted lines indicate the presence of a smooth sloping topography between basin and shoal.

For each shoal case simulation, the spectral response differs per evaluation point along the coastal boundary. In this situation, an element size of 4 km results in 49 evaluation points along the coastal boundary in the FEM model. The spectral response at all these 49 points will be plotted in a color plot to illustrate the difference in spectral response behavior. We noticed already in the 1-DH model simulations that the spectral response behavior in a weak bottom friction case is similar to the spectral response behavior in a moderate bottom friction case. Therefore we have chosen to perform the FEM model simulations with a single bottom friction coefficient that represents a coefficient in between weak and moderate bottom friction: s = 0.0005 m s^{-1}. Due to symmetry, a shoal case in the lower right corner of the basin will give completely opposing results (mirror image) compared to a shoal case in the upper right corner (Fig. 5.13a), regarding the spectral response behavior along the coastal boundary. Therefore this lower shoal case will not be presented here. The results of the shoal cases (Fig. 5.13a & b), forced by along-basin wind, are presented in the color plots of Figures 5.14 and 5.15 for the closed and semi-enclosed basin respectively. The vertical axis of the color plots represents the y-coordinates of the 49 evaluation points along the coastal boundary ($x = L$). The bottom (top) right corner of the basin corresponds to evaluation point y = 0 (y = 100 km).

Figures 5.14 and 5.15 demonstrate that implementation of the shoal cases have resulted in shifts of the resonance peaks to lower frequencies. These peak shifts increase as the frequency increases. This is in line with the 1-DH model results in Chapter 4. Furthermore, the color plots clearly show that the location of the shoal influences the spatial behavior of the spectral response along the coastal boundary. We notice that the peak amplitudes are highest at evaluation points near the shoal location, especially at the higher resonant frequencies. This is also true for the lower right shoal case in both types of basins, not presented here for symmetry arguments.

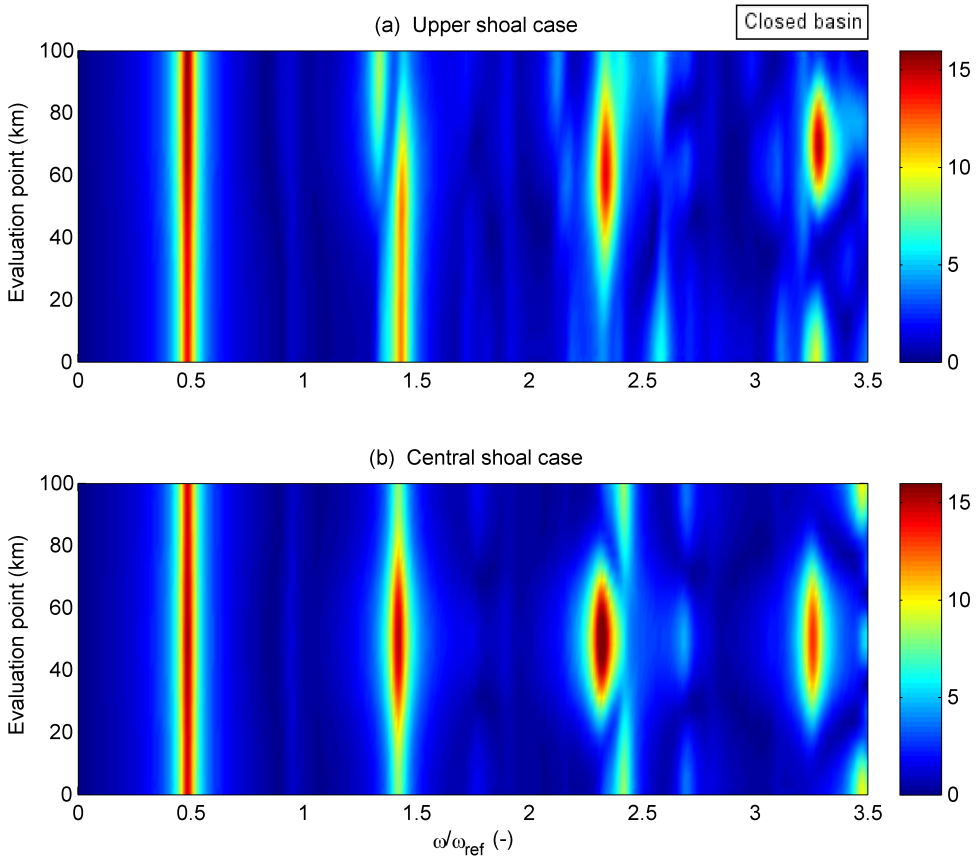

Figure 5.14: Scaled amplification factor A as a function of dimensionless frequency ω/ω_{ref} (horizontal axis) at 49 evaluation points (vertical axis) along the coastal boundary of the closed basin with shoal cases (a) & (b). Along-basin wind forcing is applied and s = 0.0005 m s^{-1}.

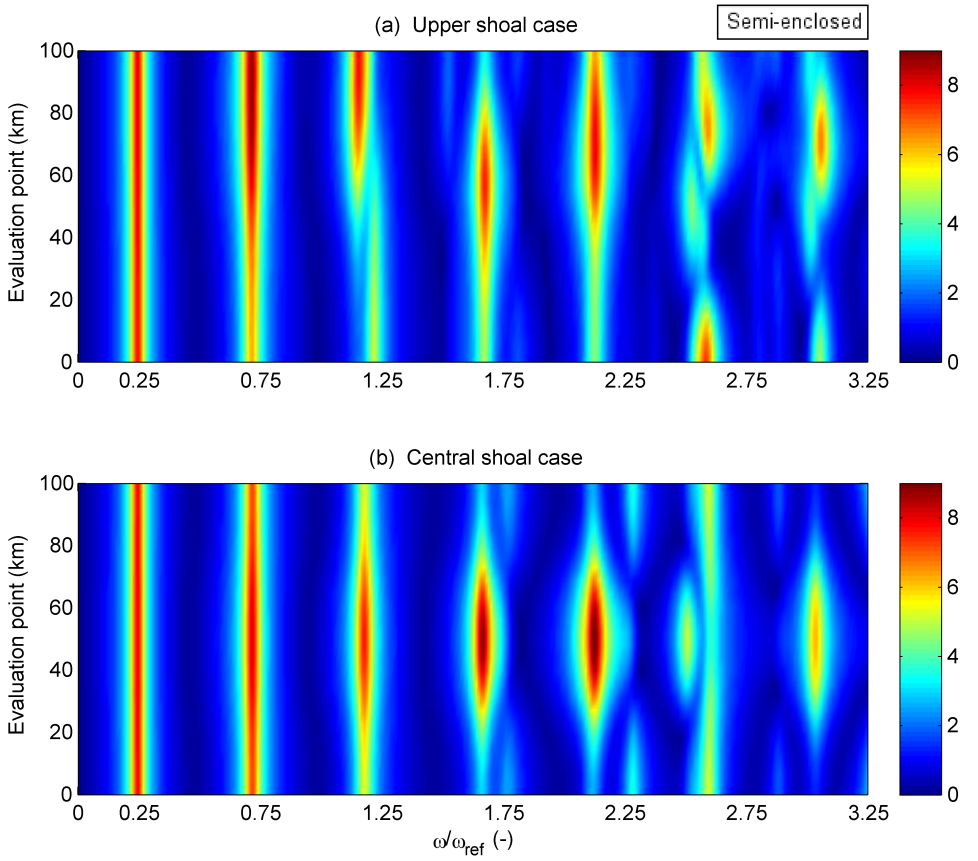

Figure 5.15: Same as Fig. 5.14, but now for the semi-enclosed basin.

Instead of along-basin wind forcing, the same cases have been simulated with cross-basin wind forcing as well. First we will present the results of the flat bed cases, forced by cross-basin wind, for both types of basins in Figure 5.16.

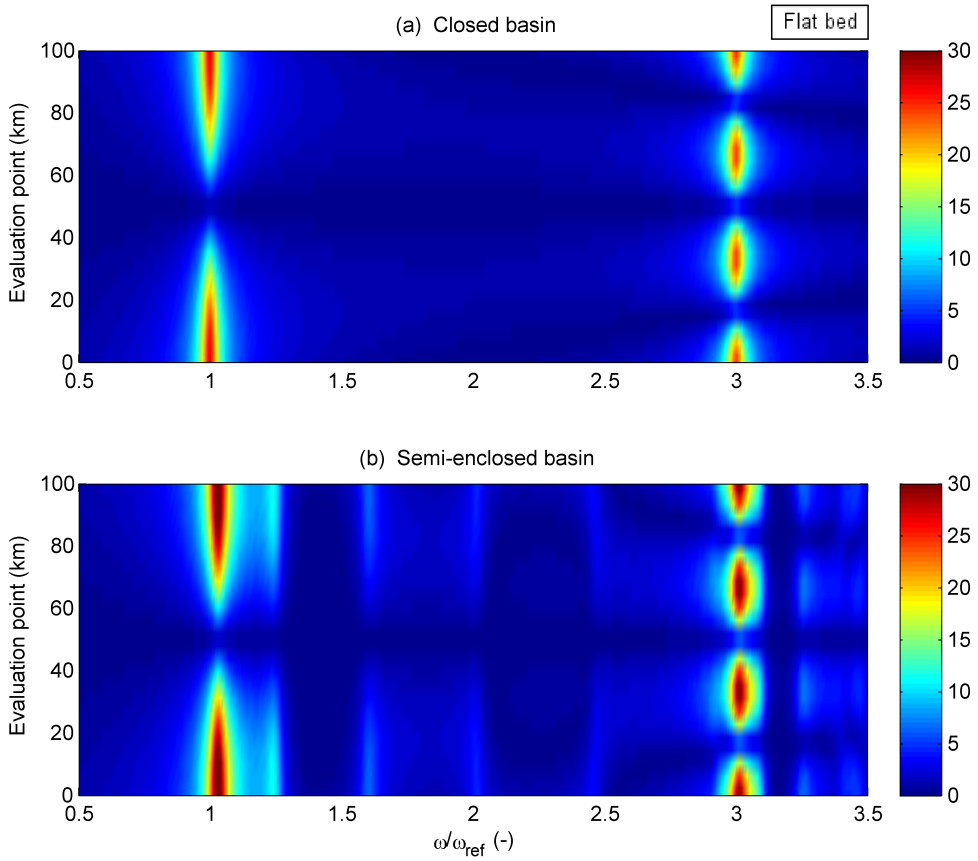

Figure 5.16: Scaled amplification factor *A* as a function of dimensionless frequency ω/ω_{ref} (horizontal axis) at 49 evaluation points (vertical axis) along the coastal boundary of the flat bed case in the closed (a) and semi-enclosed (b) basin. Cross-basin wind forcing is applied and s = 0.0005 m s^{-1}.

We already noticed from Section 5.2.4 that in the flat bed case of the closed basin with cross-basin wind forcing, the classical resonance peaks are obtained at frequencies ω/ω_{ref} = 1 and 3. Figure 5.16b shows that these resonance peaks are also obtained in the flat bed case of the semi-enclosed basin at approximately the same frequencies (slightly higher values). Figure 5.16 further shows that the spatial behavior of the spectral response varies along the coastal boundary, in contrast to the flat bed cases forced by along-basin wind. The spatial behavior even differs per resonant peak. Moreover, we notice that a few new and smaller peaks emerge at other frequencies than the classical resonant frequencies in the semi-enclosed basin (Fig. 5.16b). Nevertheless we can conclude that the amplification at the center of the coastal boundary (y = 50 km) almost completely damps out for all simulated frequencies in both types of basins.

Next, the results of the shoal cases forced by cross-basin wind are presented in Figures 5.17 and 5.18 for the closed and semi-enclosed basin. At first we notice that in these shoal cases the resonance peaks are shifted to lower frequencies, with larger shifts at higher frequencies. Secondly,

we notice that new peaks emerge right behind the classical resonance peaks in the results of both shoal cases, which were not (slightly) present in the results of the flat bed case of the closed (semi-enclosed) basin. Thirdly, when we compare the results of the shoal cases with the results of the flat bed cases (see Fig. 5.16), we notice that the amplitudes of the shoal cases are lower than the amplitudes of the flat bed cases, especially at higher frequencies. In addition to that, we notice some deflections of the peaks in the spectral response behavior of the upper shoal cases in terms of amplitudes and shifts with respect to evaluation points near the shoal location. Moreover, the peaks in the center shoal cases show a more symmetrical behavior along the coastal boundary, because of its central location of the shoal. Concluding, the results show that the location of the shoal certainly influences the behavior of the spectral response along the coastal boundary. As already mentioned, due to symmetry the lower shoal cases show identical spectral response behavior as the upper shoal cases, only in opposite direction (mirror image).

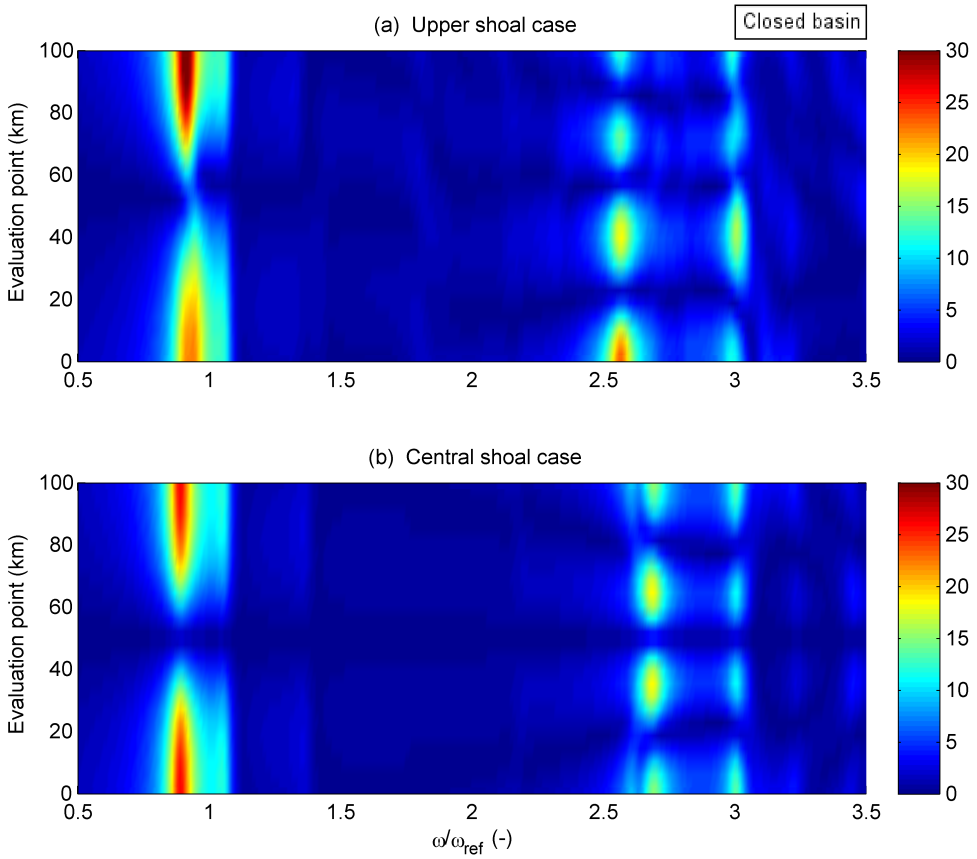

Figure 5.17: Scaled amplification factor A as a function of dimensionless frequency ω/ω_{ref} (horizontal axis) at 49 evaluation points (vertical axis) along the coastal boundary of the closed basin with shoal cases (a) & (b). Cross-basin wind forcing is applied and s = 0.0005 m s^{-1}.

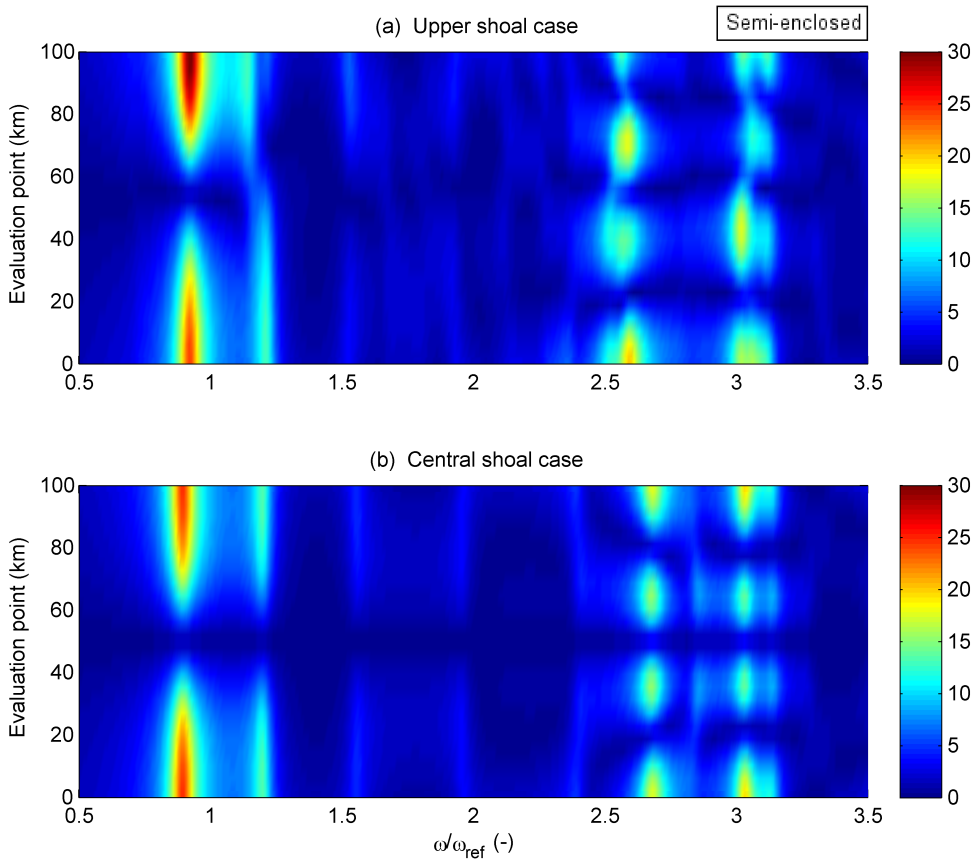

Figure 5.18: Same as Fig. 5.17, but now for the semi-enclosed basin.

5.3.2 Sensitivity of the spectral response to the pit location in the basin

Instead of implementing a shoal at two different locations in the basin, we will now implement a pit at the same locations in front of the coastal boundary of the basin domain in the FEM model. The fixed dimensions of the pit are the same as the shoal: 58 km length, 58 km width, 10 m depth and a smoothed slope length of 8 km. The pit locations will be studied separately and are presented in Figure 5.19: the upper pit case (a) and the central pit case (b).

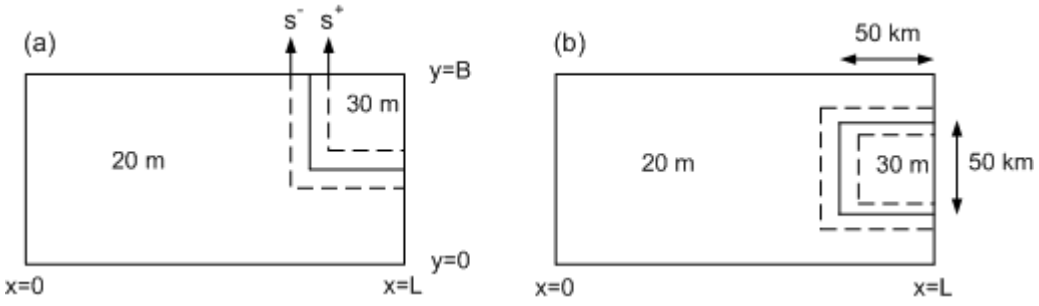

Figure 5.19: Top view of the pit locations (a & b) in front of the coastal boundary ($x = L$). 20 m depth of the basin with a smooth transition (from s^- to s^+) to 30 m depth at the pit location.

The FEM model simulations have been performed with bottom friction coefficient s = 0.0005 m s^{-1}. First we will present the results of the pit cases forced by along-basin wind for the closed and semi-enclosed basin in Figures 5.20 and 5.21.

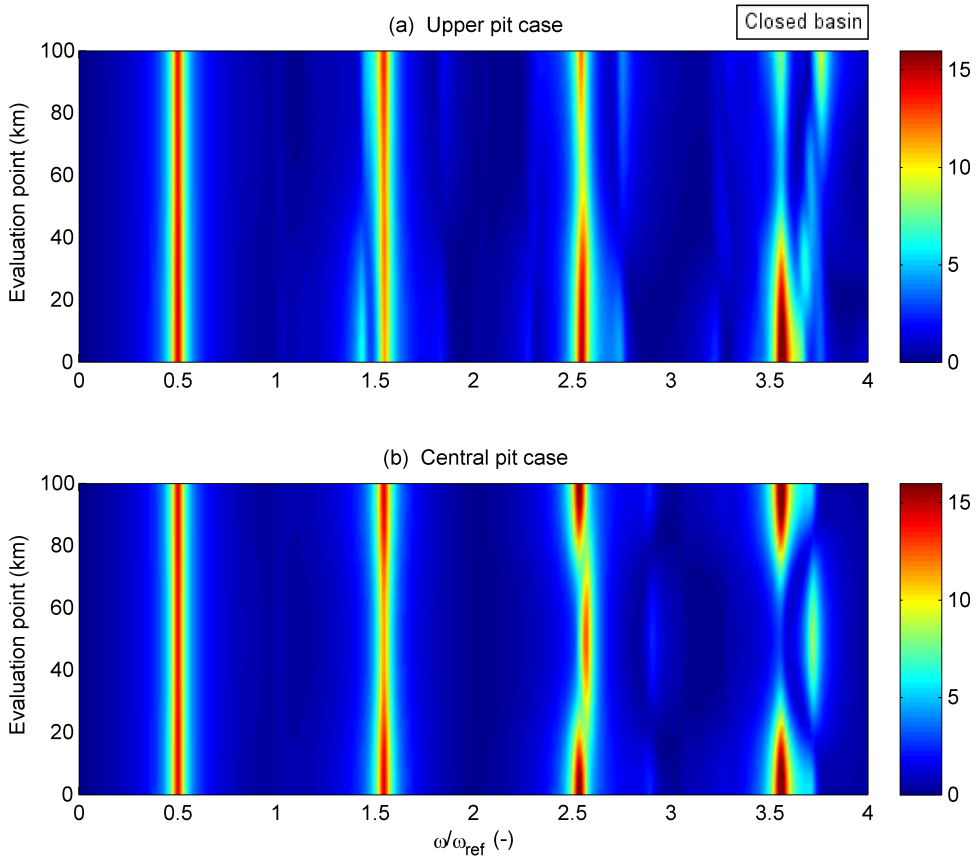

Figure 5.20: Scaled amplification factor *A* as a function of dimensionless frequency ω/ω_{ref} (horizontal axis) at 49 evaluation points (vertical axis) along the coastal boundary of the closed basin with pit cases (a) & (b). Along-basin wind forcing is applied and $s = 0.0005$ m s^{-1}.

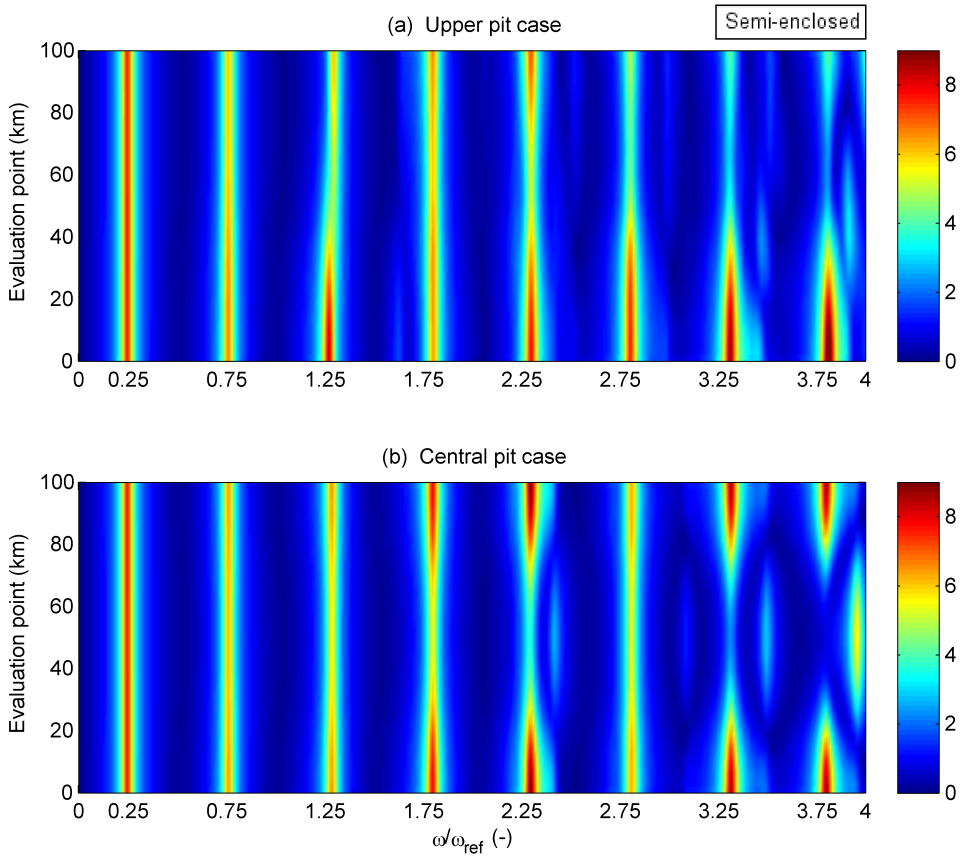

Figure 5.21: Same as Fig. 5.20, but now for the semi-enclosed basin.

We first notice from Figures 5.20 and 5.21 that implementation of the pit cases have resulted in slight shifts of the resonance peaks to higher frequencies. These peak shifts increase as the frequency increases. We further notice, especially at higher resonant frequencies, that peak amplitudes are lowest at evaluation points near the pit location, in contrast to the shoal cases where peak amplitudes are highest at evaluation points near the shoal location. This is also true for the lower right pit case in both types of basins, not presented here for symmetry arguments.

Next, the same pit cases forced by cross-basin wind instead of along-basin wind have been simulated. The results of these cases in the closed and semi-enclosed basin are presented in Figures 5.22 and 5.23. When we compare the results of the pit cases (Fig. 5.22) with the flat bed case (Fig. 5.16a) in the closed basin, we first notice that the peak amplitudes of the pit cases are substantially lower than the peak amplitudes of the flat bed case. This applies to a lesser extent for the cases in the semi-enclosed basin. Secondly, we notice in the pit cases that peaks are shifted to higher frequencies with larger shifts for higher frequencies. Also, new peaks emerge around the classical resonance peaks, especially in the closed basin. Thirdly, when we look at the pit cases in the closed basin we notice a tendency of lower amplitudes at evaluation points near the pit location, especially at higher frequencies. However, this tendency is not observed in the pit cases of the semi-enclosed basin.

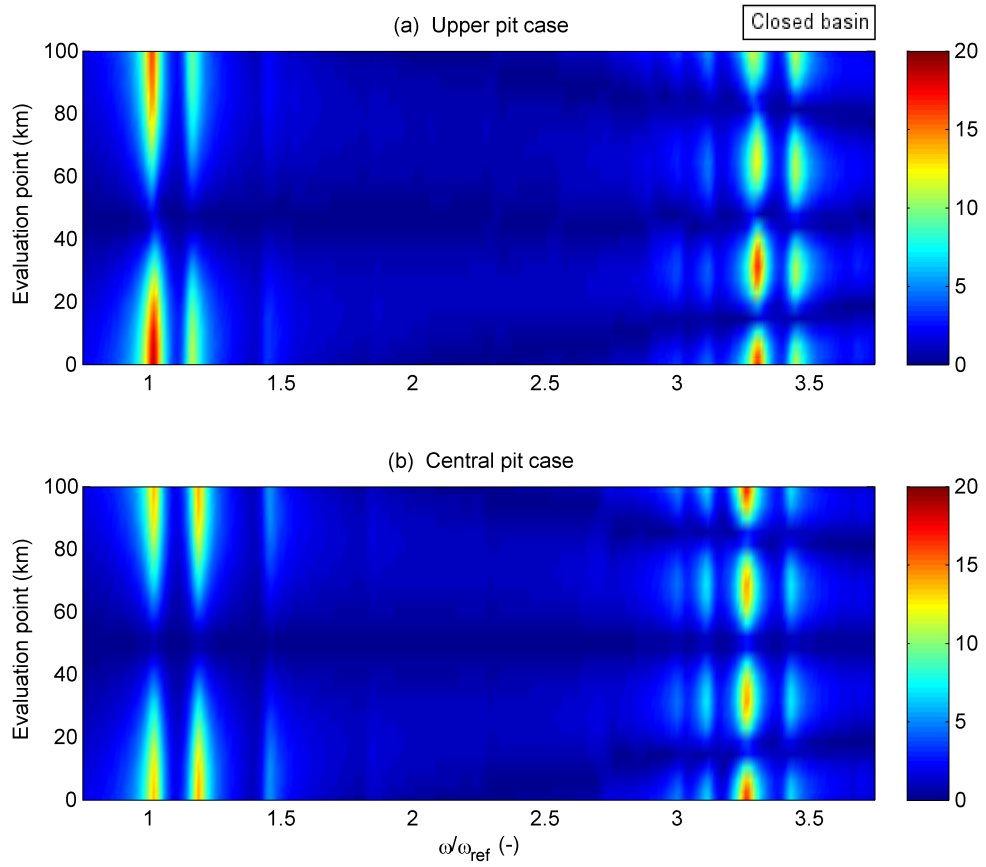

Figure 5.22: Same as Fig. 5.20, but now with cross-basin wind forcing.

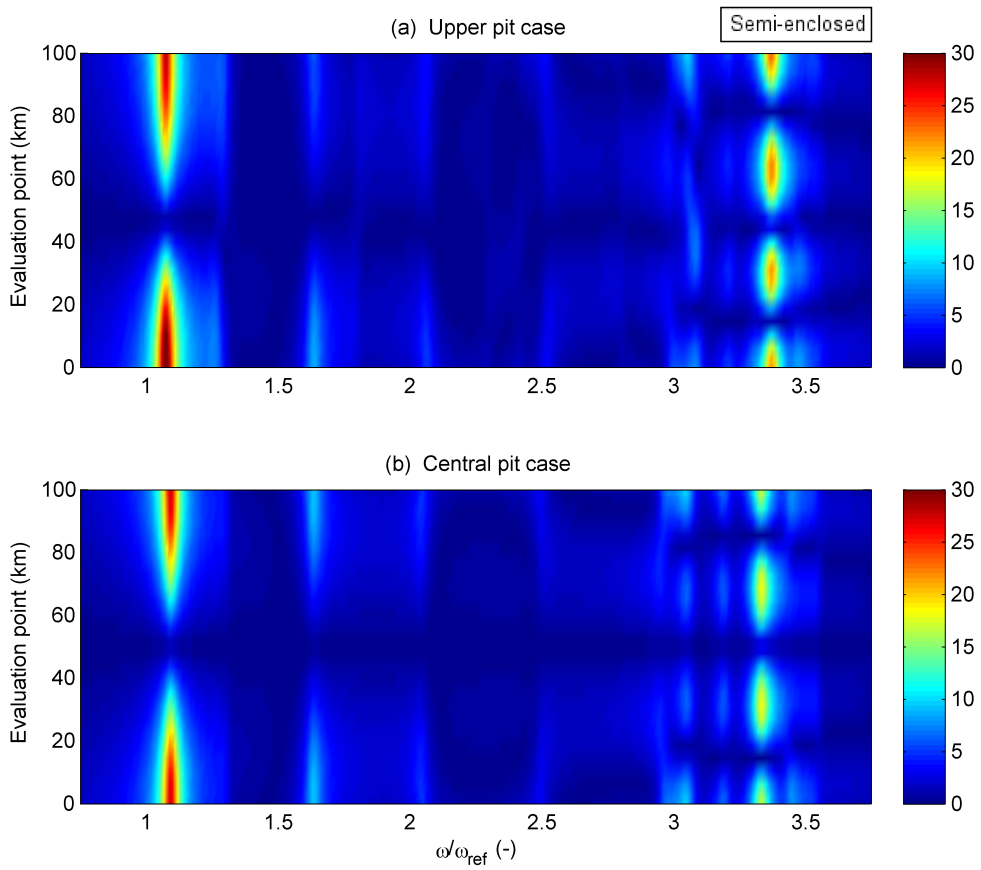

Figure 5.23: Same as Fig. 5.23, but now for the semi-enclosed basin.

5.4 Sensitivity analysis regarding the wind direction relative to topographic elements in the basin

In this section we will continue with analyzing the influence of the wind direction on the spectral response in earlier studied cases, such as the flat bed, shoal and pit cases. In this analysis extra attention is on the location of the elements relative to specific evaluation points along the coastal boundary. Furthermore, the focus in Section 5.3 was on along- and cross-basin wind forcing. Since we want to vary the wind direction, we will focus on 30° and 60° wind angle forcing in this section. We start by showing the influence of various wind angles on the spectral response of the flat bed cases at a specific evaluation point in Section 5.4.1. In turn, we will show the influence of shoal and pit locations with regard to the 30° and 60° wind angle forcing on the spectral response, treated in Sections 5.4.2 and 5.4.3.

5.4.1 Sensitivity of the spectral response to wind angles in the flat bed case

Due to symmetry, the spectral response driven by the wind with a certain angle is identical to the spectral response driven by the wind in opposite direction (certain angle + 180°). For example, this means that a wind angle of 90° results in the same spectral response as a wind angle of 270°. Furthermore, it appears that for wind angles between zero and 90° the spectral response at

evaluation point y = 25 km of a certain angle is identical to the spectral response at evaluation point y = 75 km of that same angle added with 90° (certain angle + 90°). This means that, for example, the spectral response at evaluation point y = 25 km driven by a wind angle of 45° is identical to the spectral response at evaluation point y = 75 km driven by a wind angle of 135°. This is true for the flat bed case in both types of basins. In this analysis, we will focus on the effects of wind angles between zero (along-basin wind) and 90° (cross-basin wind). In the previous section we already performed model simulations with wind angles of zero and 90°. Because of the linearity of the model, we can calculate the complex spectral response solution N_θ for every angle θ from the complex spectral response solutions of the zero and 90° wind angle cases, using the following expression:

$$N_\theta = N_{\text{along}} \cos\theta + N_{\text{cross}} \sin\theta. \tag{5.3}$$

Where N_{along} is the complex along-basin wind solution (0°) and N_{cross} is the complex cross-basin wind solution (90°). Subsequently, color plots will be used to illustrate the spectral response behavior at a specific evaluation point for various wind angles (vertical axis) ranging between zero and 90°, over a frequency range of 400 modes (horizontal axis). Just as in Section 5.3, bottom friction coefficient s = 0.0005 m s^{-1} is applied in all the cases in Section 5.4. The results of the flat bed cases for various wind angles at evaluation point y = 25 km are presented in the color plots of Figure 5.24. These color plots clearly show the great influence of wind direction on the spectral response behavior.

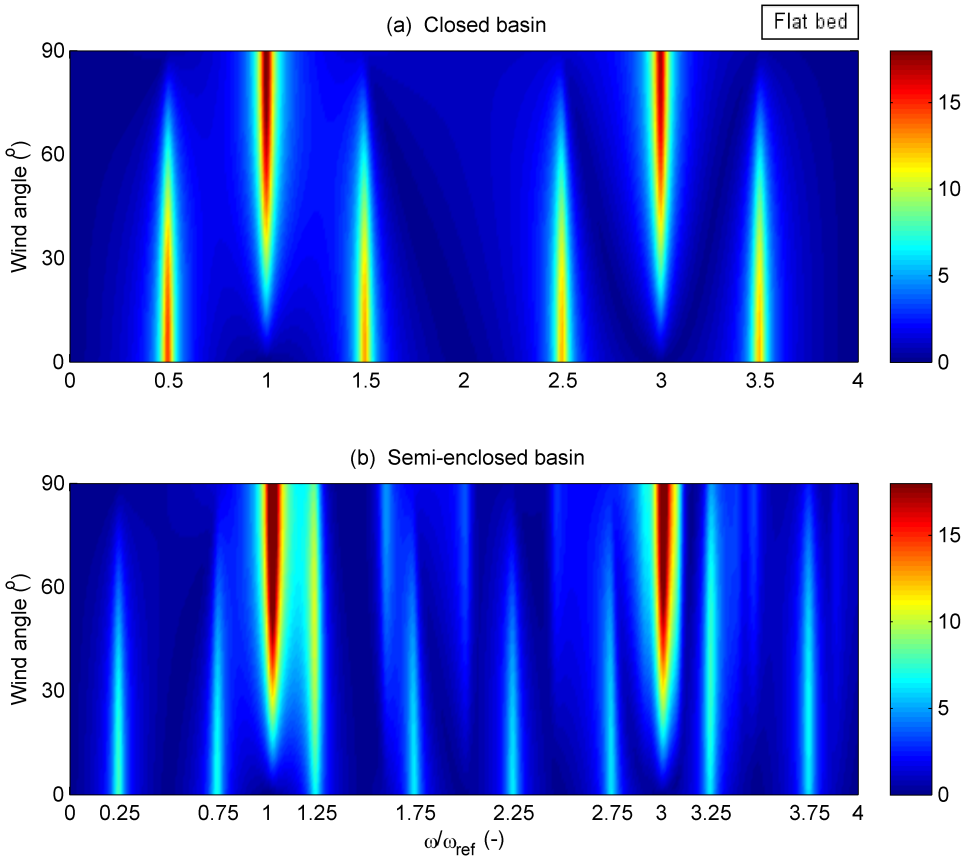

Figure 5.24: Scaled amplification factor A as a function of dimensionless frequency $\omega/\omega_{\text{ref}}$ (horizontal axis) and wind angle (vertical axis), at evaluation point y = 25 km: flat bed case in the closed (a) and semi-enclosed (b) basin with s = 0.0005 m s^{-1}.

In Section 5.3 we have already seen that the spectral response of a uniform wind in along-basin direction is very different than the same wind in cross-basin direction. The spectral response of wind angles in between zero and 90°, consists of a combination of the spectral responses for these two wind angles, clearly illustrated in Figure 5.24. Naturally, along-basin wind forcing has a high (low) contribution in the spectral response of a low-angle (high-angle) wind forcing case and vice versa for cross-basin wind forcing. We further notice that the spectral response in the closed basin (Fig. 5.24a) has a clear symmetrical behavior. This appears to be less pronounced in the semi-enclosed basin. That is because of the total reflection of the propagating waves at the boundaries of the closed basin, in contrast to the open boundary system in the semi-enclosed basin.

5.4.2 Sensitivity of the spectral response to wind angles in the shoal cases

The next step will be to compare the spectral response of two different shoal cases with the spectral response of the flat bed case at specific evaluation points, where we imposed wind forcing with 30° and 60° wind angles. Section 5.3.1 already treated the shoal cases forced by along- and cross-basin wind. The spectral response behavior will be analyzed at three evaluation points along the coastal boundary. The locations of the shoal cases together with the selected evaluation points are shown in Figure 5.25.

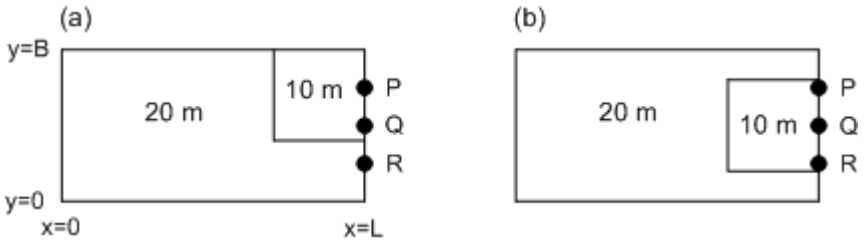

Figure 5.25: Top view of the upper (a) and central (b) shoal location in front of the coastal boundary (*x* = *L*). Slope length of the shoals not included in the sketches**.** Evaluation points P, Q and R at respectively *y* = 75, 50 & 25 km.

We start our analysis by imposing a 30° wind angle forcing on the flat bed case and shoal cases in the closed basin. The resulting spectral response of the flat bed case (dotted black) and the shoal cases (blue and pink) are plotted in one figure for a single evaluation point. Figure 5.26 (a, b & c) shows the results at the three evaluation points P, Q and R respectively. First of all, the flat bed case results reflect the classical resonance peaks for along-basin wind at point Q and reflect a combination of the classical resonance peaks for along- and cross-basin wind at points P and R. Second, the results of both shoal cases show shifts of the resonance peaks to lower frequencies, as expected. Third, in all cases the resonance peaks are dominated by the along-basin wind contribution at point Q. We have seen already in the previous section (see Figs. 5.16-5.18) that the cross-basin wind contribution is close to zero in the center of the coastal boundary. In the results of the upper shoal case (blue) we notice that the peak amplitudes are higher at point P (near the shoal location) than at point R (away from the shoal location). This tendency of higher amplitudes at the evaluation point near the shoal location is also reflected in the results of the central shoal case (pink), but only if we compare the resonance peaks dominated by the along-basin wind: the peak amplitudes are higher at point Q (near the shoal location) than the along-basin peak amplitudes at points P and R (further away from the shoal location).

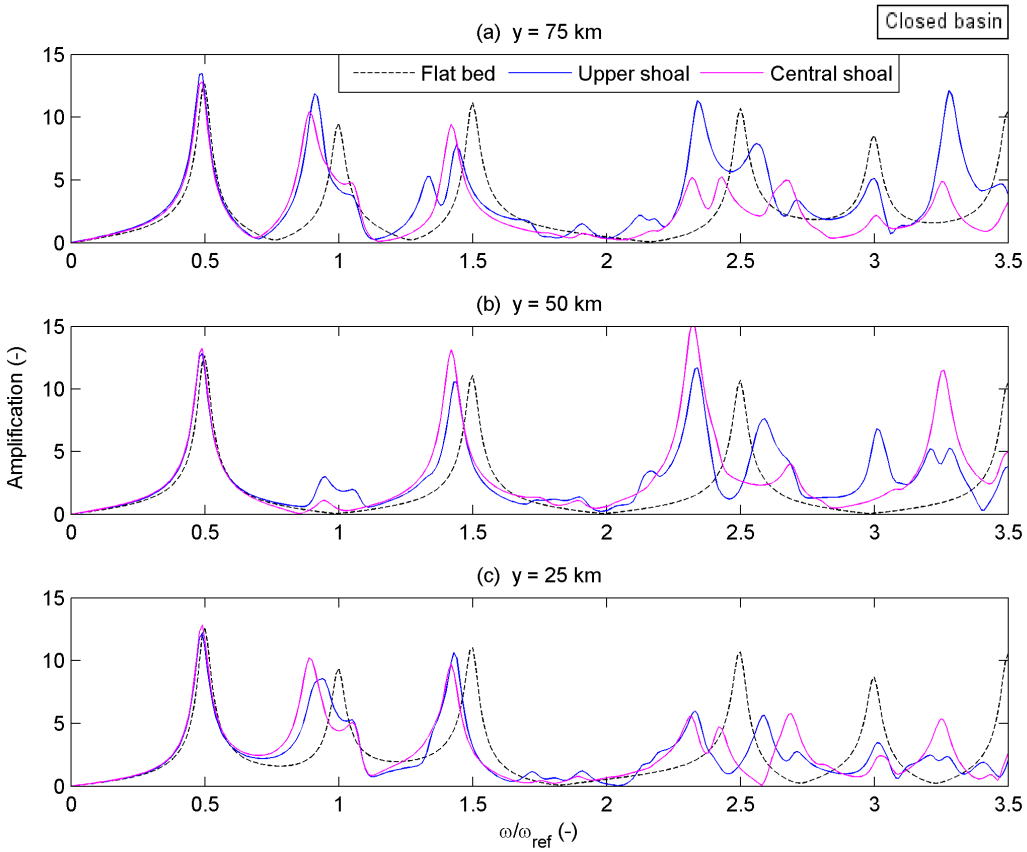

Figure 5.26: Scaled amplification factor A as a function of dimensionless frequency ω/ω_{ref} for a flat bed case (dotted black line), upper shoal case (blue line) and central shoal case (pink line), at evaluation points P (a), Q (b) and R (c) in the closed basin. **30° wind angle forcing** is applied and s = 0.0005 m s^{-1}.

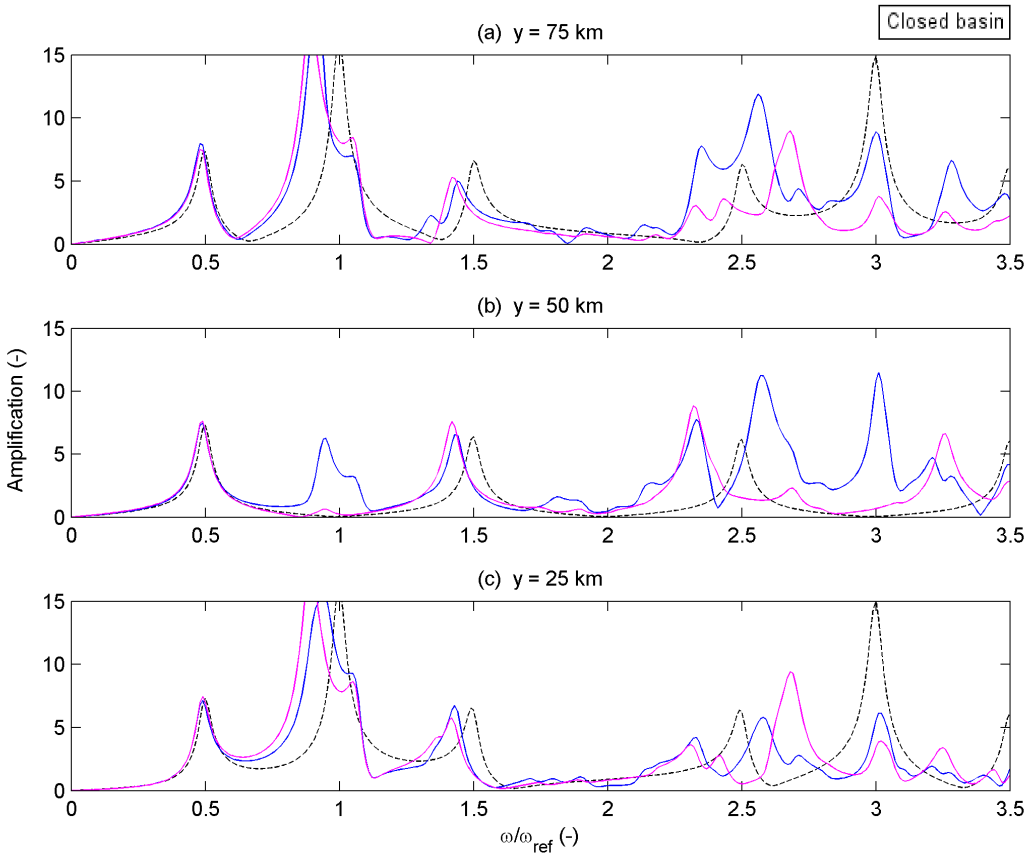

Figure 5.27: Same as Fig. 5.26, but now with **60° wind angle forcing**.

The results of the same cases imposed by a 60°, instead of a 30°, wind angle forcing are presented in Figure 5.27 (a, b & c) for evaluation points P, Q and R respectively. We first notice from the plots at points P and R that the amplitudes of the peaks at frequencies 1 and 3 have increased compared to the 30° wind angle cases (Fig. 5.26). That is because the 60° wind angle forcing is closer to cross-basin (90°) wind forcing, whereby the cross-basin resonance peaks dominate in the 60° wind angle cases. This also explains why the along-basin peaks of the 60° wind angle cases are decreased at all evaluation points compared to the 30° wind angle cases. Furthermore, the results of the upper shoal case show yet again that the highest peak amplitudes are found at point P near the shoal location. The same applies to the results of the central shoal case, where the highest along-basin peak amplitudes are found at point Q near the shoal location.

Next, we will continue with the analysis of the same cases in the semi-enclosed basin. The results of the cases at evaluation points P, Q and R, imposed by a 30° wind angle forcing, are presented in Figure 5.28. The flat bed case results (dotted black) show that the classical resonance peaks for along- and cross-basin wind show up at points P and R. The only notable difference in spectral response behavior of the flat bed case between points P and R is present at frequencies 1.25 and 3.25, where the peak amplitudes are much higher at point R. Apparently, these differences are caused by the lack of symmetry in the semi-enclosed basin, because they are not present in the closed basin results (Fig. 5.26). When we compare the results of the upper shoal case (blue) at points P and R, we further notice higher peak amplitudes (except for the peak at frequency 1.25) at point P near the shoal location, than at point R. This tendency also applies to the central shoal case (pink), with higher peak amplitudes at point Q near the shoal location, compared to the lower along-basin peak amplitudes at points P and R. Thereby, we notice the absence of cross-basin resonance peaks in all three cases at point Q.

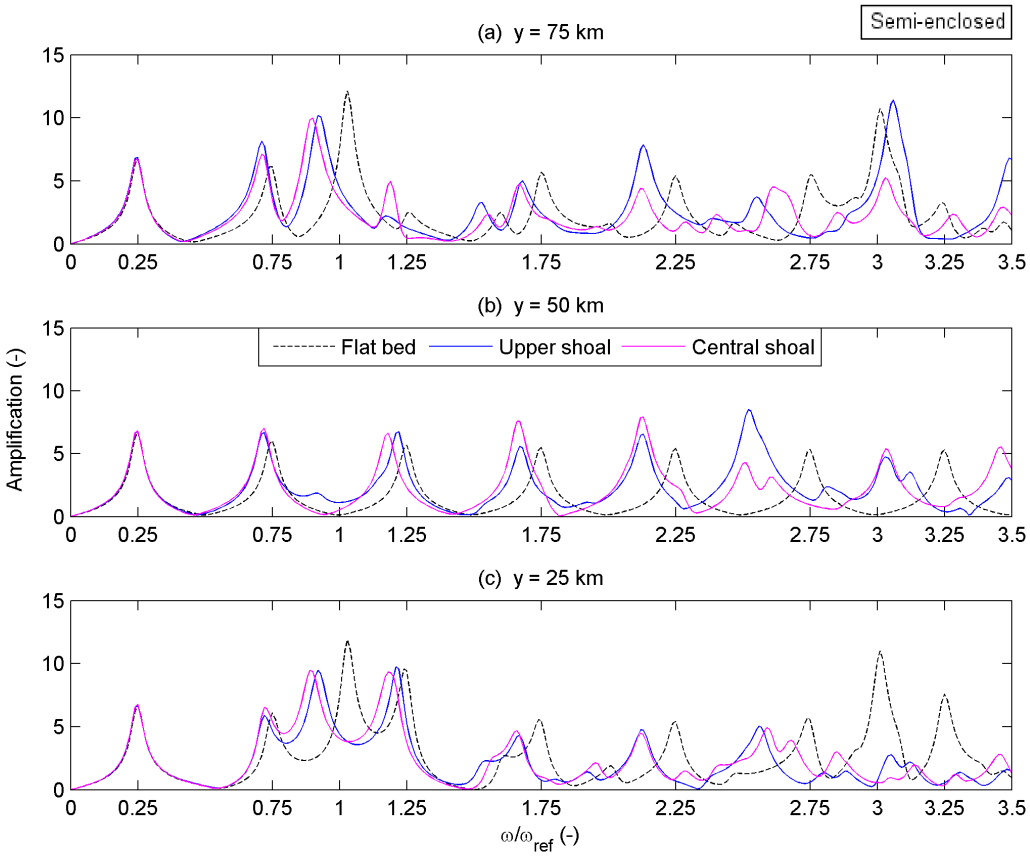

Figure 5.28: Same as Fig. 5.26, but now for the semi-enclosed basin: **30° wind angle forcing** is applied.

The results of the same cases at evaluation points P, Q and R, imposed by a 60° wind angle forcing, are presented in Figure 5.29. Again we notice that the cross-basin peak amplitudes at frequencies 1 and 3 have increased at points P and R, compared to the 30° wind angle cases (Fig. 5.28). And that the along-basin peaks, except for the peak at frequency 1.25, of the 60° wind angle cases are decreased at all evaluation points, relative to the 30° wind angle cases. Figures 5.29a & c further show that the peak amplitudes of the upper shoal case are higher at point P near the shoal than at point R, except for the peak at frequency 1.25.

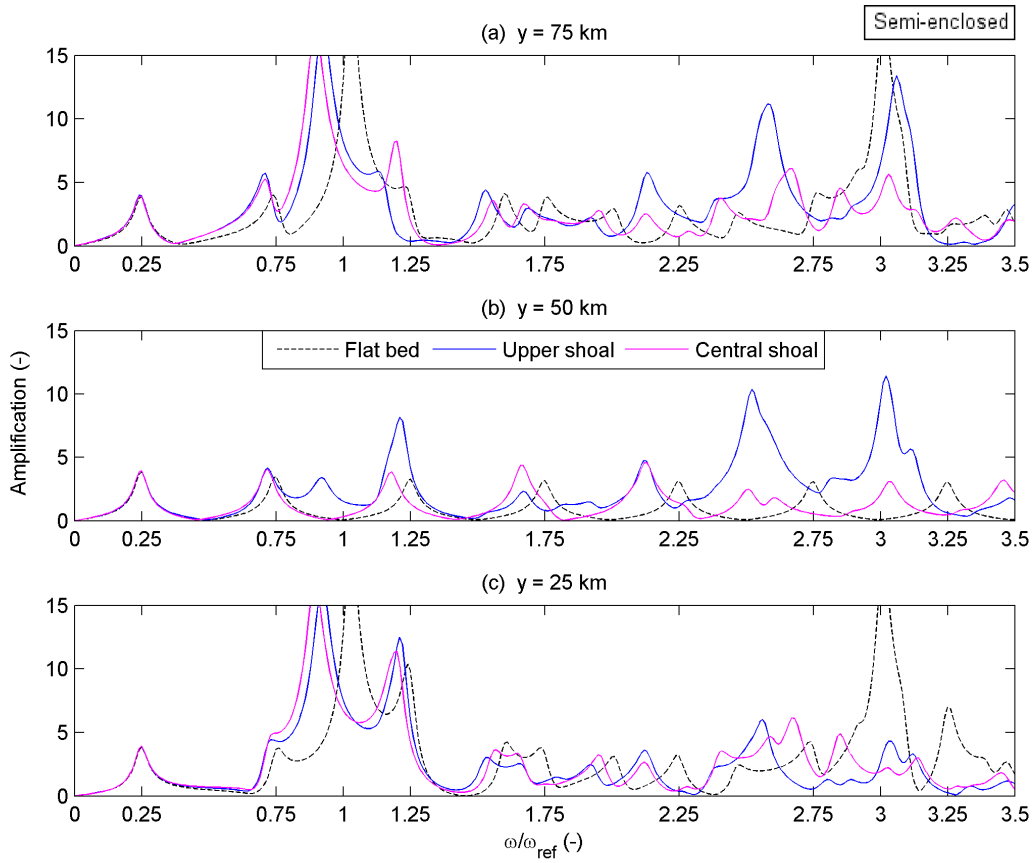

Figure 5.29: Same as Fig. 5.28, but now with **60° wind angle forcing**.

5.4.3 Sensitivity of the spectral response to wind angles in the pit cases

In this section we will do the same analysis with the pit cases instead of the shoal cases. The locations of the pit cases together with the evaluation points of interest are shown in Figure 5.30.

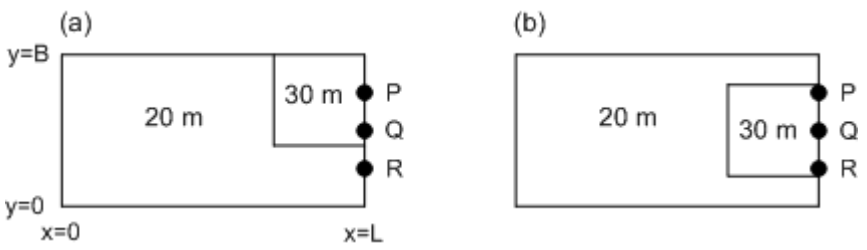

Figure 5.30: Top view of the upper (a) and central (b) pit location in front of the coastal boundary (x = L). Slope length of the shoals not included in the sketches. Evaluation points P, Q and R at respectively y = 75, 50 & 25 km.

First we will impose a 30° wind angle forcing on the pit cases in the closed basin. The resulting spectral responses will be compared with the spectral response of the flat bed case with a 30° wind angle forcing at evaluation points P, Q and R. The results are presented in Figure 5.31. The figure shows that the resonance peaks of the pit cases (blue and pink) are shifted to higher frequencies, compared to the resonance peaks of the flat bed case (dotted black). We further notice an opposite effect in the upper pit case (blue), relative to the upper shoal case in the previous section: peaks are lower (instead of higher in the shoal case) at point P (near the pit location) than the peaks at point R (away from the pit location). However, this tendency does not show up in the central pit case (pink). Furthermore, Fig. 5.31b shows that cross-basin resonance peaks are barely present at point Q, even in the upper pit case.

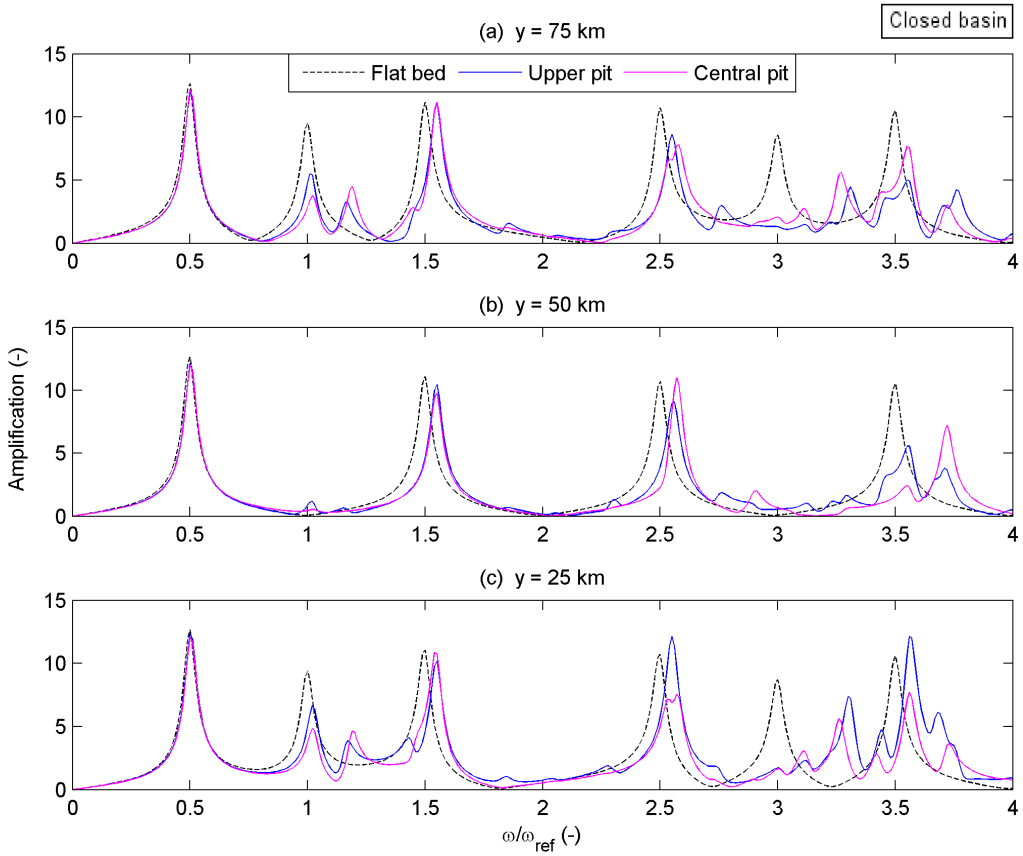

Figure 5.31: Scaled amplification factor *A* as a function of dimensionless frequency ω/ω_{ref} for a flat bed case (dotted black line), upper pit case (blue line) and central pit case (pink line), at evaluation points P (a), Q (b) and R (c) in the closed basin. **30° wind angle forcing** is applied with s = 0.0005 m s^{-1}.

The results of the same cases imposed by a 60° wind angle forcing are presented in Figure 5.32. When we look at the results of the upper pit case, we see once more that the differences in peak amplitudes between point P and R are present. In addition, the cross-basin resonance peaks of all cases dominate at points P and R, whereas the along-basin resonance peaks dominate at point Q. These along-basin peaks at point Q have decreased significantly in the 60° wind angle situation, compared to the 30° wind angle situation (Fig. 5.31b).

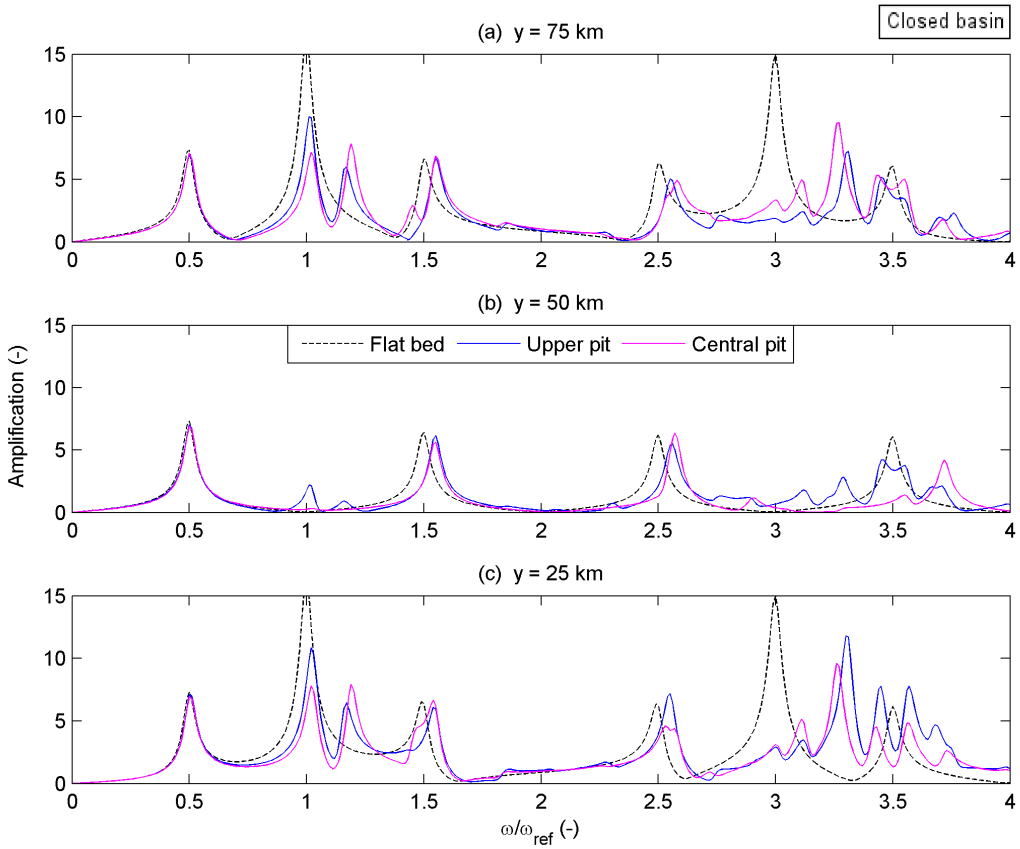

Figure 5.32: Same as Fig. 5.31, but now with **60° wind angle forcing**.

Finally, we will discuss the results of the same cases in the semi-enclosed basin. The results of the 30° and 60° wind angle forcing cases are presented in Figures 5.33 and 5.34 respectively. Again we notice in both figures the difference in peak amplitudes of the upper pit case at points P and R: lower peak amplitudes at point P near the pit location, than at point R. This also applies to the results of the central pit case where the peak amplitudes are lower at point Q near the pit location, than at points P and R in both wind angle results. We further notice that the peak amplitudes of the central pit case at points P and R are no longer the same at all frequencies: the peak amplitudes at frequency 3.25 are higher at point P than at point R in both wind angle cases. We noticed these differences already in the results of the flat bed and shoal cases in the semi-enclosed basin, particularly at frequency 1.25, which is possibly a result of the lack of symmetry in the semi-enclosed basin. Furthermore, if we compare the 30° and 60° wind angle results of the upper pit case at point Q, we see some amplitude outliers around frequency 3.25 in the 60° wind angle case, which were absent in the 30° wind angle case.

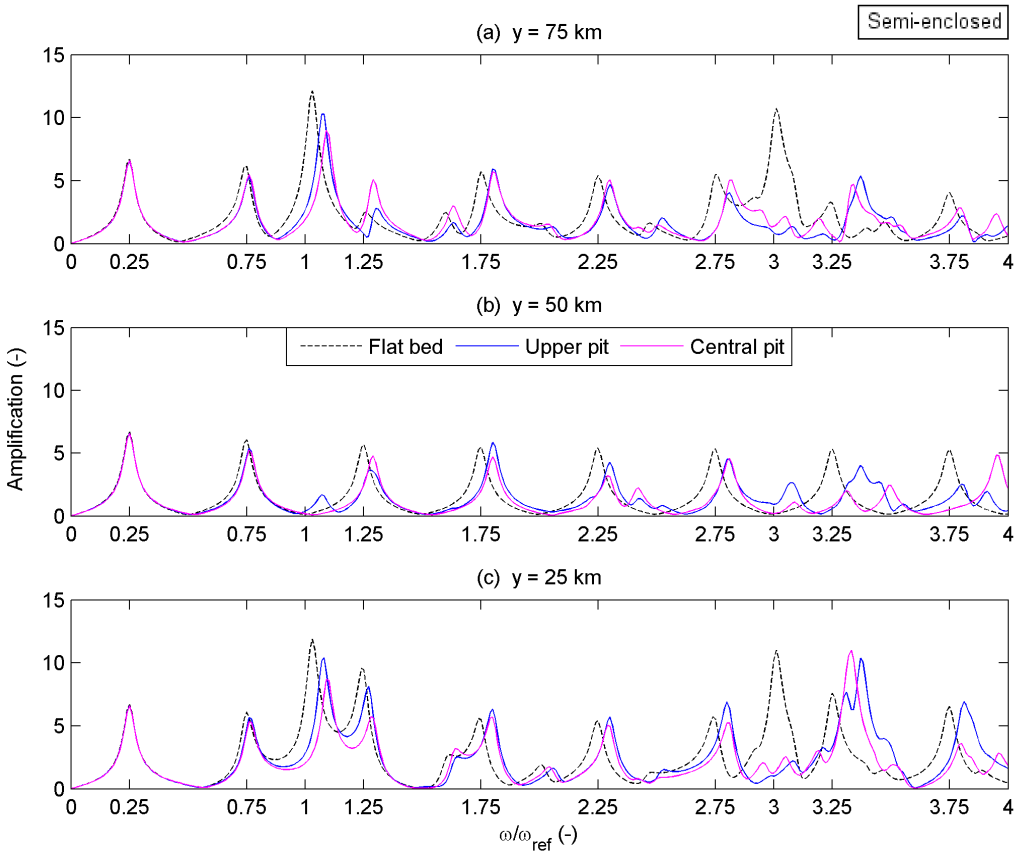

Figure 5.33: Same as Fig. 5.31, but now for the semi-enclosed basin: **30° wind angle forcing** is applied.

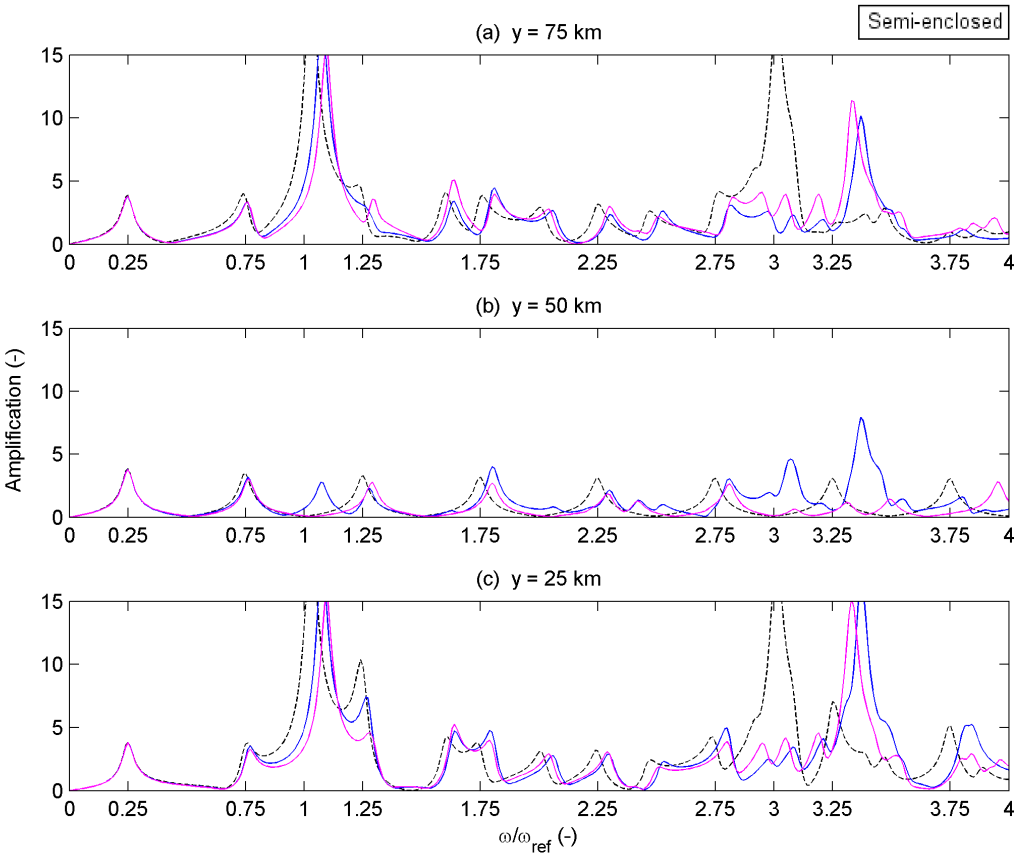

Figure 5.34: Same as Fig. 5.33, but now with **60° wind angle forcing**.

5.5 Summary

At first we explained the main model settings and some underlying assumptions of the 3-D FEM model. Due to our simplified model domain, we have applied a structured grid composed of triangular elements. The model simulations in this chapter were performed with at least 300 frequency modes (300-400) for both the closed and the semi-enclosed basins.

The values for the applied bottom friction coefficient s ($m\ s^{-1}$) were s = 10^{-10} (assuming no friction), 10^{-4} (weak friction) and 10^{-3} (moderate friction) for comparison between both flow models and calibrating r-values for the 1-DH model in Section 5.2. In turn, a fixed value was chosen in between weak and moderate friction, s = 5 x 10^{-4}, to continue the FEM simulations with for the conducted sensitivity analyses in sections 5.3 and 5.4. Moreover, a remarkable difference between the simulations of both flow models had been discovered, for the time being devoted to the fact of featuring the basin hydrodynamics differently in the 1-DH approach versus the 3-D approach.

At the same time, a default value (K_v = 0.012 ($m^2\ s^{-1}$)) was applied to represent the vertical eddy viscosity in all FEM simulations. In order to give an indication of its validity, the bottom friction of the 1-DH model was expressed as a function of the roughness set (s, K_v) of the FEM model by means of expressing the 3-D velocity of the FEM model in a 1-DH flow velocity for a steady flow condition (derived in Appendix C). This resulted in realistic values for K_v, especially for the semi-enclosed basin.

Finally, sensitivity analyses could be conducted regarding the influence of varying topographic elements, such as pits and shoals, in front of the evaluation points along the coast, subject to periodic wind forcing in various angles, on the basin's spectral response at various evaluations points. Since this was a rather comprehensive study, the main findings will be treated briefly. As expected, the shoal and pit locations influences the spatial behavior of the spectral response along the basin, especially at the highest frequencies of the studied frequency range (M*(0.01* ω_{ref}) rad s^{-1}) of the periodic wind forcing. Induced by cross-basin wind forcing, resonant peaks shift to lower (higher) frequencies when a shoal (pit) is implemented, with larger shifts at higher frequencies again. Moreover, new but lower peaks emerge at frequencies around the resonant frequencies of the shoal and pit cases, which were not (slightly) present in the flat bed case of the closed (semi-enclosed) basin. How these effects translates in the time-dependent response (set-up along the coast), will be treated in the next chapter.

Chapter 6

Time-dependent response of the basin's surface elevation to a single wind event

In this chapter we will illustrate how the basin's spectral response to a single wind event is obtained from the basin's spectral response to periodic forcing and the wind spectrum, and how it translates into the basin's time-dependent response of the surface elevation. In order to demonstrate the relevance and possibilities of the model approach we have selected a few examples of pit and shoal cases in the closed and semi-enclosed basin, forced by different wind events. Furthermore, each case is compared to the reference flat bed case. The basin dimensions and wind characteristics in the following examples are set in such a way that certain effects on the behavior of the time-dependent elevation are highlighted properly. The model simulations have been done with the 1-DH model (Section 6.1) and the FEM model (Sections 6.2 & 6.3).

6.1 Flat bed case versus pit case in the 1-DH model

The spectral response to periodic forcing, as obtained from our models in previous chapters, displays in particular resonance peaks with corresponding resonant frequencies at a certain evaluation point in the basin. In turn, when a single wind event is forced onto the basin, the wind spectrum indicates to what extent these resonant frequencies are excited by the wind event. In fact, the product of these two quantities will give the basin's spectral response to the wind event under consideration. Finally, the inverse Fourier transform is applied to convert this latter spectral response in to the surface elevation as a function of time.

According to the well known Beaufort wind force scale (Saucier, 1955), a single wind event with a wind speed of 30 m s^{-1} (at 10 m height) can be considered as a storm (Beaufort force 11). From Eq. (3.7), it follows that this corresponds to a wind stress of 3 N m^{-2}. First, we will consider a wind event that imposes a spatially uniform wind forcing of 3 N m^{-2} onto our reference basin in the along-basin direction. The effective duration of the wind event is set to 6 hours with a ramp stage duration of 2 hours to represent the spin-up and spin-down of the forcing. The wind event has a recurrence time T_{recur} of 16.5 days, which follows from the minimum frequency ($0.01 \cdot (\omega_{ref})$: 4.4 x 10^{-6} rad s^{-1}) applied in the model simulations. The wind forcing will be imposed onto two separate cases in the 1-DH model: a flat bed topography and a pit case in the closed basin with bottom friction coefficient r = 5 x 10^{-4} m s^{-1} in both cases. Here we have chosen for an extreme example of the pit case with basin dimensions: h_1 = 20 m; L_1 = 50 km; h_2 = 40 m; L_2 = 150 km. A side view of the basin's step topography is presented in Figure 6.1. The results of both cases will be presented by a spectral representation (*a*, *c*) and a temporal representation (*b*, *d*) at the rear end of the basin, shown in Figure 6.2.

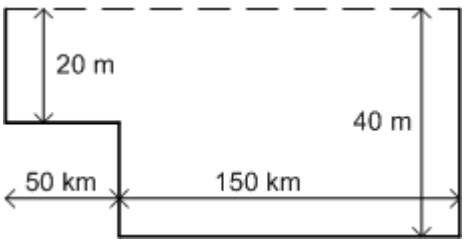

Figure 6.1: Side view sketch of the closed basin's step topography of the pit case in the 1-DH model. Depths are in meters, lengths in kilometers. Note: the vertical scale has been strongly exaggerated with respect to the horizontal scale.

First we will focus on the flat bed case results, which are shown in the top plots of Figure 6.2. The pink curve of Figure 6.2a represents the basin's spectral response to the wind event, which is a product of the wind spectrum (grey) and the basin's spectral response to periodic forcing (blue). Here, the spectral response $|N|$ at the evaluation point is presented by the absolute value of the complex amplitude of the surface elevation in meter. Figure 6.2a clearly shows that the first resonant peak of the basin's spectral response (blue) is excited the most by the wind event (grey), which results in a large peak of the basin's actual response (pink) at that resonant frequency. In turn, the basin's actual response in the spectral representation has been converted to the temporal representation using the inverse Fourier transform function (Eq. 2.5), which finally resulted in the basin's time-dependent response of the surface elevation to the wind event, represented by the black curve shown in Figure 6.2b. The grey curve in the same figure represents the original wind event as a function of time, simulated as a superposition of Fourier modes.

It is important to emphasize that the basin's actual response (pink) can be lowered significantly if the resonant peaks of the basin's spectral response (blue) coincides with a trough of the wind spectrum (grey). We have shown in Chapter 4 that resonant peaks of the basin's spectral response will shift to higher frequencies if the basin dimensions are set to a so-called pit case. Since we want to trigger the first resonant peak coinciding with the trough of the wind spectrum, the resonant peak has to shift far to the right. Therefore the pit case dimensions were set according to Figure 6.1.

The results of the pit case are presented in the bottom plots of Figure 6.2. Figure 6.2c clearly demonstrates that the first peak of the blue curve coincides with the trough of the grey curve at the first resonant frequency, resulting in a significantly lowered actual response (pink) of the basin at this frequency. As a result, the maximum elevation in the pit case has decreased significantly relative to the maximum elevation in the flat bed case (see black curves in Fig. 6.2b, d). Moreover, it demonstrates that the sloshing in the pit case is damped out almost completely after half a day, whereas the sloshing period in the flat bed case takes considerably longer.

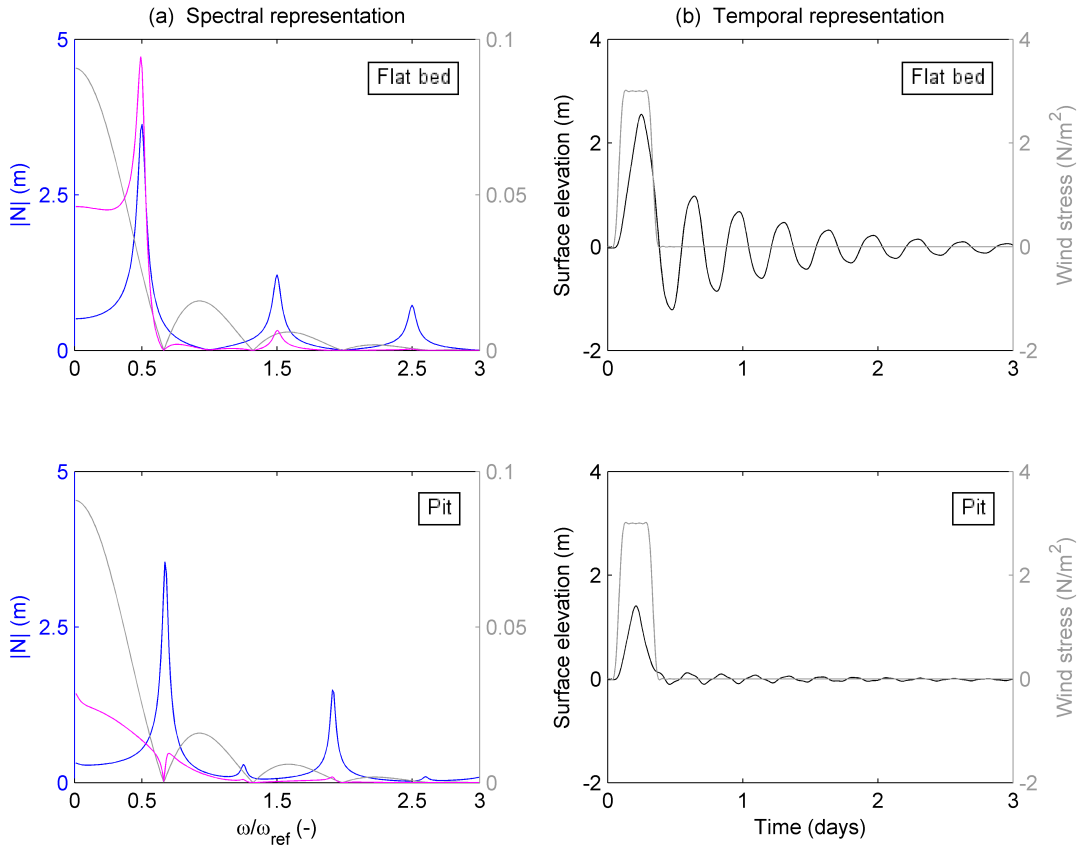

Figure 6.2: Response of surface elevation of the flat bed case (*top*) and the pit case (*bottom*) at the rear end of the **closed basin**, forced by an along-basin wind event with an effective duration of 6 h. The plots on the *left* show the spectral representation of the wind event (*grey*) as well as the response to periodic forcing (*blue*), and the actual response to the wind event (*pink*) for both cases. The plots on the *right* show the temporal representation of both forcing (*grey*) and response (*black*) for both cases. Simulations are performed in the 1-DH model with parameter values as specified in main text.

6.2 Flat bed case versus shoal case in the FEM model

In line with the previous section, we will discuss here the results of a certain case in the FEM model that we treated already in Chapter 5 (Section 5.4.2) in relation to the flat bed case.

A single wind event, with a 3 N m^{-2} wind stress and a 60° wind angle, will be forced upon the flat bed case and the central shoal case (see Figure 6.3) in the semi-enclosed basin. Recall that the basin dimensions are (effectively): 50 km length, 50 km width, 10 m height and a smoothed slope length of 8 km. The bottom friction coefficient is set to s = 5 x 10^{-4} m s^{-1} in both cases. The effective wind duration is set to 9 hours with a ramp stage duration of 2 hours and a recurrence time of 16.5 days. The results of both cases will be analyzed at evaluation point y = 12.5 km. We already noticed from the cross-basin wind simulations in Chapter 5 (see Figs. 5.12b & 5.14b) that the resonance peaks of the central shoal case have been shifted to lower frequencies with slightly lower amplitudes compared to the flat bed case at the concerning evaluation point. Since the resonance peaks of the cases under consideration are dominated by the cross-basin wind contribution, this spectral response behavior is expected here as well. Next, we will show how this affects the time-dependent response of the basin's surface elevation.

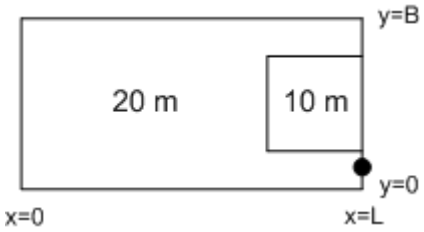

Figure 6.3: Top view sketch of the shoal case in the FEM model. The *black dot* indicates evaluation point *y* = 12.5 km. Depths in the basin are indicated with 10 and 20 m. Sloping of the bed topography not presented in this sketch (see Fig. 5.13b for the actual sloping approach).

Just as in the previous section, the results of both cases will be compared in the spectral and temporal representation, shown in Figure 6.4. Regarding the spectral representation, Figure 6.4c clearly shows that the largest resonant peak of the shoal case coincides with the second trough of the wind spectrum, in contrast to the resonant peak of the flat bed case (Figure 6.4a). Thereto, the actual basin's response (pink curve) of the shoal case is lower than the flat bed case at that frequency as well. However, this difference is barely reflected in the temporal representation. After all, the differences between Figure 6.4*b* and *d* are not that big. The oscillating activity is almost the same in both cases.

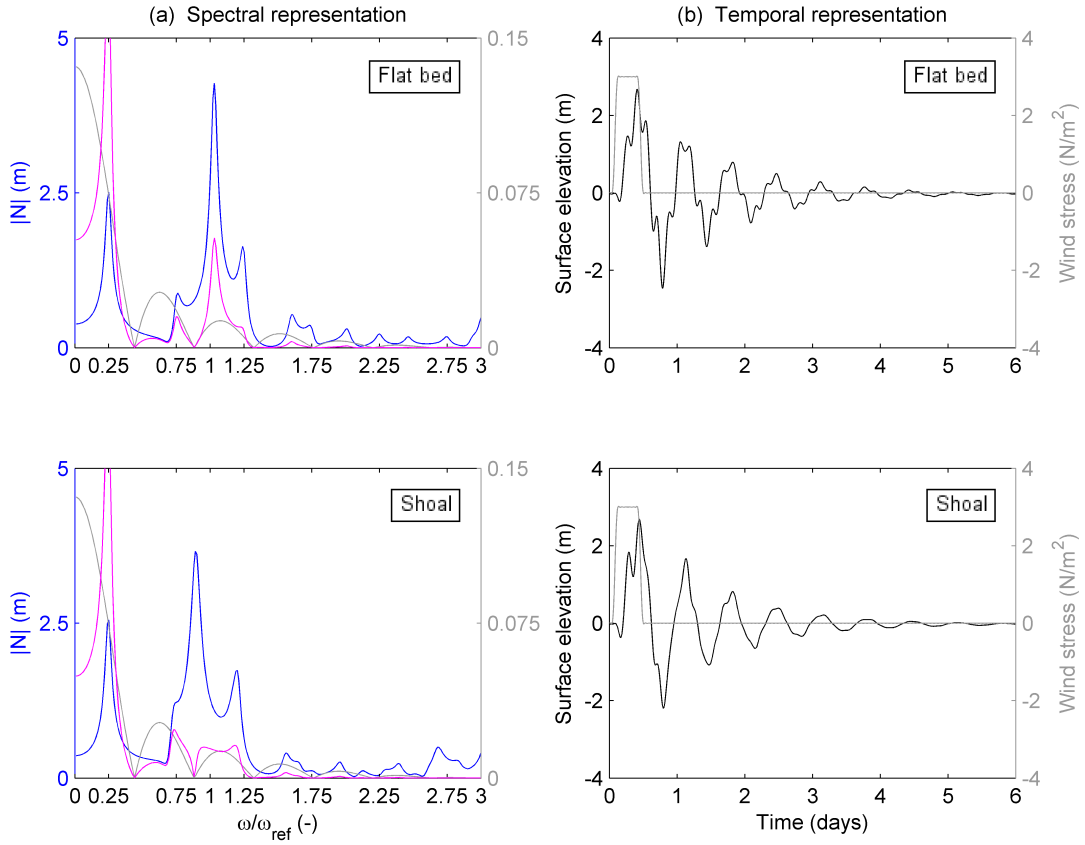

Figure 6.4: Same as Fig. 6.2, but now for the flat bed case (*top*) and shoal case (*bottom*) in the **semi-enclosed basin**, simulated in the FEM model at evaluation point *y* = 12.5 km. Both cases are forced by a wind event with an effective duration of 9 h and a 60° wind angle.

This example clearly shows that despite constraining the largest resonant peak, the influence on the basin's time-dependent elevation is limited in certain cases. It turns out that especially the behavior of the first resonant peak has a big influence on the magnitude of the time-dependent elevation. That is because the wind spectrum has the largest magnitude, and thus the strongest influence, at the lowest frequencies. Thus, in order to lower the basin's time-dependent elevation significantly, the best result is obtained when the first resonant peak of the basin's spectral response coincides with a trough of the wind spectrum.

6.3 Flat bed case versus pit case in the FEM model

In this section we will discuss an example of a pit case with a more extreme pit volume in the semi-enclosed basin and compare its results with the flat bed case results. The bottom friction coefficient is set to s = 5 x 10^{-4} m s^{-1} in both cases. The pit dimensions have been set to: 108 km length, 58 km width, 30 m depth and a smoothed slope length of 8 km, which effectively gives a pit of 100 km length, 50 km width and 30 m depth. A sketch of the pit location is shown in Figure 6.5.

A single wind event with a 3 N m^{-2} wind stress will be forced upon both cases. This time the wind event has a cross-basin wind forcing (90° wind angle) with an effective wind duration of 6.5 hours, a ramp stage duration of 2 hours and a recurrence time of 16.5 days. The results of both cases will be analyzed at evaluation point y = 87.5 km and compared in the spectral and temporal representation, shown in Figure 6.6.

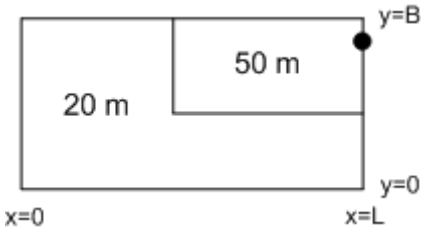

Figure 6.5: Top view sketch of the pit case in the FEM model. The *black dot* indicates evaluation point y = 87.5 km. Depths in the basin are indicated with 20 and 50 m. Again, the sloping contours left out of the figure for simplicity.

At first, the plots of Figure 6.6*a* and *c* clearly demonstrate the difference in amplitude of the first dominant resonant peak of the basin's spectral response (blue curve). The amplitude of this peak is much lower in the pit case than in the flat bed case. In addition to that, this peak has shifted significantly to a higher frequency in the pit case compared to the flat bed case. Moreover, the dominant resonant peak of the pit case coincides with the trough of the wind spectrum, in contrast to the flat bed case. Therefore, the actual response (pink curve) of the pit case is damped significantly, in contrast to the actual response of the flat bed case. As a result, the basin's elevation of the pit case is much lower and its sloshing behavior over time a lot calmer compared to the flat bed case (black curves in Fig. 6.2b, d). In conclusion, the oscillating activity at the concerning evaluation point is a lot less in the pit case than in the flat bed case under these conditions.

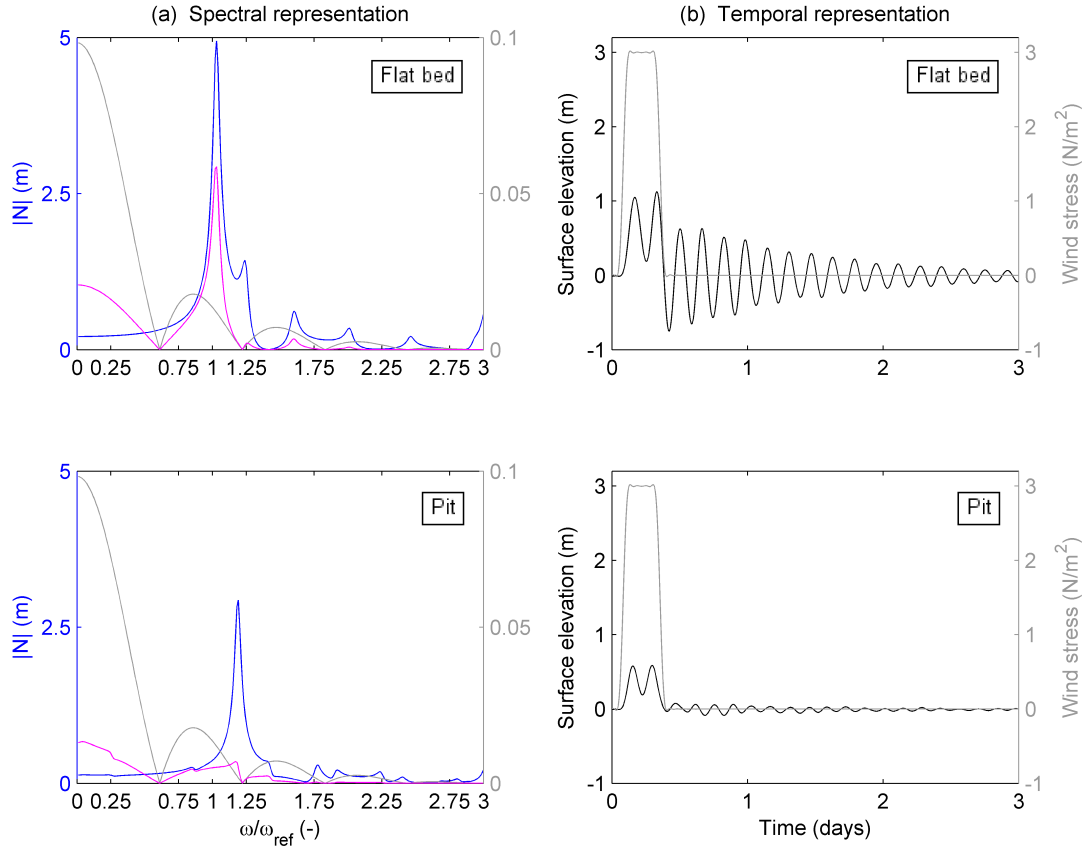

Figure 6.6: Same as Fig. 6.4, but now for the pit case instead of the shoal case in the **semi-enclosed basin** at evaluation point *y* = 87.5 km. Both cases are forced by a wind event with an effective duration of 6.5 h in cross-basin direction.

6.4 Summary

The behavior of the wind driven response of the time-dependent surface elevation along the coast for each case treated in this chapter, have been explained mainly by the spectra, of the wind forcing and the basin's spectral response to periodic wind forcing, in the frequency domain of the cases under consideration. Hereby, we have applied our gathered findings of the previous chapters regarding these spectra.

Furthermore, it turns out that the lower frequencies of the periodic wind forcing input clearly dominate the behavior of the time-dependent set-up induced by a wind event, relative to higher frequencies. This can be explained by the fact that due to the applied characteristics of a wind event, a large portion of the wind spectrum's energy is distributed over the lower frequencies of the spectrum, experienced already in Chapter 2.

Moreover, this chapter demonstrates how to trigger optimal set-up behavior by modifying the basin topography for a given wind event with a certain wind speed, wind duration, ramp stage and wind angle.

Chapter 7

Discussion

In this chapter, some important assumptions and model choices will be discussed, together with the found results during this research project. First we will treat the assumptions with regard to excluding hydrodynamic processes in the flow models, partly due to adopting a linearised model approach at the start of this project (Section 7.1). Followed by the justification for the applied Dirichlet boundary condition at the open boundary of the semi-enclosed basin and the exclusion of tides (Section 7.2). Finally, we will discuss the model performance of the FEM model regarding accuracy and certain unclarities in the model results in Section 7.3.

7.1 Hydrodynamic processes in our linearised model approach

The model formulations of our flow models used in this study are based on the linearised shallow water equations. By assuming linear dynamics, non-linear processes will be neglected. This implies that we assume a small Froude number:

$$F_r = \frac{U}{\sqrt{gh}} \ll 1. \tag{7.1}$$

With typical scales *U* for flow velocity and *h* for depth. As a result, the surface displacement is small compared to the average water depth, referred to as the rigid lid approximation. As a result, we neglect the non-linear processes such as advection terms and horizontal mixing of momentum.

Although the FEM model is suitable for simulating Coriolis effects, this process is neglected during this study. An important reason for this is that the 1-DH model can not simulate cross-basin dynamics, because of its one-dimensional nature. Another reason is the 'negative' experience of my supervisors (especially W.L. Chen) with applying the Coriolis parameter in FEM model simulations. Negative in a way that the Coriolis effects significantly disturbs the spectral response spectra, intensively applied throughout this study, which makes it a lot harder to interpret these type of results in the frequency domain. Therefore we have chosen to neglect this process completely in this study, to focus on the influence of basin topography, wind direction and bottom friction on the spectral and time-dependent response of the closed and semi-enclosed basin. For a comprehensive analysis regarding the important influences of the Coriolis effects on the basin's spectral response, I will refer to the work of W.L. Chen (2015, PhD thesis).

Bottom friction and the vertical eddy viscosity, which adds turbulence to the system, are both linearly implemented in the model as well. These processes are further discussed in Section 7.3, regarding the influence of these parameters on the model results. Finally, both flow models are driven by wind forcing only, while atmospheric pressure is neglected.

7.2 Boundary conditions

In the semi-enclosed basin, we assume that the sea outside our model domain effectively imposes a Dirichlet boundary condition at the open boundary of our model domain. This implies that the surface elevation is considered to be zero at this open boundary, connecting the model domain with the outer sea. The underlying assumption is that this outer region is large enough to absorb the oscillating effects at the open boundary induced by wind forcing in the coastal basin. This means that waves propagating outside the model domain can be seen as a outward flux with a very small amplitude, which barely affects the elevation of this wide and deep outer region.

As already mentioned, non-linear processes like tide-surge interactions are neglected in this study. However, tides and thus tide-surge interactions could be included in the model by imposing a tidal periodic signal at the open boundary condition. Because we also study closed basins, the tide effects have been excluded entirely.

7.3 Model simulations

In order to conduct the performed sensitivity analyses, computation time of the applied models needs to be manageable. Therefore, we have adopted the idealized process-based modelling approach in the beginning of this study. Furthermore, the applied combination of both flow models with the Fourier transform approach allows us to perform the required model simulations rather quick.

A comparison between the 1-DH model simulations and the FEM model simulations has been done in Chapter 5 by reproducing the basin's spectral response for a few simple 1-DH cases by simulating similar cases in the FEM model. Because of the different model approaches of both flow models, the FEM model can not reproduce identical 1-DH model simulations. After all, the 1-DH model is based on one-dimensional depth-averaged flow, whereas the FEM model is based on three-dimensional depth-integrated flow. Nevertheless, simulating identical cases in both models resulted in pretty good similarities of the spectral response behavior of both model simulations.

The statistical measure 'standard error of the estimate' is used to calibrate the bottom friction coefficient r of the 1-DH model. This measure determines the goodness of fit over a sample of frequency simulations. Here, it has been applied over the full frequency range of periodic wind forcing as input for both flow models. One could argue to choose a smaller frequency range to calculate the error and conduct the calibrations at. Namely, a specific frequency range which encloses a certain resonant peak. However, since the purpose for calibration was not to improve the accuracy of the 1-DH simulations, this more general calibration approach was used. The purpose for calibration was to give an indication of the accuracy of the FEM model simulations, with respect to the 1-DH model simulations of identical cases. This is also important with regard to future storm surge research in coastal basins, where this rather new FEM model is expected to be applied for as well. Nevertheless, it would be wise to further calibrate the FEM model parameters, (K_v, s) in particular, and validate its results with real time data of coastal basins in practice. This will be further treated in the next chapter (Recommendations).

It turned out that the degree of fit decreases as the bottom friction coefficient and the complexity of basin topography increases. Another more striking result is that the amplification peaks (in its non-dimensional form) of the 1-DH simulations remain constant for increasing frequencies, in contrast to the peaks of the FEM simulations, which decrease for increasing frequencies for the reference flat bed case in both types of basins (Fig. 5.4). Unfortunately, no solid

explanation has been found yet for these observations other than a different approach of representing the vertical structure of the flow for each model. A more thorough study would be required to give a sound explanation for these observations.

Chapter 8:

Conclusions & Recommendations

This final chapter answers the research questions of this study, treated in Section 8.1. Subsequently, recommendations will be given in Section 8.2, based on the answers of the research questions and the discussion, presented in Chapter 7.

8.1 Conclusions

All the research questions formulated in Chapter 1 will be answered here. Each question is addressed in a separate chapter. The first two questions addresses the applied methods and models. The last three questions contribute to the objective of this study.

1. How is a time-dependent single wind event converted in the frequency domain and how are its characteristics influencing the spectral representation?

The Fourier transform approach enables us to switch easily between the temporal and spectral representations. In this study we consider a single wind event as a periodic signal over time. One important aspect of the Fourier theory is that any smooth periodic signal can be represented as a sum of sinusoids. The periodic signal $y(t)$ can then be decomposed into M sinusoids with appropriate amplitude, phase and frequency components, where M is the number of frequency modes. The resulting Fourier series (Eq. 2.2) can be solved by applying the fast Fourier transform algorithm (Eq. 2.3) to obtain the spectral representation of the single wind event as a function of frequency modes. The same method can be used to convert a signal in the frequency domain back into the time domain, by applying the inverse Fourier transform function (Eq. 2.5), which will come in handy later in Chapter 6 to convert the actual response to a single wind event into the time domain. This approach is treated more fully in Chapter 2, provided with examples.

The duration (T_{event}) and smoothness (T_{ramp}) of a wind event play an important role in the spectral representation of the wind event. An exploratory sensitivity analysis has been conducted regarding the effects of varying T_{event} and T_{ramp}. It turns out that the spectral energy of the wind signal is distributed in more condensed peaks with higher amplitudes when we increase T_{event}. On the other hand, increasing T_{ramp} will lower the amplitudes, especially at higher frequencies.

2. How do we formulate the model conditions in order to simulate the set-up along the basin's coastal boundary for the closed and semi-enclosed basin?

The chosen model domain consist of a rectangular basin with 200 km length and 100 km width for both the closed and the semi-enclosed basin. The linearised shallow water equations are applied to express the hydrodynamic processes in the domain. These equations will be solved either in the 3-D or in the 1-DH flow model, by setting appropriate boundary conditions for both models.

In the 3-D flow model formulation, the system is forced by imposing a time-periodic and space-uniform wind stress at the free surface. Turbulence is represented using a spatially uniform vertical eddy viscosity, combined with a partial slip condition at the bed including bottom friction in a linearised way. Furthermore, a zero transport condition is imposed normal to the closed boundaries in both types of basins, where a zero surface elevation condition is imposed at the open boundary in

the semi-enclosed basin. Due to the linearity of the system, we have used the complex notation to express the wind forcing together with the solution of the surface elevation and currents in a time-periodic fashion, by assuming a dynamic equilibrium.

In the 1-DH model formulation, we assume one-dimensional depth-averaged flow by considering the width of the basin to be very small compared to the length of the basin. The hydrodynamic processes are expressed by the depth-integrated shallow water equations together with the depth-averaged bottom stress formulation. A topographic step approach is applied to address topographic changes in the basin. Again, the complex notation will be used to express the wind forcing together with the solution of the surface elevation and currents in a one-dimensional time-periodic fashion.

3. What are the effects of varying the bottom friction coefficient and topographic basin dimensions on the basin's spectral response at the rear end of the closed and semi-enclosed basin, using the 1-DH flow model?

First of all, the spectral response of a basin driven by periodic wind forcing displays resonance peaks. Increasing bottom friction lowers the resonance peaks. The sensitivity analysis of the basin's depth ratio h_2/h_1 has shown that the classical resonance peaks shift to lower (higher) frequencies when the depth ratio becomes < 1 (> 1), which follows from the fact that waves in shallow water propagate more slowly than waves in deep water. Furthermore, new resonant peaks show up in the spectral response due to breaking of symmetry of the propagating waves caused by topographic differences in the basin. In addition, bottom friction damps the amplification in shallower regions to a higher degree than in deeper regions. This can be explained by the fact that the effective friction coefficient is higher in shallower regions, which leads to larger damping of amplification.

The comparison between the reference flat bed case and a topographic step case, with the same average basin depth, demonstrates that the effective wave speed in the step case is lower than in the flat bed case, whereby peaks shift to lower frequencies. This implies that the shallower region dominates the deeper region of the step case, in terms of influence on the spectral response behavior. The sensitivity analysis of the h/L ratio of the shoal and pit designs has shown that redistributing sand into a pit design results in lower resonant peaks, particularly for high h_{pit}/L_{pit} ratios, compared to redistributing sand into a shoal design, given that the basin volume remains constant in all studied cases. All the cases in both the shoal and the pit design have a lower effective wave speed compared to the reference flat bed case. Moreover, the shoal design dominates the pit design in terms of shifting peaks to lower frequencies. After all, as the $h_{element}/L_{element}$ ratio increases, the effective wave speed in the shoal design decreases more rapidly than in the pit design.

Finally, the results in Chapter 4 show that the semi-enclosed basin simulations in the 1-DH model exhibit many similarities with the closed basin simulations, regarding the spectral response behavior.

4. What is the influence of implementing topographic elements, such as pits and shoals, and wind direction on the basin's spectral response at the rear end of the closed and semi-enclosed basin, using the 3-D flow model?

At first, the results in Chapter 5 show that the size and location of a topographic element, such as a shoal or a pit, strongly influences the spectral response behavior along the coastal boundary of a basin. Induced by along-basin wind forcing, the resonant peaks of the spectral response shift to lower (higher) frequencies when a shoal (pit) is implemented in front of the coastal boundary at the rear end of the basin. These peak shifts increase as the frequency increases, which is in line with the 1-DH

model results in Chapter 4. Furthermore, the location of the shoal and pit influences the spatial behavior of the spectral response along the coastal boundary. Resonant peaks are highest (lowest) at evaluation points near the shoal (pit) location, particularly at higher resonant frequencies. This is true for both types of basins.

Induced by cross-basin wind forcing, resonant peaks shift to lower (higher) frequencies when a shoal (pit) is implemented, with larger shifts at higher frequencies. Moreover, new but lower peaks emerge at frequencies around the resonant frequencies of the shoal and pit cases, which were not (slightly) present in the flat bed case of the closed (semi-enclosed) basin. Compared to the reference flat bed case, the resonant peaks are lower in all the shoal and pit cases (varied at different locations in front of the basin), particularly at higher frequencies. The peaks are even lower in the pit cases than in the shoal cases.

In this linear approach of simulating wind forcing, the spectral response initiated by a spatially uniform wind stress in a certain wind direction is a combination of spectral response contributions by the along-basin and cross-basin wind forcing. To this end, along-basin wind forcing has a high (low) contribution in the spectral response of a low-angle (high-angle) wind forcing case and vice versa for cross-basin wind forcing. Therefore, varying wind direction in the studied cases show similar results to the addressed along- and cross-basin wind forcing cases, proportional to the wind angle contribution of both cases. Concluding, the most substantial influences on the spectral response behavior take place at the higher frequencies of the spectrum in all studied cases of Chapter 5. This will have consequences for the actual influences on the basin's response to a single wind event, treated in the next question.

5. How to obtain the actual response of the time-dependent set-up in the basin, induced by a single wind event? And how is the spectral response reflected in the time-dependent set-up?

The spectral response to periodic forcing, as obtained from our models, displays in particular the resonant frequencies of the basin. When a single wind event is forced onto the basin, the *wind spectrum* indicates to what extent these resonant frequencies are excited by the wind event. The product of these two *quantities* will give the basin's spectral response to the wind event under consideration. Subsequently, the inverse Fourier transform function (Eq. 2.5) will be applied to convert the latter response into the actual response of the time-dependent set-up in the basin.

The sensitivity analysis in Chapter 2 already demonstrated that for various single wind events, a large portion of the wind spectrum's energy is distributed over the lower frequencies of the spectrum. Therefore, the basin's spectral response will be excited the most at these lower frequencies by the wind event under consideration. This implies that the lowest frequencies of the basin's spectral response influence the basin's actual response to a single wind event the strongest. Moreover, it turns out that the basin's actual response can be lowered significantly when the resonant peaks of the basin's spectral response coincides with a trough of the wind spectrum. In turn, gained insights about the sensitivity of the spectral response to certain basin specifications, obtained from the sensitivity analyses in Chapter 4 and 5, enables us to modify the topographic dimensions in such a way that particularly the first resonant peak of the basin's spectral response coincides with a trough of the wind spectrum for a given wind event blowing in a certain direction.
Finally, examples of a few cases, with various topographic elements and various wind angles of several events, in Chapter 6 have shown that applying the gained insights of this method properly can yield a major reduction of the oscillating activity of the basin's surface elevation over time.

8.2 Recommendations

In Chapter 7 we already referred to recommendations for further improvement of the accuracy of FEM model simulations. To this end, it would be recommended to calibrate and validate on the basis of real time data of existing coastal basins, and in particular coastal basins that are frequently subject to severe storms and/or wind events, such as for example the Bay of Bengal along the coast of Bangladesh (e.g. Dube et al., 2009). Thus, validation based on real time data in favor of existing or analytical models, at which this study and its conducted results are based on. However, the fact remains that such a model is mostly easy in use and can generate lots of data. My personal experience is that it helped me a lot with understanding the complex matter, simply by the fact that I could generate fast and lots of data to focus on uncertainties in the model results (trial and error). This obviously depends on your research goal, where in this research project a better understanding of processes by (sometimes strongly) simplifying these processes through de imposed conditions on the flow model. Therefore I recommend a very clear goal and a systematic plan of approach beforehand, when there is the possibility to generate a lot of data in little time.

Furthermore, there are lots of possibilities to study further with these types of flow models (FEM model) which needs relatively little computation time. Some general ideas are first of all implementing and varying more complex geometries of the basin. After all, the FEM model is highly suitable for this approach because it can deal with both structured grids as well as unstructured grids. In this study we have applied the structured grid of the FEM model, because of the strongly simplified considered geometry of the basins. Second, the size of topographic elements can be varied in many ways: in width, length and/or depth; in volume relative to the basin's volume (regarding the small sensitivity study conducted in Section 4.2.3); even in combination with several complex geometries (which was also a serious consideration prior to this study) and many more I would say. Finally, inclusion of more (non-linear) processes such as tide, Coriolis effects and advection. But that perhaps entails too much complexity, resulting in an exponential increase in computation time (expectation), losing its big advantage of the applied modeling approach, namely little computation time. Therefore it is very important to figure out beforehand what the real purpose is of applying the FEM model in future study.

That brings me to mention that the basin's spectral response results of this research project perhaps predominates the basin's time dependent response, which means there is an opportunity for future studies to elaborate further on the latter response. However I recommend for follow up studies with regard to the just mentioned possibilities for these flow models, to look for challenging real time case studies. Further simulations of random cases to trigger the optimal conditions in a basin will not directly meets to a certain need of better safety in high risk areas for example. A more specific example would be to assess in advance the common wind events of a high-risk coastal area in practice. And mainly focus on wind event duration and angle is my suggestion for a challenging case study. Since these two wind characteristics influence the Fourier wind spectra the strongest and therefore *probably* also basin's time-dependent set-up. Probably, because this mainly depends on the basin's resonant frequency response, whether these frequencies will be excited by the wind event or not. And like I showed in this study, these resonant frequencies depend on a lot of factors, such as the basin dimensions (geometry, topography). Yet again, that was not the goal of *this* study but it is just a general recommendation for further research. A win win situation I would say.

Bibliography

Beets, D. J. & Spek, A.J.F. (1999) The Holocene evolution of the barrier and the back-barrier basins of Belgium and the Netherlands. *Netherlands Journal of Geosciences*. Southern Bight image.

Berg, N. J. (2013) On the influence of storm parameters on extreme surge events at the Dutch coast. *M. Sc. Thesis, University of Twente, Department of Water Engineering and Management,* 140 *pp.*

Bertin, X., Bruneau, N., Breilh, J.-F., Fortunato, A. B. & Karpytchec, M. (2012) Importance of wave age and resonance in storm surges: The case of Xynthia, Bay of Biscay. *Ocean Modelling, Vol.* 42*, pp.* 16-30.

Brown, J.M., Souza, A.J. & Wolf, J. (2010) An 11-year validation of wave-surge modelling in the Irish Sea, using a nested POLCOMS-WAM modelling system. *Ocean Modelling, Vol.* 33*, pp.* 118-128.

Chen, C., Beardsley, R.C. & Cowles, G. (2006) An unstructured grid, finite-volume coastal ocean model (FVCOM) System. *Oceanography*, *Vol.* 19, *pp.* 78-89.

Chen, Q., Wang, L., Tawes, R. (2008) Hydrodynamic response of Northeastern Gulf of Mexico to hurricanes. *Estuaries and Coasts, Vol.* 31*, pp.* 1098-1116.

Chen, W.L., Roos, P.C., Schuttelaars, H.M., Kumar, M. & Hulscher, S.J.M.H. (2013) *Manuscript*: A new way to study surge problem. *Private communication*.

Chen, W.L., Roos, P.C., Schuttelaars, H.M. & Hulscher, S.J.M.H. (2014) Storm surge response in large-scale basins: influence op topography. *Proceedings of the 17th PECS conference*, *Brazil*, *October 2014*.

Chen, W.L. (2015) Idealised modelling of storm surges in large-scale coastal basins. *PhD thesis, University of Twente, Engineering Technology (CTW),* 134 *pp*.

Chen, W.L., Roos, P.C., Schuttelaars, H.M. & Hulscher, S.J.M.H. (2015) Resonance properties of a closed rotating rectangular basin subject to space- and time-dependent wind forcing. *Ocean Dynamics, Vol.* 65 *(*3*), pp.* 325-339.

Chen, W.L., Roos, P.C., Schuttelaars, H.M., Kumar, M., Zitman, T.J. & Hulscher, S.J.M.H. (2016) Response of large-scale coastal basins to wind forcing: influence of topography. *Ocean Dynamics, Vol.* 66 (4)*, pp.* 549-565.

Craig, P.D. (1989) Constant-eddy-viscosity models of vertical structure forced by periodic wind. *Continental Shelf Research*, *Vol.* 9, *pp.* 343-358.

Dube, S. K., Jain, I., Rao, A. D. & Murty, T. S. (2009) Storm surge modeling for the Bay of Bengal and Arabian Sea. *Natural Hazards, Vol.* 51*, pp.* 3-27.

Duhamel, P., Piron, B. & Etcheto, J.M. (1988) On computing the inverse DFT. *IEEE Trans. Acoust., Speech and Sig. Processing, Vol.* 36 (2)*, pp.* 285-286.

Gill, A.E. (1982) Atmosphere-Ocean Dynamics. *International Geophysics Series, Vol.* 30*,* 662 *pp.*

Guo, Y.K., Zhang, J.S., Zhang, L.X. & Shen, Y.M. (2009) Computational investigation of typhoon-induced storm surge in Hangzhou Bay, China. *Estuarine, Coastal and Shelf Science, Vol.* 85*, pp.* 530-536.

Holland, G.J. (1980) An analytic model of the wind and pressure profiles in hurricanes. *Monthly weather review, Vol.* 108*, pp.* 1212-1218*.*

Hulscher, S.J.M.H., Ribberink, J.S. & Knaapen, M.A.F. (2002) Syllabus Marine Dynamics. *Faculty of Engineering Technology, University of Twente.*

Intergovernmental Panel on Climate Change (IPCC) (2007) Climate Change 2007: Impacts, adaptation and vulnerability. *Working Group I Report, The Physical Science Basis, Chapter 10, Global Climate projection, World Meteorological Organization, pp.* 812-822*.*

Irish, J. L., Resio, D. T. & Ratcliff, J. J. (2008) The influence of storm size on hurricane surge. *Journal of Physical Oceanography, Vol.* 38*, pp.* 2003-2013.

Jones, J.E. & Davies, A.M. (2007) Influence on non-linear effects upon surge elevations along the west coast of Britain. *Ocean Dynamics, Vol.* 57*, pp.* 401-416.

Moon, I.–J., Kwon, J.–I, Lee, J.C., Shim, J.–S., Kang, S.K., Oh, I.S., Kwon, S.J. (2009) Effect of the surface wind stress parameterization on the storm surge modeling. *Ocean Modelling, Vol.* 29*, pp.* 115-127.

Online Statistics Education: A Multimedia Course of Study (http://onlinestatbook.com). Project Leader: David M. Lane, Rice University. Retrieved at November 2015.

Ponte, A.L. (2010) Periodic wind-driven circulation in an elongated and rotating basin. *Journal of Physical Oceanography, Vol.* 40*, pp.* 2043-2058.

Pugh, D.T. (1987) Tides, Surges and Mean Sea-Level. *Natural Environment Research Council, Swindon, UK,* 472 *pp.*

Rao, D.B. (1966) Free gravitational oscillations in rotating rectangular basins. *Journal of Fluid Mechanics, Vol.* 25 (3), *pp*. 523-555.

Roos, P.C. (2009) Syllabus Mathematical Physics of Water Systems. *Faculty of Engineering Technology, University of Twente, January,* 2009*.*

Roos, P.C. (2014) Syllabus Marine Dynamics. *Faculty of Engineering Technology, University of Twente, version* 2*: January* 21*,* 2014*.*

Roos, P.C., Hulscher, S.J.M.H. & De Vriend, H.J. (2008) Modelling the morphodynamic impact of offshore sandpit geometries. *Coastal Engineering, Vol.* 55*, pp.* 704-715.

Saucier, W.J. (1955) Principles of Meteorological Analysis. *University of Chicago Press*, 438 *pp.*

Van der Molen, J., Gerrits, J. & de Swart, H.E. (2004) Modelling the morphodynamics of a tidal shelf sea. *Continental Shelf Research, Vol.* 24*, pp.* 483-507.

Walstra, D.J.R., Van Rijn, L.C., Hoogewoning, S.E., Aarninkhof, G.J. (1999) Modeling of sedimentation of dredged trenches and channels under the combined action of tidal currents and waves. *WL | Delft Hydraulics*, 16 pp.

Weisberg, R.H. & Zheng, L. (2006b) Hurricane Storm Surge Simulations for Tampa Bay. *Estuaries and Coasts, Vol.* 29*,* 99. 899-913.

Weisberg, R.H. & Zheng, L. (2006c) A simulation of the hurricane Charley storm surge and its breach of North Captiva Island. *Florida Scientist, Vol.* 69*, pp.* 152-165*.*

Weisstein, E.W. (2015) Fourier Series. *MathWorld – A Wolfram Web Resource.* http://mathworld.wolfram.com/FouriersSeries.html. Retrieved at July 2015.

Wu, J. (1982) Wind-stress coefficients over sea surface from breeze to hurricane. *Journal of Geophysical Research, Vol.* 87*, pp.* 9704-9706*.*

Appendix A

Solution method of the analytical 1-DH model

A.1 Outline of the solution method

From the hydrodynamics in Section 3.2.2, the linearised depth-averaged shallow water equations (3.13 & 3.14) can be solved by introducing complex amplitudes, under the assumptions of a dynamic equilibrium and a linear system of equations. In this way the problem is reduced to solving for the complex amplitudes of the currents and the surface water elevation. Recall that these amplitudes satisfy

$$-i\omega N + h\frac{\partial U}{\partial x} = 0 \tag{3.23}$$

$$-i\omega\gamma^2 U = -g\frac{\partial N}{\partial x} + \frac{T^{(x)}}{h}, \qquad \text{with } \gamma^2 = \left(1 + \frac{ir}{\omega h}\right). \tag{3.24}$$

Subsequently, the differential problem can be expressed as a single equation for amplitude *N* only, by applying some straightforward differential operations. Take the space derivative of Eq. (3.24) and multiply with *h*. Multiply Eq. (3.23) with $i\omega\gamma^2$. Then the summation of these two equations will form the single equation for complex amplitude *N*, which is given by

$$\frac{\partial^2 N}{\partial x^2} + \gamma^2 k^2 N = 0. \tag{A.1}$$

Because the basin is divided in two compartments due to the single step topography, the solution for *N* will be separated per compartment as well. This results in two general solutions to the Helmholtz Eq. (A.1) for compartment 1 and 2, denoted with subscripts 1 and 2:

$$N_1 = A_1\cos(\gamma_1 k_1 x) + B_1\sin(\gamma_1 k_1 x), \tag{A.2}$$

$$N_2 = A_2\cos(\gamma_2 k_2 x) + B_2\sin(\gamma_2 k_2 x), \tag{A.3}$$

$$\text{with } k_n = \frac{\omega}{\sqrt{gh_n}} \quad \text{and } \gamma_n = \sqrt{1 + \frac{ir}{\omega h_n}}. \qquad (n = 1,2) \tag{A.4}$$

A.2 Solution for the closed basin

In this single step topography setting, next to the horizontal boundary conditions, two extra continuity conditions apply at the interface (*x* = 0). Continuity of volume transport is expressed as $U_1h_1 = U_2h_2$ at *x* = 0. Continuity of surface elevation is expressed as $N_1 = N_2$ at *x* = 0. The subscripts

refer to the concerning compartments of the basin. Together with the horizontal boundary conditions the following four conditions apply for amplitude *N*:

$$\frac{\partial N_1}{\partial x} = \frac{T^{(x)}}{gh_1} \quad at\ x = -L_1, \qquad \frac{\partial N_2}{\partial x} = \frac{T^{(x)}}{gh_2} \quad at\ x = L_2. \tag{A.5}$$

$$\frac{\partial N_1}{\partial x} = \frac{h_2}{h_1}\frac{\partial N_2}{\partial x} \quad at\ x = 0, \qquad N_1 = N_2 \quad at\ x = 0. \tag{A.6}$$

The expressions of N_1 and N_2 in Eqs. (A.2) & (A.3) in Section A.1 can now be further solved with these four conditions. Therefore coefficients A_1, A_2, B_1 and B_2 have to derived. Substituting the first boundary condition at $x = -L_1$ in the equation of N_1 gives

$$B_1 = \frac{T^{(x)}}{gh_1\gamma_1 k_1 \cos(\gamma_1 k_1 L_1)} - A_1 \tan(\gamma_1 k_1 L_1)\,. \tag{A.7}$$

Substituting the second boundary condition at $x = L_2$ gives

$$B_2 = A_2 \tan(\gamma_2 k_2 L_2) + \frac{T^{(x)}}{gh_2\gamma_2 k_2 \cos(\gamma_2 k_2 L_2)}. \tag{A.8}$$

Substituting the first matching condition at $x = 0$ gives

$$B_1 = \frac{h_2\gamma_2 k_2}{h_1\gamma_1 k_1} B_2. \tag{A.9}$$

From the second matching condition it follows that $A_1 = A_2$. Substituting Eqs. (A.7) and (A.8) in Eq. (A.9) will give

$$A_1 = \frac{T^{(x)}}{gh_1\gamma_1 k_1}\left(\frac{\cos(\gamma_2 k_2 L_2) - \cos(\gamma_1 k_1 L_1)}{\mu \sin(\gamma_2 k_2 L_2)\cos(\gamma_1 k_1 L_1) + \sin(\gamma_1 k_1 L_1)\cos(\gamma_2 k_2 L_2)}\right), \tag{A.10}$$

$$\text{with } \mu = \frac{h_2\gamma_2 k_2}{h_1\gamma_1 k_1}.$$

The derived solution for A_1 can now be substituted in Eq. (A.8). Notice that $A_1 = A_2$, which gives

$$B_2 = \frac{T^{(x)} \tan(\gamma_2 k_2 L_2)}{gh_1\gamma_1 k_1}\left(\frac{\cos(\gamma_2 k_2 L_2) - \cos(\gamma_1 k_1 L_1)}{\mu \sin(\gamma_2 k_2 L_2)\cos(\gamma_1 k_1 L_1) + \sin(\gamma_1 k_1 L_1)\cos(\gamma_2 k_2 L_2)}\right) \tag{A.11}$$

$$+ \frac{T^{(x)}}{gh_2\gamma_2 k_2 \cos(\gamma_2 k_2 L_2)}.$$

To find the full solution of $N_2(L_2)$, the derived coefficients A_2 and B_2 will be substituted in Eq. (A.3). This results in

$$N_2(L_2)_{\text{closed}} = \frac{T^{(x)}}{gh_1\gamma_1 k_1}\left(\frac{1 + \frac{1}{\mu}\sin(\gamma_1 k_1 L_1)\sin(\gamma_2 k_2 L_2) - \cos(\gamma_1 k_1 L_1)\cos(\gamma_2 k_2 L_2)}{\mu \sin(\gamma_2 k_2 L_2)\cos(\gamma_1 k_1 L_1) + \sin(\gamma_1 k_1 L_1)\cos(\gamma_2 k_2 L_2)}\right). \tag{A.12}$$

In turn, the solutions for the flat bed case with and without bottom friction will be derived from this expression (A.12).

Flat bed with bottom friction

The solution for the flat bed case with bottom friction can be obtained by substituting L_2 = 0 in expression (A.12), leaving L_1 capturing the basin length L:

$$N(L)_{\text{closed}} = \frac{T^{(x)}}{gh\gamma k}\left(\frac{1-\cos\gamma kL}{\sin\gamma kL}\right). \qquad (A.13)$$

This solution (A.13) has been used in Section 4.1 (Fig. 4.1) to illustrate the influence of bottom friction on the spectral response behavior of the flat bed in the closed basin.

Flat bed without bottom friction

The frictionless expression can now easily be obtained by substituting γ = 1 in expression (A.13), which gives

$$N(L)_{\text{closed}} = \frac{T^{(x)}}{ghk}\left(\frac{1-\cos kL}{\sin kL}\right). \qquad (A.14)$$

This solution (A.14) has been used in Section 4.1 to obtain the classical resonance properties of the closed basin.

A.3 Solution for the semi-enclosed basin

The boundary and matching conditions that apply in the semi-enclosed basin are:

$$N_1 = 0 \quad at\ x = -L_1, \qquad \frac{\partial N_2}{\partial x} = \frac{T^{(x)}}{gh_2} \quad at\ x = L_2. \qquad (A.15)$$

$$\frac{\partial N_1}{\partial x} = \frac{h_2}{h_1}\frac{\partial N_2}{\partial x} \quad at\ x = 0, \qquad N_1 = N_2 \quad at\ x = 0. \qquad (A.16)$$

These conditions will now be used to solve the amplitude of the surface elevation at the right basin boundary $N_2(L_2)$. The expressions for N_1 and N_2 are given by Eqs. (A.2 & A.3) in Section A.1. The coefficients A_1, A_2, B_1 and B_2 will now be different than the coefficients for the closed basin case in the previous Section. Therefore these coefficients have to be derived again. Substituting the first boundary condition at $x = -L_1$ in the equation of N_1 gives

$$B_1 = \frac{A_1}{\tan(\gamma_1 k_1 L_1)}. \qquad (A.17)$$

Substituting the second boundary condition at $x = L_2$ gives

$$B_2 = A_2\tan(\gamma_2 k_2 L_2) + \frac{T^{(x)}}{gh_2\gamma_2 k_2\cos(\gamma_2 k_2 L_2)}. \qquad (A.18)$$

Substituting the first matching condition at x = 0 gives

$$B_1 = \frac{h_2\gamma_2 k_2}{h_1\gamma_1 k_1} B_2. \qquad (A.19)$$

From the second matching condition it follows that $A_1 = A_2$. Substituting Eqs. (A.17) and (A.18) in Eq. (A.19) will give

$$A_1 = \frac{T^{(x)}}{gh_1\gamma_1 k_1}\left(\frac{\tan(\gamma_1 k_1 L_1)/\cos(\gamma_2 k_2 L_2)}{1-\mu\tan(\gamma_1 k_1 L_1)\tan(\gamma_2 k_2 L_2)}\right), \quad \text{with } \mu = \frac{h_2\gamma_2 k_2}{h_1\gamma_1 k_1}. \qquad (A.20)$$

The derived solution for A_1 can now be substituted in Eq. (4.9). Notice that $A_1 = A_2$, which gives

$$B_2 = \frac{T^{(x)}\tan(\gamma_2 k_2 L_2)}{gh_1\gamma_1 k_1}\left(\frac{\tan(\gamma_1 k_1 L_1)/\cos(\gamma_2 k_2 L_2)}{1-\mu\tan(\gamma_1 k_1 L_1)\tan(\gamma_2 k_2 L_2)}\right) + \frac{T^{(x)}}{gh_2\gamma_2 k_2\cos(\gamma_2 k_2 L_2)}. \qquad (A.21)$$

To find the full solution of $N_2(L_2)$, the derived coefficients A_2 and B_2 will be substituted in Eq. (A.3). This results in

$$N_2(L_2)_{\text{semi}} = \frac{T^{(x)}}{gh_1\gamma_1 k_1}\left(\frac{\sin(\gamma_1 k_1 L_1)\cos(\gamma_2 k_2 L_2) + \frac{1}{\mu}\sin(\gamma_2 k_2 L_2)\cos(\gamma_1 k_1 L_1)}{\cos(\gamma_1 k_1 L_1)\cos(\gamma_2 k_2 L_2) - \mu\sin(\gamma_1 k_1 L_1)\sin(\gamma_2 k_2 L_2)}\right). \qquad (A.22)$$

In turn, the solutions for the flat bed case with and without bottom friction will be derived from this expression (A.22).

Flat bed with bottom friction

The solution for the flat bed case with bottom friction can be obtained by substituting $L_2 = 0$ in expression (A.22), leaving L_1 capturing the basin length L:

$$N(L)_{\text{semi}} = \frac{T^{(x)}}{gh\gamma k}\tan\gamma kL. \qquad (A.23)$$

This solution (A.23) has been used in Section 4.1 (Fig. 4.1) to illustrate the influence of bottom friction on the spectral response behavior of the flat bed in the semi-enclosed basin.

Flat bed without bottom friction

The frictionless expression can now easily be obtained by substituting $\gamma = 1$ in expression (A.23), which gives

$$N(L)_{\text{semi}} = \frac{T^{(x)}}{ghk}\tan kL. \qquad (A.24)$$

This solution (A.24) has been used in Section 4.1 to obtain the classical resonance properties of the semi-enclosed basin.

Appendix B

1-DH model simulations

In this appendix we will present some results of the pit and shoal cases which are referred to in Chapter 4. The influence of bottom friction on the spectral response of the shoal and pit cases, treated in Section 4.2.3, are presented in Figures B.1 (closed basin) and B.2 (semi-enclosed basin).

Here, the focus is not on the sensitivity of the h/L ratio of the element, but on the differences in spectral response behavior between weak (a) and moderate (b) bottom friction.

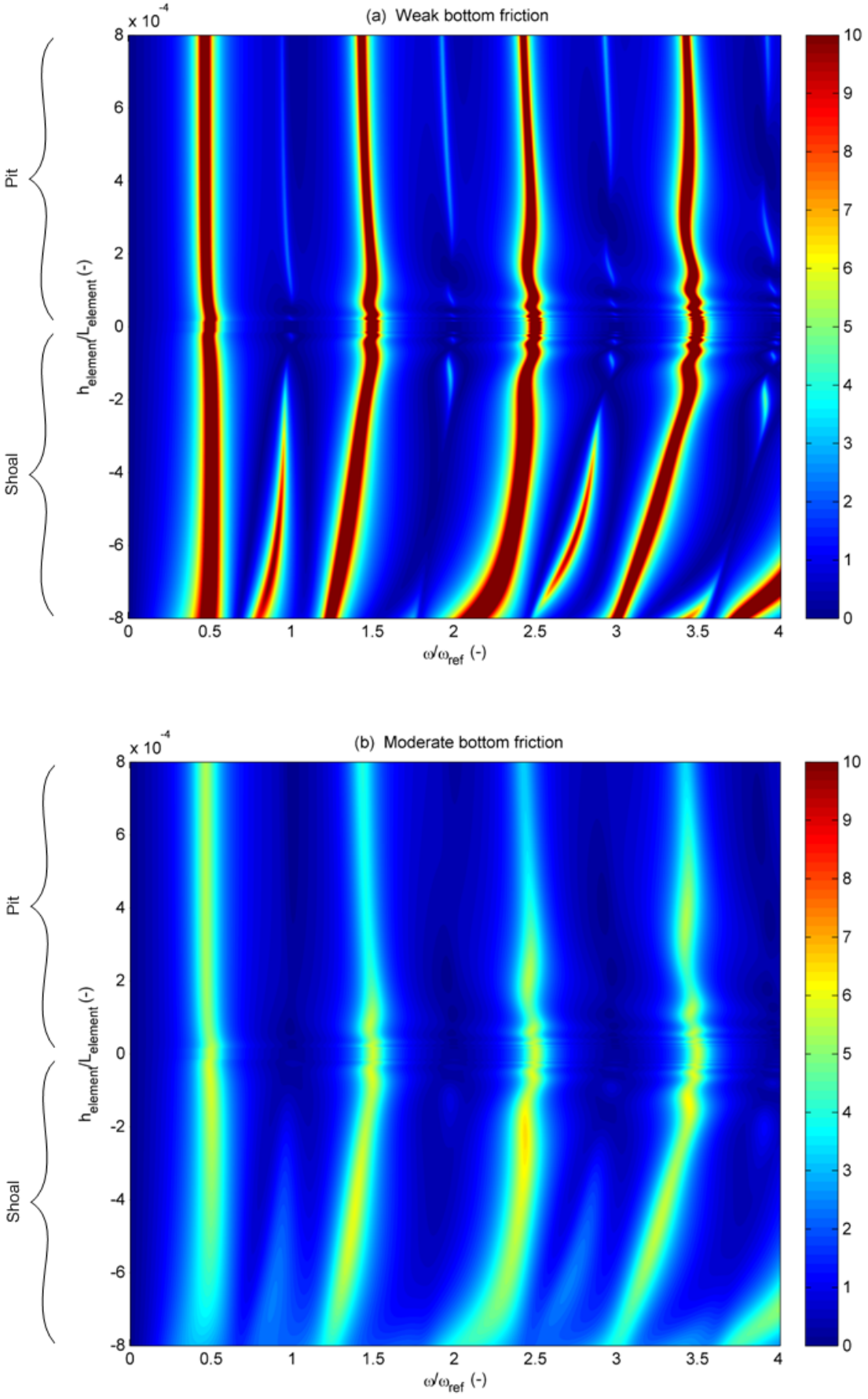

Figure B.1: Scaled amplification factor A as a function of dimensionless forcing frequency ω/ω_{ref} (horizontal axis) and ratio $h_{element}/L_{element}$ (vertical axis) at the rear end of the closed basin ($x = L$) for two bottom friction coefficients: (a) $r = 0.0002$ m s^{-1}, (b) $r = 0.001$ m s^{-1}. Positive (negative) ratios on the vertical axis represent pit (shoal) cases.

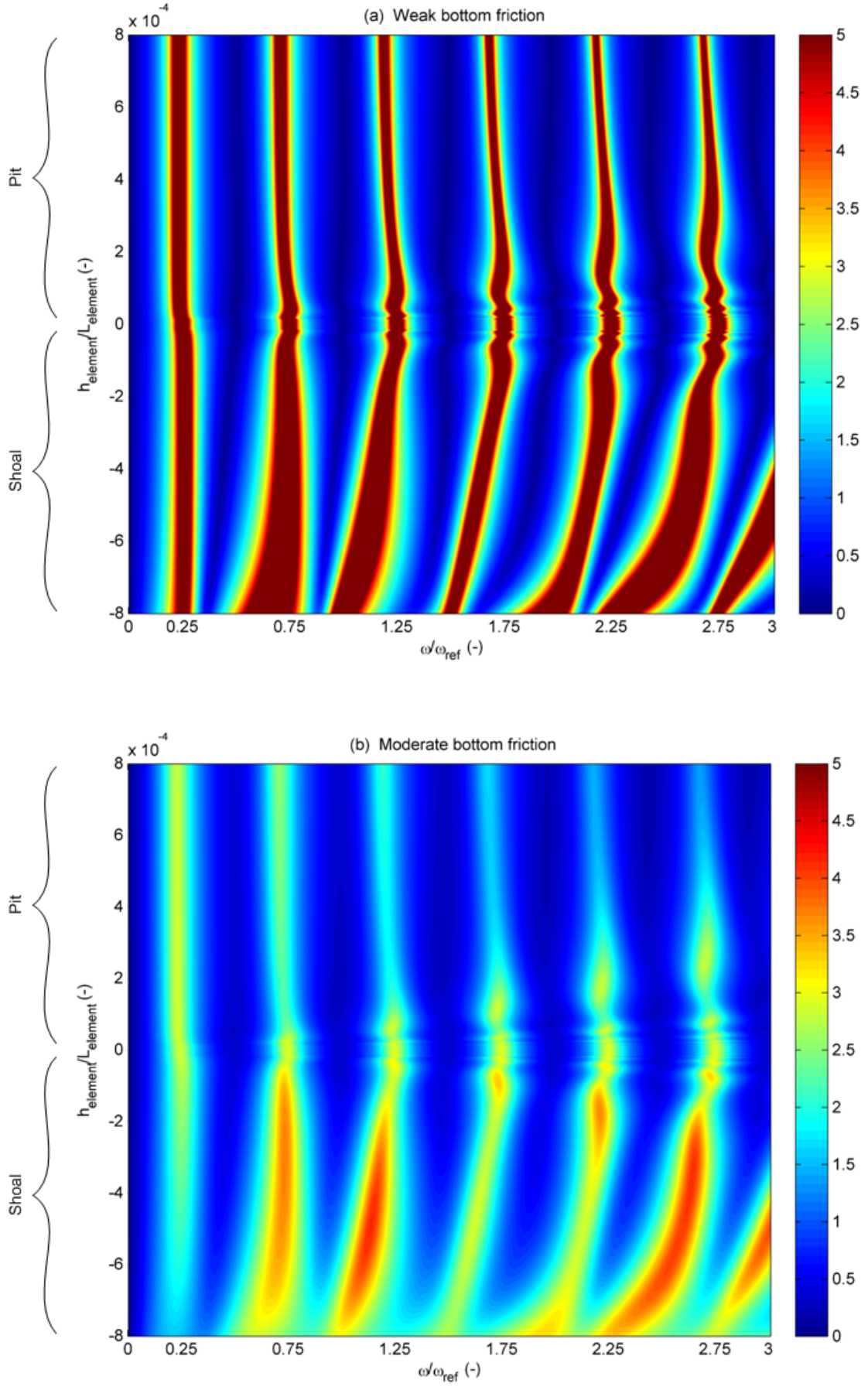

Figure B.2: Same as Fig. B.1, but now for the semi-enclosed basin.

Appendix C

Relation between roughness coefficients for the 1-DH & 3-D flow models

To give an indication of the validity of the applied roughness parameters in the FEM model, we would like to express the linearised bottom friction coefficient r ($m\ s^{-1}$) of the 1-DH flow model in the set (s, K_v) representing the linearised bottom friction s (m s^{-1}) and vertical eddy viscosity K_v ($m^2\ s^{-1}$) of the 3-D FEM model. We do this by considering a steady uniform flow in both models, meaning ω (rad s^{-1}) of the periodic wind forcing is zero. For simplicity, we will apply a modified coordinate system for this comparison, relative to the coordinate system we use in all other analyses of this study. This means that the bottom of the basin is set at z = 0 and the still water level of the surface water elevation $z = h$ (instead of at $z = -h$ and z = 0, respectively).

C.1 Derivation of $u(z)$ for the 3-D flow model

First we will derive the along-basin flow velocity $u(z)$ for the 3-D flow model in this simplified case. Since we consider a steady uniform flow, this implies

$$\frac{\partial}{\partial z}\left(\tau^{(x)}, \tau^{(y)}\right) = 0 \qquad \text{with} \qquad \frac{\left(\tau^{(x)}, \tau^{(y)}\right)}{\rho_w} = K_v \frac{\partial u}{\partial z}, \tag{C.1}$$

which means

$$\frac{\partial}{\partial z}\left(\rho_w K_v \frac{\partial u}{\partial z}\right) = 0. \tag{C.2}$$

For simplicity, the horizontal shear stress from bottom to surface $\tau(z)$ in the basin will now be expressed as

$$\tau(z) = \rho K_v \frac{\partial u}{\partial z} = \beta = \text{constant}. \tag{C.3}$$

At the surface ($z = h$):

$$\tau(h) = \tau_w \qquad \rightarrow \qquad \beta = \tau_w \qquad\qquad \text{at } z = h. \tag{C.4}$$

Also boundary condition (3.4) from Chapter 3 applies at the surface

$$\frac{\partial u}{\partial z} = \frac{\tau_w}{\rho K_v} \qquad\qquad \text{at } z = h. \tag{C.5}$$

In turn, taking the primitive of Eq. (C.5) gives

$$u(z) = \frac{\tau_w}{\rho K_v} \cdot z + \gamma, \qquad (C.6)$$

with constant γ. To find γ, we state at the bottom (z = 0):

$$u(0) = u_b \quad \rightarrow \quad \gamma = u_b \qquad \text{at } z = 0. \qquad (C.7)$$

Also, the partial-slip condition (3.5) for Chapter 3 applies at the bottom. Because the shear stress does not vary over depth in this situation, we can express the flow velocity at the bottom u_b as a function of the bed shear stress τ_b ánd the wind shear stress τ_w. This means that we can combine Eqs. (3.5) & (C.3), which results in

$$K_v \frac{\partial u}{\partial z} = s \cdot u_b \quad \& \quad \tau(0) = \tau_b \qquad \text{at } z = 0, \qquad (C.8)$$

$$\frac{\tau_b}{\rho} = s \cdot u_b \qquad \text{at } z = 0. \qquad (C.9)$$

Furthermore, since $\tau_b = \tau_w$, from Eq. (C.9) we then find

$$\rho \cdot s \cdot u_b = \tau_w \quad \rightarrow \quad u_b = \frac{\tau_w}{\rho \cdot s} \qquad (C.10)$$

Finally, the along-basin flow velocity $u(z)$ can now be obtained by substitution of Eqs. (C.7) & (C.10) in Eq. (C.6):

$$u(z) = \frac{\tau_w}{\rho}\left(\frac{z}{K_v} + \frac{1}{s}\right). \qquad (C.11)$$

C.2 Expression for bottom friction coefficient *r* in roughness coefficients *s* and K_v

Next, we have to depth-average Eq. (C.11) to connect the 3-D flow model with the 1-DH model approach, which expresses the along-basin flow velocity as a depth-averaged flow. Recall from Chapter 3 (Eq. (3.15)) that depth-averaging means

$$\bar{u}(x) = \frac{1}{h}\int_0^h u(x,z)dz. \qquad (3.15)$$

Notice that in contrast to the time-dependent periodic flow velocity (dynamic condition) of both flow models, we have a steady flow here (expressed as t and ω = 0). To continue with the derivation, depth-averaging Eq. (C.11) results in

$$\bar{u}(x) = \frac{\tau_w}{\rho}\left(\frac{z}{K_v} + \frac{1}{s}\right). \qquad (C.12)$$

Since $\tau_b = \tau_w$, Eq. (C.12) becomes

$$\tau_b = \frac{\rho \cdot \bar{u}}{\frac{1}{2K_\mathrm{v}} h + \frac{1}{s}} \qquad (C.13)$$

From the 1-DH model approach, we also use

$$\frac{\tau_b}{\rho} = r \cdot \bar{u} \qquad \text{at } z = 0. \qquad (C.14)$$

Eventually, we can express *r* in *s* and K_v by combining Eqs. (C.13 & C.14), such that we find

$$r = \frac{1}{\frac{1}{2K_\mathrm{v}} h + \frac{1}{s}} \,. \qquad (C.15)$$

Although this relation is derived for steady uniform flow, it will be used for unsteady flow in Section 5.2.3 to provide some guidance for the applied roughness coefficients (*s*, K_v) in the FEM model.